ELECTRON ENERGY SPECTROMETERS FOR THE SCANNING ELECTRON MICROSCOPE

HUNG QUANG HOANG

(M.Sc, Vietnam National University of Hanoi)

A Thesis Submitted for the Degree of Doctor of Philosophy

Department of Electrical and Computer Engineering

National University of Singapore

2011

Acknowledgments

With the completion of this thesis, I would like to acknowledge those who have helped make this project possible.

Foremost, to my Supervisor, Associate Professor Anjam Khursheed, I would like to express my sincere thanks for his advice, encouragement, and support during this project and taking time to carefully read through the thesis manuscript.

I would like to thank the staffs in the CICFAR lab, particularly Mrs Ho Chiow Mooi and Mr Koo Chee Keong for all kinds of administration and hardware support.

A special thank goes to Dr. Mans Osterberg and Dr. Tao Luo for their fruitful discussions and help during the project. I truly appreciate Mr. Nelliyan Karuppiah, an expert on SEM operation who helped me much on SEM operation in my early days in CICFAR.

Finally, I would like to express my gratitude to my parents who have been behind me at every stage, providing unwavering support.

Table of Contents

Summary

This thesis aims to develop electron energy spectrometers for the Scanning Electron Microscope (SEM), in order to make it a more powerful instrument for nano-scale material and device inspection. Three electron energy spectrometers are reported in this thesis for SEMs of different types of objective lenses.

The first spectrometer is based upon the use of a circular magnetic beam separator, suitable for SEMs that have electric/magnetic field immersion objective lenses. These kinds of SEMs are able to obtain high image resolution at low primary beam voltage (1kV or less). The circular magnetic beam separator acts as the first stage of the spectrometer, separating different energy ranges of scattered electrons. An array of post-deflectors, which utilize retarding mixed electric/magnetic fields, are subsequently used to disperse and focus all the scattered electrons onto their own detectors. This redesigned SEM/spectrometer combination is able to capture the whole range of scattered electrons, from secondary electrons, Auger electrons to backscattered electrons in parallel. Both simulation design as well as an experimental prototype for testing the spectrometer concept inside a conventional SEM is reported.

The second spectrometer design in this work is a toroidal geometry spectrometer that can be incorporated into the specimen chamber of a conventional SEM as an add-on attachment. This spectrometer design goes beyond previous toroidal spectrometer designs by achieving second-order focusing, effectively improving the energy resolution of previous toroidal spectrometers by over a factor of seven for the same transmission. A prototype of this spectrometer design is manufactured as an add-on

attachment inside a conventional SEM, and experimental results are reported that confirm simulation predictions.

The third spectrometer is a new high resolution-transmission energy spectrometer design, named the Radial Mirror Analyzer (RMA). This spectrometer design is based upon modifying the well-known fountain spectrometer, enabling it to function as an add-on attachment that can be permanently incorporated inside the SEM chamber, like a normal energy dispersive X-ray analysis (EDS) unit. The predicted energy resolution for this spectrometer is around one order of magnitude better than previous rotationally symmetric electrostatic energy spectrometers such as the cylindrical mirror analyzer for the same transmission.

The spectrometer designs in this work have applications beyond electron microscopy, to other areas in applied physics such as surface sciences.

List of Tables

List of Figures

List of Symbols

SYMBOL	DESCRIPTION
ϕ, ϕ_1, ϕ_2	Deflection angle
β, β_1, β_2	Azimuthal entrance angle
$\theta, \theta_1, \theta_2$	Polar entrance angle
$\Delta\theta$	Semi-angle of an electron beam
θ_c	Cut-off angle
W	Working distance
T	Transmittance (transmission) of a spectrometer
E_P	Pass energy
E_0	Centre band energy
TR	Trace-width of an electron beam
$\Delta E/E$	Relative energy resolution
R, R_1, R_2	Radius of a spectrometer
V_S	Specimen voltage
V_M	Mirror voltage
V, V_1, V_2, V_3, V_D	Potentials applied to electrodes
W	Working distance
SE	Secondary electron
BSE	Backscattered electron
AE	Auger electron
η	Backscattered yield coefficient
δ	Secondary electron yield
Y_A	Auger electron yield
n_p	Number of primary electrons
SNR	Signal-to-noise ratio

Chapter 1: Introduction

The aim of this thesis is to design and develop electron energy spectrometers for the scanning electron microscope (SEM). At present, the detection systems of conventional SEMs are not generally designed to capture the energy spectrum of electrons scattered from the sample. The main analysis tool used inside the SEM for defect/material analysis is the well-known Energy Dispersive X-ray (EDS) method. However, this technique is limited by a spatial and depth resolution of about 1μm and is difficult to use for low energy electron beam applications (<10kV) [1.1]. By integrating energy spectrometers into the SEM design, the energy spectrum of its scattered electrons can be obtained, enhancing the kind of information that SEMs can acquire on the nano-scale, making them more powerful material and device instruments.

Although some electron energy spectrometers have been developed for the SEM in the past, most of them have been made for the purpose of quantifying voltage contrast. Towards the late 1980s, several companies emerged which manufactured dedicated scanning electron microscope columns, known as Electron Beam Testers (EBTs) which were specifically designed and optimized to make quantitative voltage measurements on integrated circuits. From the late 1980s, integrated circuit manufacturers started to make circuits covered by a top ground plane, making it difficult for Electron Beam Testers to directly probe conductors, and they therefore diminished in popularity.

New possibilities of using energy spectrometers for other applications inside the SEM

other than voltage contrast are recently emerging. Backscattered electron (BSE) detection is well known for qualitative material contrast imaging in the SEM. However, change in atomic number of the specimen being probed also provides a significant change in the shape of the BSE energy spectrum, making it possible to perform material quantification by monitoring the BSE spectrum shape. An example of this possibility has been proposed by Luo and Khursheed [1.2], where they correlated experimental BSE spectra with corresponding Monte-Carlo simulations. This technique might be useful in some cases for single element material analysis. Backscattered spectrometers have also been used by Rau et al. to provide depth information about multi-layer specimens [1.3]. Some recent work by Kazemian et al. [1.4-1.5] demonstrate that by monitoring changes in the secondary electron (SE) spectrum, dopant concentrations in semiconductor samples can be quantitatively mapped inside the SEM. Furthermore, the possibility of carrying out Auger electron (AE) elemental analysis in the SEM has been demonstrated in the work by El-Gomati [1.6-1.7] and Cubric [1.8], where the Auger spectrum from a specimen can be acquired by a fast energy analyzer after cleaning its surface by ion bombardment. This makes Auger spectroscopy a promising tool for analyzing nano-scale defects and elemental identification inside the SEM. This method might well be a useful companion method to the widely used EDS spectrometry technique and overcome important restrictions of standard EDS, of being limited to operate with primary beam energies between 10 to 20 keV and having low (micron) spatial resolution [1.1]. All in all, these new possibilities of using scattered electron spectra inside the SEM require higher performance energy spectrometers than previous voltage contrast spectrometers and form the motivation for this thesis to develop new electron energy spectrometers for the SEM.

1.1   Objective lens improvements

One of the most important considerations for integrating a spectrometer in the SEM is how it fits together with the objective lens. Over the last few decades, different SEM columns have been designed, utilizing different types of objective lenses, as shown in Fig. 1.1 [1.9]. Each of these lenses has a different way of detecting scattered electrons from the specimen. Hence, different energy spectrometer designs are required for different kinds of objective lenses, based up on their mechanical arrangement as well as their way of detecting scattered electrons.

In the conventional SEM, illustrated in Fig. 1.1a, the specimen is placed in the free-field region below the final pole-piece of the objective lens with a working distance, which is defined by the distance between the final pole piece of the SEM objective lens and the specimen, normally ranging from 5 mm to 30 mm, scattered electrons are emitted in all directions. The electron energy analyzer in this case needs to be directly placed in between the final pole-piece of the objective lens and the specimen like a normal SE or BSE detector as illustrated in Fig. 1.2. These electron spectrometers are typically designed as add-on attachments to fit inside the SEM chamber. Examples of these types of spectrometers are found in the work by Feuerbaum [1.10] for secondary electrons, Jacka et al. for Auger electrons [1.11], and Rau et al. for backscattered electrons [1.12-1.13].

The main drawback of this type of spectrometer is that placing it below the SEM objective lens results in a large working distance (W). A larger working distance increases on-axis aberrations of the primary beam spot on the specimen, which in turn significantly degrades the image resolution. The challenge in designing electron

energy spectrometers for conventional SEMs, is to make them so that they allow for a small working distance, and this is an important motivation for the work in this thesis. The spectrometers reported in Chapters 3 and 4 are designed with this goal in mind.
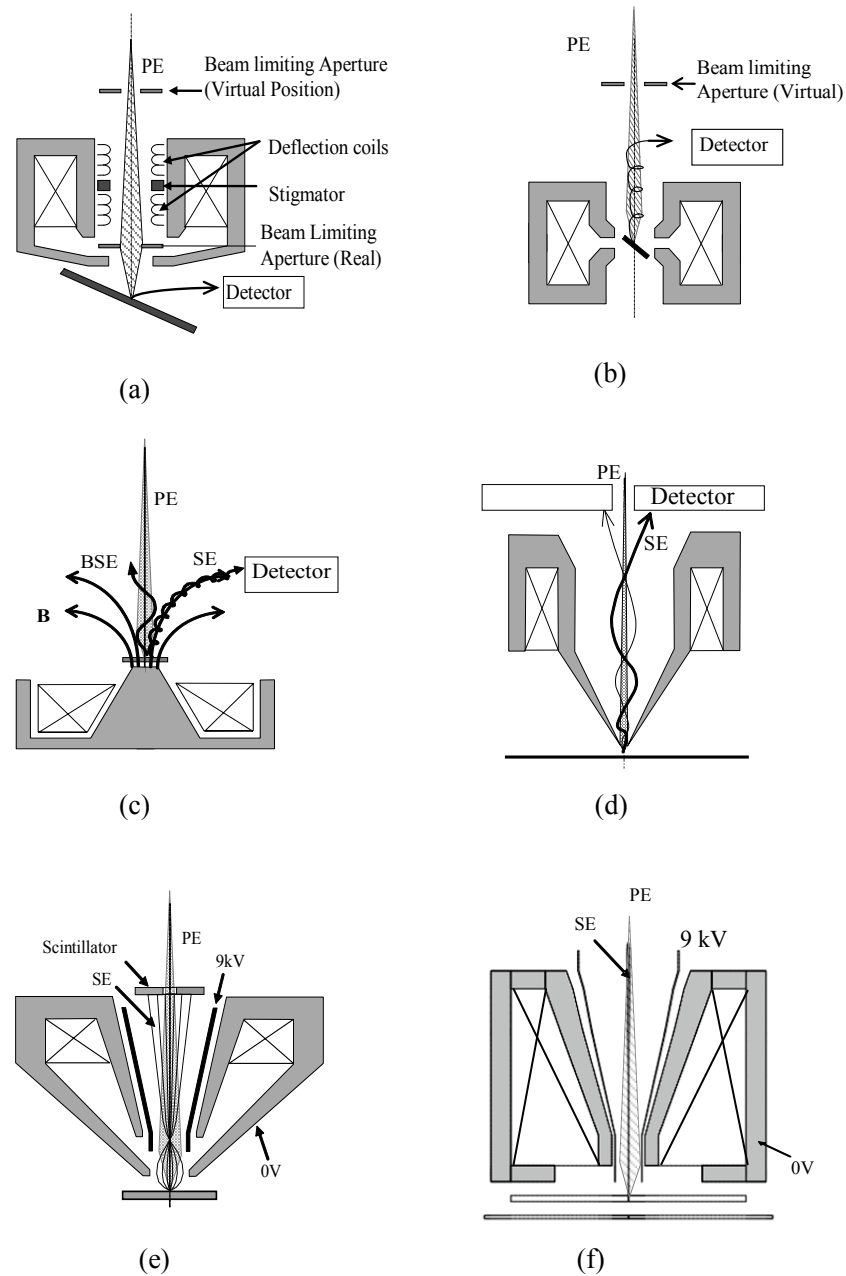
Fig. 1. 1. Different types of SEM objective lenses: (a) Conventional lens; (b) Magnetic In-lens; (c) Single pole lens below the specimen; (d) Single pole lens above the specimen; (e) Retarding field lens; and (f) Mixed-field immersion lens
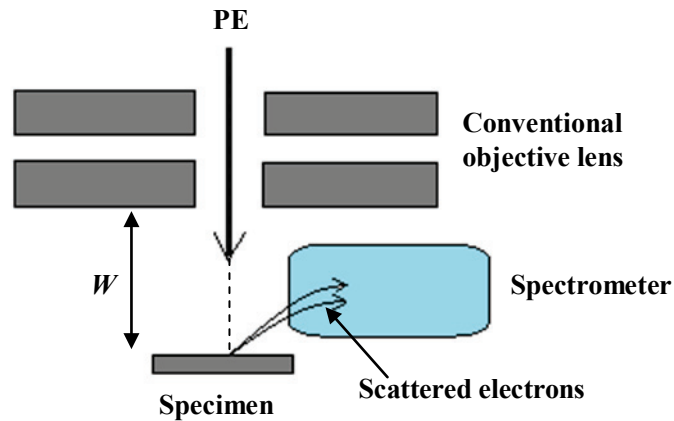
Fig. 1. 2. Arrangement of an energy spectrometer for conventional objective lens type SEMs

Beyond the conventional objective lens column, various SEM columns incorporate different objective lens design improvements. These lens improvements are designed to enhance the SEM spatial resolution, particularly at low lending energy, some of them are illustrated in Figures 1.1b-f. They include a magnetic in-lens type of objective lens, where the specimen is placed in the lens gap region (Fig. 1.1b); semi-in lenses, where the magnetic field extends beyond a single lens pole-piece (Figs. 1.1c-d); a retarding field lens, where the primary beam is slowed down just before it strikes the specimen (Fig. 1.1e); and a mixed field immersion lens, where the specimen is immersed in both a retarding electric field and a strong magnetic field (Fig. 1.1f). A more detailed review of these types of objective lens improvements can be found in the work reported by Khursheed [1.9][1.14].

The combination of an electric retarding field overlaid by a magnetic immersion field lens requires a way of separating scattered electrons from the primary beam, since their trajectories are strongly collimated and travel up close to the electron optical axis. A Wien filter can be used to deflect secondary electrons off-axis to improve the

collection efficiency, as shown in Fig. 1.3. Examples of using Wien filters in this way are reported by Kienle and Plies [1.15], or in the KLA commercial electron beam inspection system [1.16].
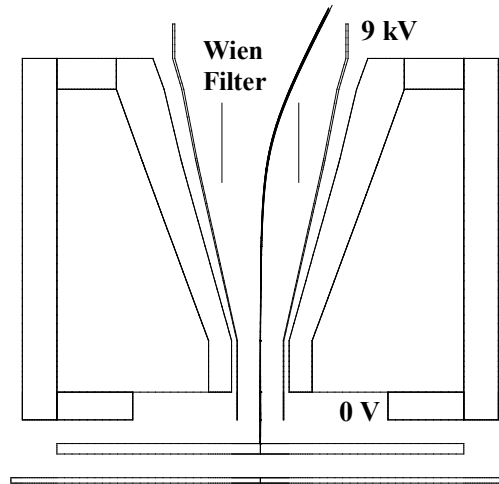
Fig. 1. 3. Separation of scattered electrons from the primary beam by use of a Wien filter in a mixed field immersion lens [1.9].
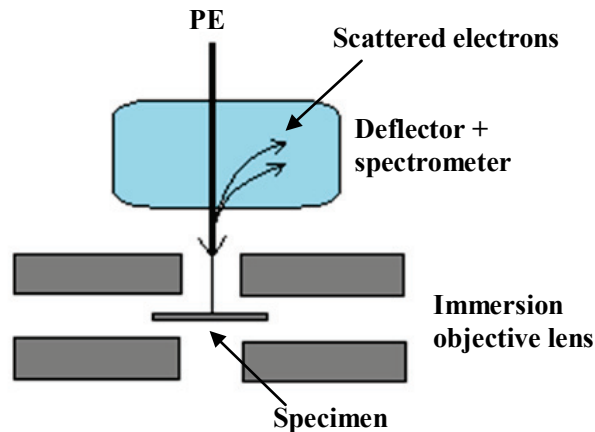
Fig. 1. 4. Energy spectrometer arrangement for immersion objective lens type SEMs.

Electron energy spectrometers have also been placed above the lens, where scattered electrons travel up through the objective lens bore and are then separated from the primary beam before reaching the spectrometer. This type of spectrometer is classified as a through-the-lens spectrometer design. The spectrometer then analyzes scattered electrons, and directs them to the detector system as illustrated in Fig. 1.4. Designs of

6

these kinds of spectrometers have been proposed by Frosien and Plies for secondary electrons [1.17], Kruit and Venebles [1.18] for secondary and Auger electrons, and by Kienle and Plies for parallel acquisition of secondary electrons [1.15]. Most of these designs use a Wien filter to separate scattered electrons from the primary beam. However, one of the problems of using a Wien filter for electron energy spectrometers is that its energy dispersion is relatively low, resulting in poor performance of its spectrometer action.

How to separate scattered electrons from the primary beam in these kinds of lenses, where scattered electrons travel through the lens bore, is the motivation for the spectrometer design reported in Chapter 2.

1.2 Electron spectrometers for the scanning Auger electron microscope (SAM)

It is important to describe some important parameters for spectrometer design to determine the performance of a spectrometer that can be used for spectroscopic applications. There are two main design parameters, the energy resolution and the transmittance (transmission). In general, the energy resolution of an electron energy analyzer provides a reasonable estimate of how well two signals of different energies can be separated by the analyzer as illustrated in Fig. 1.5, while its transmittance represents how efficiently the analyzer collects the electrons emitted from the specimen under analysis. The energy resolution is usually defined as the ratio $\Delta E/E_p$, where ΔE is the full width at half maximum (FWHM) of the energy distribution of a monochromatic beam through the analyzer, and E_p is the pass energy of the analyzer. In most cases, a relative energy resolution (in percentage) is used. In the context of

spectrometer design, the energy resolution can be estimated by comparing the FWHM of the electron beam trace-width created by spherical aberration, compared to the dispersion along the detection plane (Gaussian plane) caused by energy spread.
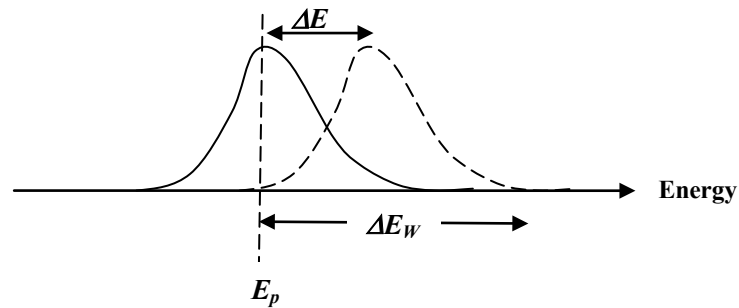
Fig. 1. 5. Definition of analyzer resolution
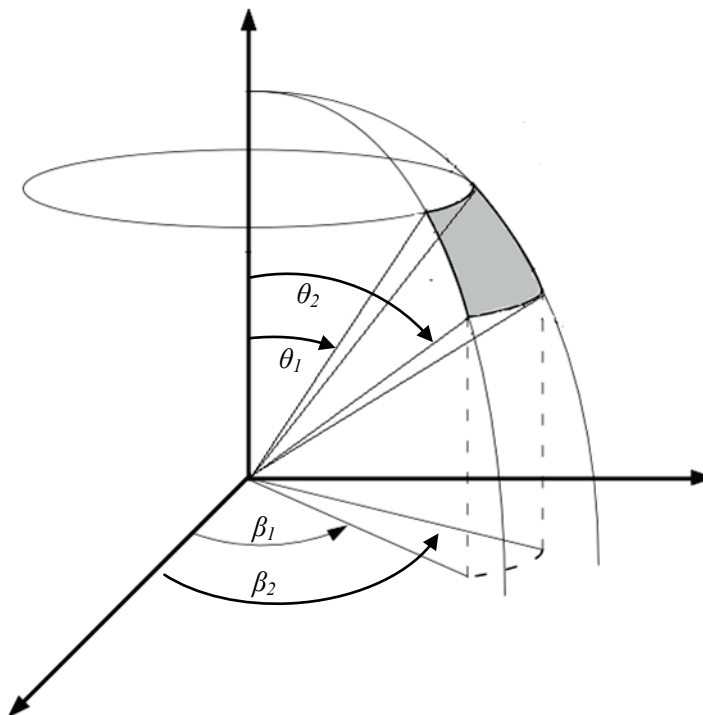
Fig. 1. 6. Azimuthal and polar angles of electrons emitted from specimen

Transmittance (or transmission) of an electron energy analyzer in this thesis, is defined to be the fraction of electrons at a given energy that arrive at the analyzer detector, compared to those that leave the specimen. Inside the SEM, the distribution of scattered electrons is best approximated by a cosine polar angular distribution [1.9].

In this case the transmittance of the analyzer, T, can be calculated by

$$T = \frac{(\beta_2 - \beta_1)}{4\pi}[\cos 2\theta_1 - \cos 2\theta_2] \times 100$$

(1.1)

where the analyzer azimuthal and polar entrance angles range from β_1 to β_2 and θ_1 to θ_2 respectively, as shown in Fig. 1.6. Even in cases where analyzers are designed to capture the full 2π steradian solid angle of emission, electrons are usually scattered and absorbed within the analyzer. The transmittance of most analyzers lies well below 30%.

High performance electron energy spectrometer designs are usually discussed in the context of Auger electron spectrometry (AES) for the Surface Sciences, and the instrument used for this purpose is the scanning Auger electron microscope (SAM). The SAM instrument actually shares much in common with the SEM as illustrated in Fig. 1.7. They both direct a focused primary electron beam on to a specimen, and capture electrons that are subsequently scattered back from it. Their electron beam columns have all the same kind of features, a tungsten/field emission electron gun, condenser lenses, an objective lens, scanning/stigmator coils, a final aperture, and electron detectors.
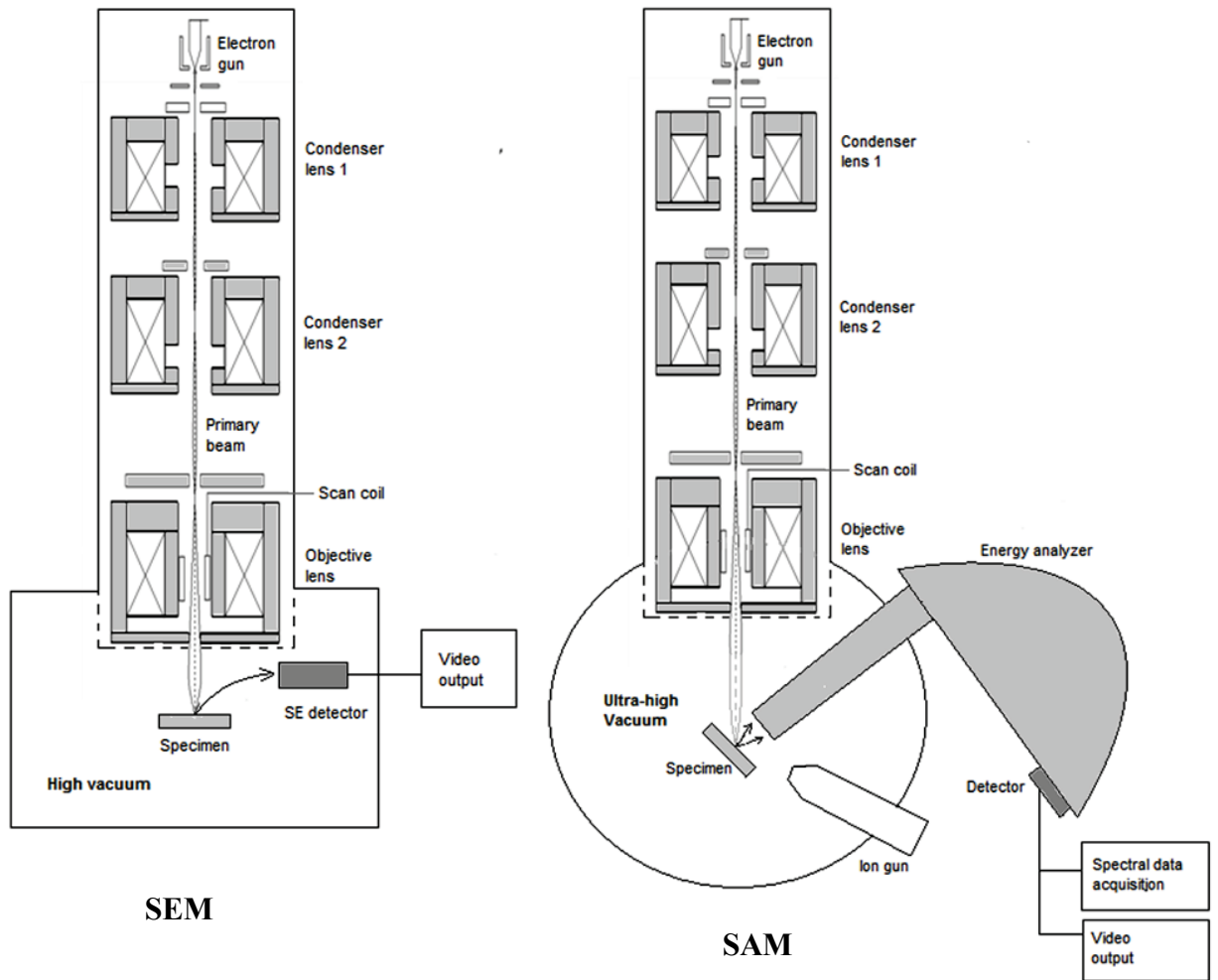
Fig. 1. 7. The schematic layouts of the SEM and the SAM instruments

In terms of scattered emission from the specimen under test, the energy spectrum of emitted electrons in both the SEM and the SAM consists of the same contributions, from secondary electrons, Auger electrons and backscattered electrons as shown in Fig. 1.8. One might therefore ask, what are the differences between the SEM and the SAM that have caused them to develop so differently, the SEM for high resolution imaging purposes and the SAM for high resolution spectrometry in the Surface Sciences? Can the SEM be used like the SAM for the purpose of electron spectrometry to form an instrument that has both high resolution imaging and high resolution electron spectrometry for nano-scale analysis?

SE   BSE

N(E)

Plasmon
losses

AE peaks

0   50 eV   Primary beam
              Energy E   energy
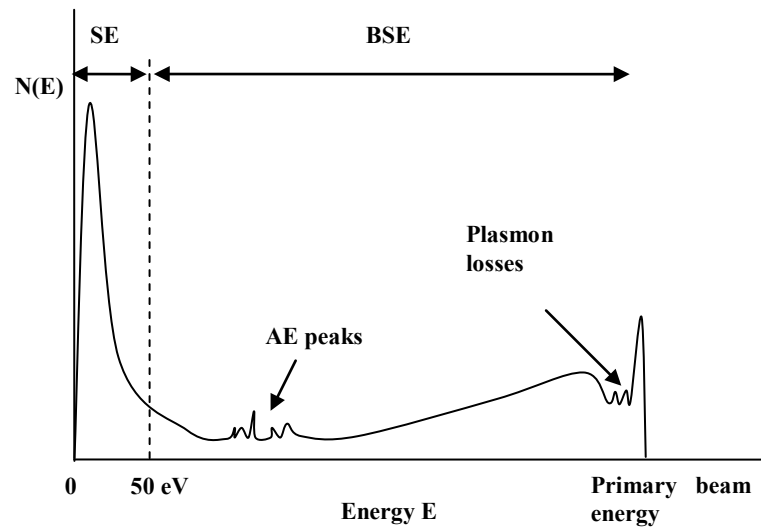
Fig. 1. 8. Energy spectrum of scattered electrons that leave the specimen inside SEMs and SAMs

There are two main differences between the SEM and the SAM that form the answer to the above questions. The first difference is in the way they detect scattered electrons from the specimen. The SEM detects its scattered electrons (usually SE signal) as an integrated current to form high resolution imaging contrast, while the SAM has something that most SEMs do not usually have, an electron energy analyzer to acquire the energy spectrum of scattered electrons, as illustrated in Fig. 1.8. The presence of an electron energy analyzer in the specimen chamber, however, usually causes the working distance (distance of final lens to specimen) in the SAM to be larger than it is for the SEM. The second difference relates to the vacuum environment inside the specimen chamber. The ultra-high vacuum (UHV) environment of the SAM specimen chamber (10^{-9}- 10^{-10} torr) is much higher than the vacuum level inside the SEM specimen chamber, which has a normal high vacuum (HV) environment (10^{-5}- 10^{-7} torr). Detection of Auger electrons requires the specimen surface to be very clean to avoid many mono-layers of contamination that

prevent Auger electrons leaving the specimen surface. This condition requires the specimen to be placed in an UHV environment and an ion flood gun normally needs to be used to clean the specimen surface in-situ. Detection of Auger electrons in the SEM specimen chamber is, therefore normally not possible. The UHV chamber has a host of different devices/detectors, other than the electron beam column and SE detector, and the SAM for these reasons, is a much more expensive and complex instrument than the SEM.

As mentioned, El-Gomati [1.7] and Cubric [1.8] recently showed that it is possible to acquire the Auger electron spectrum in the HV environment of the SEM for a short period of time after cleaning the specimen surface by ion bombardment. Thus, if a high performance electron energy analyzer and an ion flood gun can be incorporated into a SEM without greatly increasing the working distance, there is the potential for the SEM to be used as a low cost instrument for both imaging and spectroscopic analysis on the nano-scale.

The similarity of the SEM and the SAM naturally raises the question of whether the electron energy analyzers used for the SAM can be incorporated into the SEM? The two most commonly used electron energy analyzers for the SAM are the Cylindrical Mirror Analyzer (CMA) and the Hemispherical Deflector Analyzer (HDA). The CMA was first described by Sar-El [1.19] and then shortly afterwards employed for observing Auger electron spectrum by Palmberg [1.20], and subsequently developed by many research groups for charged particle spectrometry applications [1.21-1.22]. The best resolution of the CMA for an angular spread of ±6°, theoretically without the effect of the output aperture is around 0.155% [1.23]. Due to its second-order optics,

this is typically around a factor of 6 times better than most other types of spectrometers, which are usually characterized by first-order optics [1.24]. Here, the first-order optics (focusing) occurs where small variations with respect to the first-order change in input polar angle are zero, that is, to the first-order, trajectories that leave with slightly different initial angles focus at the same exit point. In this case, the trace-width at the Gaussian focusing plane depends on the angular spread by a second-order function. The second-order optics (focusing) occurs when the focal point position does not change with respect to second-order variations in the input angle. For this situation, the trace-width dependence with angular spread becomes a third-order one, resulting in significantly better energy resolution in comparison with the first-order focusing. In practice, most of the CMA designs have an energy resolution ranging from 0.25% to 0.7% for an angular spread of ±6° [1.25]. An important factor degrading its resolution in practice is a depth of focus error, which is caused by specimen misplacement. From a transmittance point of view, the CMA is very efficient because it has rotational symmetry and all electrons that pass through it are deflected by the same in-plane field distribution, there are no out-of-plane trajectory paths (neglecting the finite size of the source). The transmittance of the second-order focusing CMA is estimated to be 16.84% (an angular spread of ±6º), assuming that its entrance/exit grids have 90% transparency.
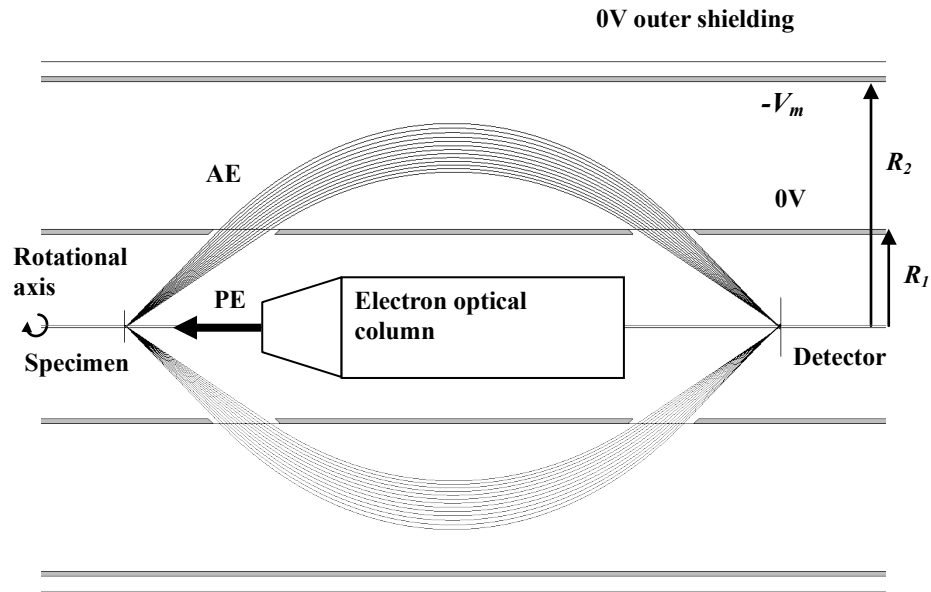
Fig. 1. 9. The CMA layout. The electric field distribution is created between concentric cylinders which are biased at different voltages, the inner one is usually grounded, located at radius R_1 from the rotational axis of symmetry, and the outer one, located at radius R_2 is biased to a mirror voltage ($-V_m$).

Fig. 1.9 shows a schematic diagram of the CMA layout. The specimen and focal point lie on a rotational axis of symmetry. An electron optical column usually needs to be placed inside the analyzer, in a field-free central region, making it difficult to combine the CMA with other existing electron beam instruments, such as the SEM.

The Hemispherical Deflection Analyzer (HDA) is presently the most widely used electron energy analyzer in the Surface Sciences at present. It is constructed by two inner and outer hemispheres with radii R_1 and R_2, in which the inner is grounded and the outer is biased at a potential V_m to deflect incoming electrons as shown in Fig. 1.10. The HDA is characterized by first-order focusing properties, so that it reports a poor energy resolution by itself (around 2% for an angular spread of ±6° in both in-plane and out-of-plane directions) [1.24]. In practice, the HDA, however, is combined with a series of lenses in a pre-analyzer decelerating column that allows it to operate

in a retardation mode, as shown in Fig. 1.10, effectively lowering the pass energy through the analyzer. A relative energy resolution below 0.05% is typically achieved in its retardation mode. The transmittance is comparatively low, due to its small angular azimuthal angle collection range, 0.172% for ±3° entrance angular spread, about 50 times lower than that for the CMA. A single detector can also be placed at the analyzer exit plane, instead of an aperture slit, and the HDA can be operated in a multi-channel mode with a band-pass width of around ±3% of the pass energy. The characteristics of the HDA can be found in detail from the work reported by Zouros et al. [1.26-1.27].
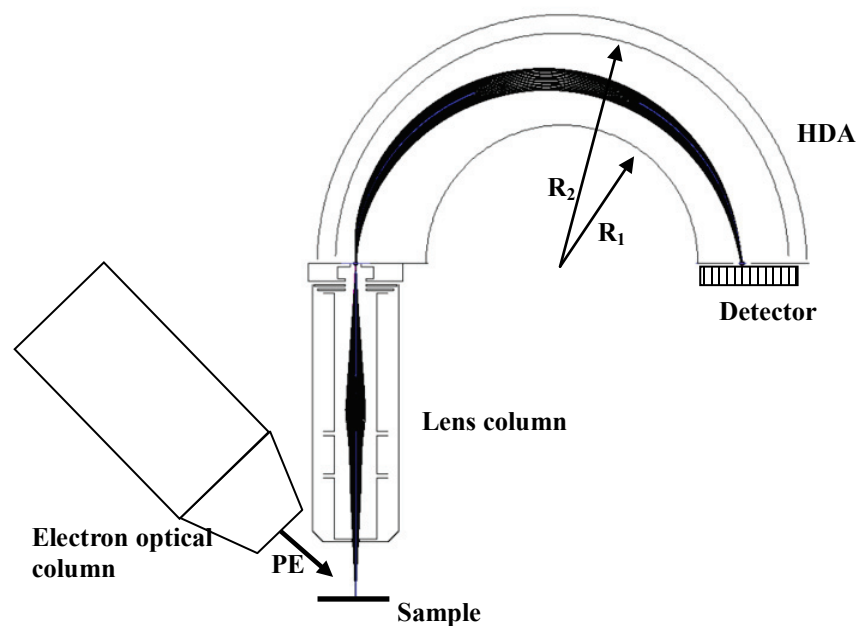
Fig. 1. 10. Schematic diagram of a HDA combined with its pre-retardation lens column.

Due to the complexity of its structure as well as its comparatively large size, the HDA system is usually placed outside the specimen chamber of the SAM. The pre-retardation lens is integrated into the specimen chamber through a port to collect scattered electrons from the specimen. This arrangement is not suitable for combining it with existing SEMs, since SEM chambers are relatively small and the space in

between the objective lens and the specimen is limited by a short working distance (of less than a few centimeters).

For reasons just mentioned, it is difficult to combine the CMA and the HDA in existing SEM instruments. There is a need to develop new electron energy spectrometers that have a comparable performance to the CMA and the HDA, and which can be integrated into the chambers of existing SEM instruments.

1.3   Parallel energy acquisition concept

A common feature of most dispersion analyzers such as the CMA is that their focusing properties depend on electron energy, and therefore they operate in a serial mode of data acquisition. A finite time is required for acquiring the signal and, for a typical electron energy spectrum of over a 2000eV range, the total acquisition time can be of the order of minutes. Therefore, another desirable feature for electron energy analyzers is to have parallel energy acquisition, where the output signal at a wide range of different energies can be obtained simultaneously, greatly speeding up data-acquisition times, in the order of seconds.

The HDA can operate in a partial parallel mode of operation by replacing the exit slit with a position sensitive detector, typically providing parallel acquisition over a small energy band of ±3% of the pass energy [1.27]. Other devices also exist to gather a larger energy band, such as the double-pass parallel plate analyzer that can gather an energy span of about 50% of the middle pass energy [1.28].

There have been a few proposals to design parallel electron energy acquisition

analyzers that can acquire a wide range of energy, about 2000eV and above. The hyperbolic field analyzer (HFA) is a parallel energy acquisition analyzer for Auger electron microscopy, which was proposed by Jacka et al [1.11][1.29], shown in Fig. 1.11. It can collect in parallel an energy spectrum with a range defined by E_{max}/E_{min} ≈36. It is typically set to capture a spectrum from about 75 eV to greater than 2500 eV by varying the analyzing field strength. Compared to most electron energy analyzers, the total transmission efficiency of the HFA is small. It can only collect 0.05% of 2π sr emission in order to provide an energy resolution of a few eV. However, the data acquisition time over the entire energy range between 75 eV to 2500 eV is very fast, normally less than 50 ms. This parallel energy analyzer has been developed and commercialized by Shimadzu corporation for fast analysis on the nano-scale [1.8]. As depicted in Fig. 1.11, the HFA analyzer can be incorporated into the chamber of conventional SEMs due to its compact size.
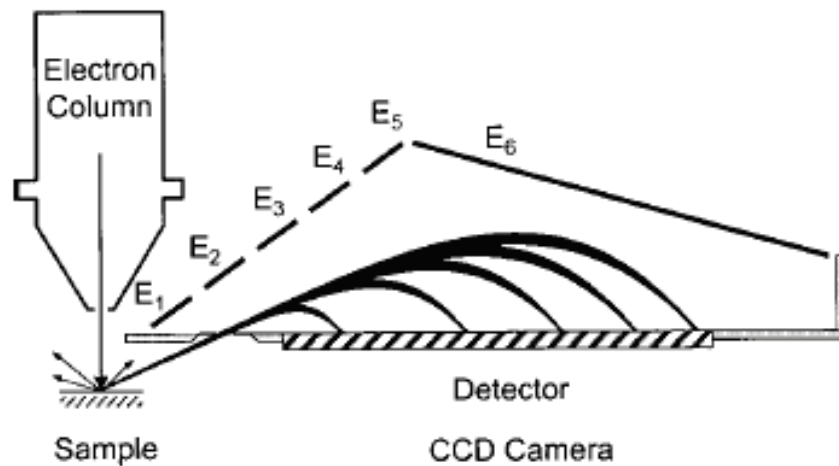
Fig. 1. 11. A schematic diagram of a HFA.

Another parallel electron energy acquisition analyzer proposal for Auger electron spectroscopy is a modified version of the CMA, called the "parallel cylindrical mirror analyzer" (PCMA), reported by F. H. Read et al [1.30-1.31]. The new PCMA design

is similar to the conventional CMA. The only difference in the new design is that a linear potential variation (instead of a fixed voltage as in the conventional CMA) is applied to the outer cylinder, and the space between its two concentric cylinders is closed by placing disks at the two ends with a non-uniform potential drop along the radial direction. This variation allows the analyzer to accept all the electrons within a wide energy range and to disperse them along its symmetric axis. For axis-to-axis focusing, the energy range is from 300 eV to 1500 eV. The achievable energy resolution is predicted to be between 0.182% to 0.456%, with a transmission of 1%. However, like the CMA, it is difficult to integrate the PCMA into existing SEMs since its rotational axis lies 90º to the primary beam axis.

A new parallel energy acquisition electron spectrometer design is presented in Chapter 2, and its predicted performance will be compared with the HFA and the PCMA.

1.4   Signal-to-noise ratio (SNR) considerations

Shot noise, generated within the SEM primary beam and its interaction with the specimen usually sets the limit to which output signal variations can be resolved, and determines the data acquisition time required for a reasonable signal-to-noise ratio (SNR). The number of primary beam n_p electrons within time τ is assumed to follow a Poisson distribution [1.32], having a mean value $\bar{n}_p$ and variance var(n_p)= $\bar{n}_p$. The mean number of primary beam electrons within time τ can be estimated by

$$\bar{n}_p = \frac{I_p \tau}{e}$$

(1.2)

where I_p is the primary beam current. The signal-to-noise ratio of the primary beam electrons is given by

$$SNR_{PE} = \frac{\overline{n}_p}{\left[\text{var}(n_{p})\right]^{1/2}} = \overline{n}_p^{1/2} = \left(\frac{I_p\tau}{e}\right)^{1/2} = \left(\frac{I_p}{2e\Delta f}\right)^{1/2}$$ (1.3)

where Δf is the bandwidth of the detector system, $\Delta f = 1/2\tau$.

In the case of backscattered electrons (BSEs), the BSE distribution obeys a binomial distribution with a backscattering coefficient η. The cascade of the Poisson distribution of the PE and the binomial distribution of the BSE results in the signal-to-noise ratio of the BSE as [1.32]

$$SNR_{BSE} = \left(\frac{I_p\tau\eta}{e}\right)^{1/2} = \left(\frac{I_p\eta}{2e\Delta f}\right)^{1/2}$$ (1.4)

Similarly, for Auger electrons, having a yield, Y_A, the signal-to-noise can be estimated as

$$SNR_{AE} = \left(\frac{I_p\tau Y_A}{e}\right)^{1/2} = \left(\frac{I_p Y_A}{2e\Delta f}\right)^{1/2}$$ (1.5)

The distribution of secondary electrons (SEs) is more complicated because one PE can excite zero, one, or more SEs with decreasing probability. The SE signal-to-noise ratio is given by [1.32]

$$SNR_{SE} = \left(\frac{I_p\tau}{e(1+b)}\right)^{1/2} = \left(\frac{I_p}{2e\Delta f(1+b)}\right)^{1/2}$$ (1.6)

where b is the noise factor. In the case of a low SE yield, δ, at very low PE energies, the process is approximately a Poisson distribution where $b \approx 1/\delta$. At a high SE yield (for PE beam of 10-20 keV), there is a deviation from the Poisson distribution and the value of b becomes larger than this value by a factor of 1.2 to1.5.

The number of scattered electrons travelling through an energy analyzer to the

detector is much smaller than the total number of electrons scattered from the specimen, depending on the transmission and the energy resolution of the analyzer. For typical energy analyzers with a transmission of less than 20% and an energy window of less than 1%, the detected signal after the analyzer is much less than 1% of the total signal scattered from the specimen. Additionally, the signal-to-noise ratio is reduced by the detector quantum efficiency, typically less than 50%. For a primary beam current of a few pAs to nAs, an acquisition time of tens to hundreds of milliseconds is usually required for a reasonable SNR (>3) [1.25].

1.5   Previous electron spectrometers for the SEM

Electron energy spectrometers have already been designed for the SEM over a few decades, however, they were limited in terms of their range of applications and performance. As already mentioned, most of them were made for the purpose of quantifying voltage contrast. Retarding field analyzers, which collect the SE energy spectrum as an integrated form of signal (S-curve), and monitor the changes of the specimen voltage as signal shifts as illustrated in Fig. 1.12, were most widely used for this purpose. An early voltage contrast retarding field analyzer using a hemispherical retarding grid was proposed by Fentem and Gopinath [1.33], and later ones, using planar grids, were reported by Plows [1.34], Flemming and Ward [1.35], and Gopinath and Sanger [1.36]. For over a decade, from 1970, retarding field analyzers were placed below the objective lens, and used as add-on attachments for the SEM. One major drawback of these voltage contrast spectrometers is that they needed to be placed below the SEM objective lens, and as a result, inevitably increased the working distance, limiting the image resolution that could be attained.
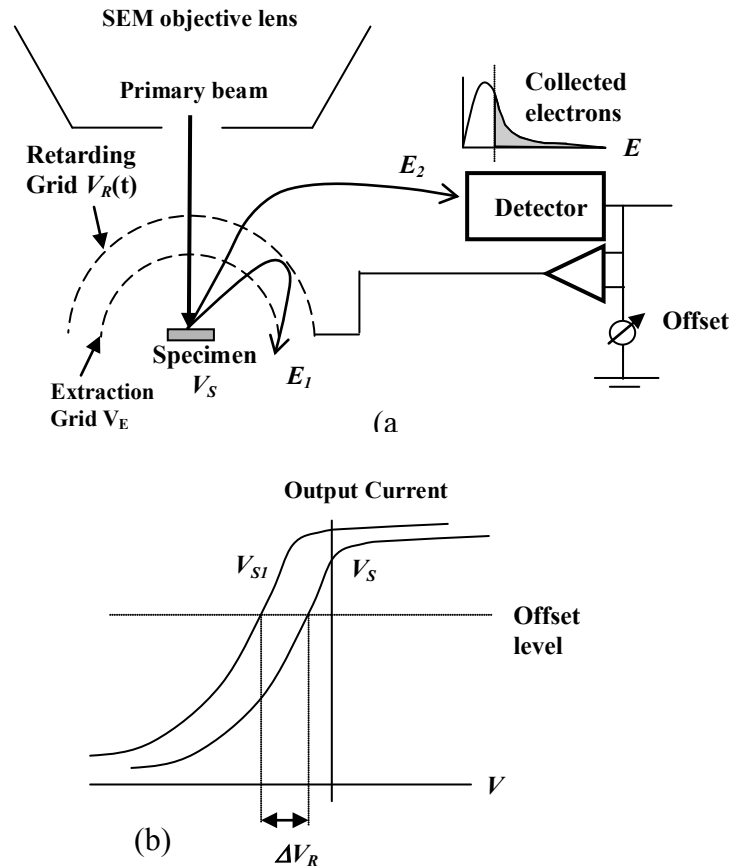
Fig. 1. 12. Principle of closed loop retarding field spectrometers for voltage contrast: (a) Spectrometer layout; (b) Output S-curve signals

From the 1980s, better objective lenses were proposed for the SEM with better electron optical performance such as immersion magnetic objective lenses, and voltage contrast spectrometer designs were consequently proposed for these kinds of objective lenses. Examples of these spectrometers were proposed by Menzel and Buchanan [1.37], Garth [1.38], Frosien and Plies [1.17], Dinnis [1.39]. They had much smaller working distances (typically 2–5 mm) than the previous retarding field analyzers, which were placed below the objective lens. These "through-the-lens" voltage contrast spectrometers as well as the previous retarding field analyzers, were not used for the purpose of capturing the energy spectrum of scattered electrons, they were designed to monitor shifts in the secondary electron (SE) spectrum. Their design

and performance, usually characterized by a voltage resolution constant [1.9], and is not directly relevant to the new emerging spectroscopic applications inside the SEM, such as p-n junction mapping or acquisition of the Auger electron spectrum. More details on voltage contrast spectrometers can be found in the references [1.9][1.40].
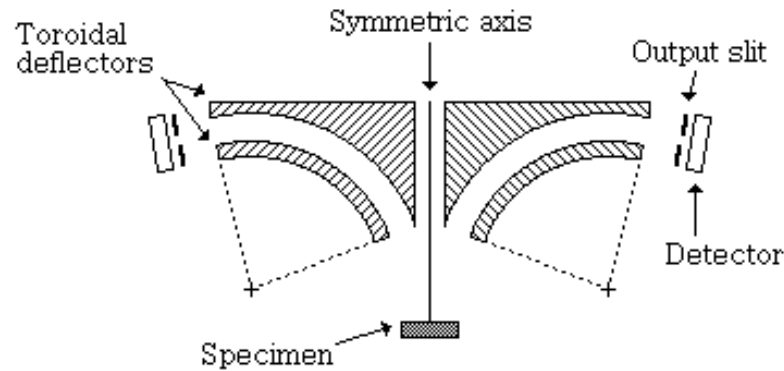
Fig. 1. 13. Schematic diagram of Rau spectrometer for the SEM

Apart from voltage contrast spectrometers, very few other spectrometers have been proposed for the SEM. Rau and Robinson designed an electrostatic toroidal deflection analyzer attachment for the SEM [1.12-1.13], as depicted in Fig. 1.13, to capture the BSE spectrum scattered from the specimen under test. This analyzer attachment is placed in between the objective lens and the specimen, resulting in a large working distance. Therefore, it is not suitable for spectral applications on the nano-scale range. Its performance is characterized by first order optics, and the energy resolution was measured to be 2.5% for a reasonable electron intensity at the detector [1.41], considerably worse than those normally used for Auger analysis (<0.3%).

All in all, the energy spectrometers for the SEM so far, which include voltage contrast spectrometers and Rau and Robinson toroidal spectrometer, are not suitable for the new approaches of acquiring scattered electron spectrum for nano-scale analysis

inside the SEM. There is a need to look for new electron energy spectrometer improvements in the SEM.

1.6   Objectives of the thesis

This thesis aims to design different high performance electron energy spectrometer attachments for SEMs in order to improve their spectroscopic capability. Different electron energy spectrometers will be designed for various types of SEMs, including existing conventional objective lens SEMs and high imaging resolution immersion objective lens SEMs. Their target performance, in terms of energy resolution and transmittance, is to be better than present Auger electron spectrometers, such as the CMA and HDA. The thesis also sets out to design parallel energy acquisition analyzers for the SEM. Numerical simulation techniques will be used to design analyzers, and proof-of-concept experimental prototypes will be made and tested inside existing SEMs.

1.7   Scope of the thesis

This thesis is divided into five chapters. Chapter 2 describes a parallel electron energy acquisition spectrometer, called the circular magnetic beam separator spectrometer. This spectrometer is designed for the mixed-field immersion objective lens SEM. Chapters 3 and 4 present two rotationally symmetric electrostatic electron energy spectrometers for conventional SEMs. In Chapter 3, simulation of a second-order focusing toroidal spectrometer as well as experimental results from its prototype SEM attachment are discussed in detail. In Chapter 4, simulation results of a radial mirror analyzer (RMA) for the SEM are reported. Some suggestions for future work and the conclusions of the thesis are presented in Chapter 5.

References

1.1   J. Golstein, D. E. Newbury, D. C. Joy, C. E. Lyman, P. Echlin, E. Lifshin, L. Sawyer, and J. R. Michael, "Scanning Electron microscopy and x-ray microanalysis", Springer, 3rd edition (2003).

1.2   T. Luo, and A. Khursheed, " Elemental identification using transmitted and backscattered electrons in a SEM", Physics Procedia 1 (2008)155-160.

1.3   E. I. Rau, and V. N. E. Robinson, " An annular toroidal backscattered electron energy analyser for use in scanning electron microscopy", Scanning, 18 (1996) 556-561.

1.4   P. Kazemian, S. A. Mentink, C. Rodenburg, and C.J Humphreys, "High resolution quantitative two-dimensional dopant mapping using energy-filtered secondary electron imaging", J. Appl. Phys. 100 (2006) 054901.

1.5   P. Kazemian, S. A. M. Mentink, C. Rodenburg and C. J. Humphreys, "Quantitative secondary electron energy filtering in a scanning electron microscope and its applications", Ulramicroscopy. 107, 140 (2007).

1.6   X. Zha, C.G.H. Walker, M.M. El Gomati, A magnetic electron energy analyser for fast data acquisition", Nucle. Instru. Method. Phys. Res A. (2010) doi:10.1016/j.nima.2010.12.139

1.7   M.M. El Gomati, C.G.H. Walker, X. Zha, "Towards quantitative scanning electron microscopy: Applications to Nano analysis", Nucle. Instru. Method. Phys. Res A. (2010)

1.8   D. Cubric, A. DeFanis, I. Konishi, S. Kumashiro, "Parallel acquisition electrostatic electron energy analyzers for high throughput nano-analysis", Nucle. Instru. Method. Phys. Res A. (2010) doi:10.1016/j.nima.2010.12.055.

1.9   A. Khursheed, "Scanning electron microscope optics and spectrometers", World Scientific (2010).

1.10   H. P. Feuerbaum, "VLSI testing using the electron probe". Scan Electr Microsc, SEM inc. I (1979) 285.

1.11   M. Jacka, and M. Kirk, M. M. El Gomati and M. Prutton, " A fast parallel acquisition electron energy analyzer: The hyperbolic field analyzer", Rev. Sci. Instrum. 70 (1999) 2282.

1.12   E. I. Rau, and V. N. E. Robinson, "An annular toroidal backscattered electron energy analyser for use in scanning electron microscopy", Scanning, 18 (1996) 556-561.

1.13   E. I. Rau, A. Khursheed, A. V. Gostev, and M. Osterberg, "Improvements to the design of an electrostatic toroidal backscattered electron spectrometer for the scanning electron microscope", Rev. Sci. Instrum. 73 (2002) 227-229.

1.14   A. Khursheed, "Recent development in scanning electron microscope design", Advances in Imaging and Electron Physics, Vol 15, edited by P. W. Hawkes. San Diego: Academic Press, 197-285.

1.15   M. Kienle and E. Plies," An off-axis multi-channel analyzer for secondary electrons", Nucl. Instrum. And Method. in Res. A 519, (2004) 325.

1.16   Meisberger et al, "Electron beam inspection system and method", US patent 5,578,821 (1996).

1.17   J. Frosien, and E. Plies, "High performance electron optical column for testing ICs with submicrometer design rules", Microelectronic Engineering 7 (1987)163-172.

1.18   P. Kruit, J. A.Venables, "High spatial resolution surface-sensitive electron spectroscopy using a magnetic parallelizer". Ultramicroscopy 25 (1988) 183.

1.19   H. Z. Sar-El, "Cylindrical Capacitor as an Analyzer I. Nonrelativistic Part", Rev. Sci. Instrum. 38 (1967) 1210.

1.20   P. W. Palmberg, G. K. Bohn, and J. C. Tracy, " High sensitivity auger electron spectrometer", Appl. Phys. Lett. 15 (1969) 254.

1.21   H. Hafner, J. A. Simpson, and C. E. Kuyatt, "Comparison of the Spherical Deflector and the Cylindrical Mirror Analyzers", Rev. Sci. Instrum. 39 (1968) 33.

1.22   J. S. Risley, "Design parameters for the cylindrical mirror energy analyzer", Rev. Sci. Instrum 43 (1972) 95.

1.23   H. Z. Sar-El, "Criterion for Comparing Analyzers", Rev. of Sci. Instrum., 41 (1970) 561.

1.24   E. H. A. Granneman, andM. J. Van Der Wiel, "Transport, dipersion and detection of electrons, ions and neutrals, chapter 6 of Handbook on Synchrotron Radiation, edited by E. E. Koch, North Holland publishing company (1983).

1.25   M. Prutton and M. M. El Gommati, "Scanning Auger Electron Microscopy" , John Wiley and Sons Ltd , UK (2006).

1.26   T. J. M. Zouros, and E. P. Benis, "The hemispherical deflector analyser revisited. I. Motion in the ideal 1/r potential, generalized entry conditions, Kepler orbits and spectrometer basic equation", J. Electron. Spectrosc. Relat. Phenom, 125 (2002) 221.

1.27   E. P. Benis, and T. J. M. Zouros, "The hemispherical deflector analyser revisited II. Electron-optical properties", J. Electron. Spectrosc. Relat. Phenom, 163 (2008) 28.

1.28   J. K. Swenson' "A high resolution projectile electron spectrometer", Nucl. Instrum. And Method. in Res. B. 10-11 (1985) 899.

1.29   M. Jacka, A. Kale and N. Traitler, "Hyperbolic field electron analyzer with second order focussing", Rev. Sci. Instrum. 74 (2003) 4298.

1.30   F. H. Read, "The parallel cylindrical mirror electron energy analyzer", Rev. Sci. Instrum. 73 (2002) 1129.

1.31   F. H. Read, D. Cubric, S. Kumashiro and A. Walker, "The parallel cylindrical mirror analyzer axis-to axis configuration" Nucl. Instrum. and Meth. in Phys. Res. A 519 (2004) 338.

1.32   L. Reimer, "Scanning electron microscopy: Physics of image formation and microanalysis", Springer, 2rd Ed (1998).

1.33   P. J. Fentem, andA. Gopinath, "Voltage contrast linearization with a hemispherical retarding analyzer", J. Phys. E: Sci. Instrum. 1 (1974) 930-933

1.34   G. S. Plows, "Stroboscopic scanning electron microscopy and the observation of microcircuit surface voltage", PhD thesis, Cambridge University, UK (1969)

1.35   J. P. Flemming, and E. W. Ward, "A technique for accurate measurement and display of applied potential distributions using the scanning electron microscope", Scanning Electron Microscopy (1970) 465-470.

1.36   A. Gopinath, A. "Estimate of minimum measurable voltage in the SEM", Journal of Physcis E: Scientific Instruments 10 (1977) 911-913

1.37   E. Menzel, E. and R. Buchanan, "In-the-lens secondary electron analyser for IC internal voltage measurements with electron beams", Electronics Letters 20 (1984) 408-9

1.38   S. C. J. Garth, S. C. J, "In-the-lens electron spectrometers for E-beam testing: A Review", Microelectronic Engineering 6 (1987) 667-672.

1.39   A. R. Dinnis, "Detectors for quantitative voltage contrast on submicron devices", Microelectronic Engineering 7 (1987) 139-146.

1.40   J. T. L. Thong, "Electron Beam Testing Technology", Plenum Press, NY (1993)

1.41   D. Berger, M. Filippov, H. Niedrig, E.I. Rau, F. Schlichting, "Experimental determination of energy resolution and transmission characteristics of an electrostatic toroidal spectrometer adapted to a standard scanning electron microscope", J. Electron. Spectrosc. Relat. Phenom. 105 (1999) 119.

Chapter 2: A circular magnetic beam separator spectrometer

2.1   Introduction

This chapter aims to describe a parallel electron energy acquisition spectrometer design for a mixed field immersion objective lens SEM. As discussed in Section 1.3, a mixed-field immersion objective lens, which gives the highest image resolution of all immersion lens designs [2.1], has the difficulty of separating scattered electrons from the primary beam, Wien filters are usually used for this purpose.

Based upon the use of Wien filters, Kienle and Plies proposed a parallel energy multichannel secondary electron (SE) analyzer design for a mixed field objective lens [2.2]. In their design as depicted in Fig. 2.1, the primary beam travels through most the column and is decelerated down to a landing voltage of 1 kV at the specimen. SEs are typically accelerated to 8 kV as they travel back up the column, and are deflected off-axis by a Wien filter. They are then further deflected and dispersed by an electric spherical deflector analyzer (SDA), after which their image is magnified and focused on to a YAG scintillator to generate a light image, which is captured by a CCD placed behind the scintillator. The whole spectrum of SEs from 0 to 20 eV can be simultaneously captured. This design can also be set to another operating mode, where it captures the BSE.

The Kienle and Plies spectrometer has the disadvantage of requiring a complicated redesign of the electron column. Another Wien filter needs to be placed further up the column, in order to cancel out adverse energy dispersion and second-order

geometrical aberration effects on the primary beam. In addition, several stages of magnifying the energy dispersion are also required, since the lower Wien Filter only deflects the secondary electron beam by 15°, and the SDA is limited to a deflection angle of 75°.
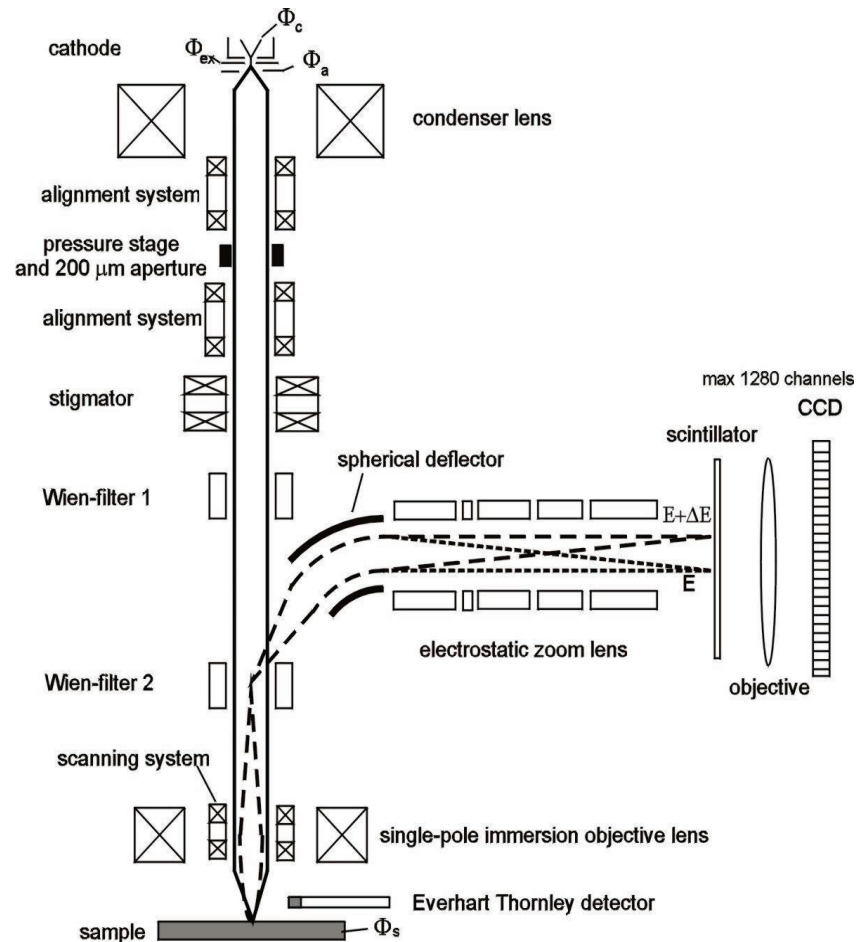
Fig. 2. 1. Schematic layout for the multi-channel secondary electron off-axis analyzer reported by Kienle and Plies [2.2].

Apart from the use of Wien filters for separating scattered electrons from the primary beam, there have been so far, two other parallel energy acquisition electron spectrometer proposals for immersion objective lenses that utilize magnetic sector beam separators for separating scattered electrons from the primary beam. Mankos

proposed a curved axis scanning electron microscope design in his patent [2.3], which operates in a spectroscopic mode for parallel electron energy acquisition. The design is based upon the use of a square magnetic sector beam separator [2.4]. The most important characteristic of this beam separator is that it can focus the primary beam stigmatically, (stigmatic focusing of an electron beam is characterized by two conditions: the focusing positions and the exit semi-angles must be the same in both in-plane and out-of-the plane). This proposal utilizes a curved axis instead of a straight optical axis down the electron optical column as shown in Fig. 2.2. The primary electron beam from the column is bent 90° by the beam separator and focused on to the specimen by the objective lens system. The scattered electrons emitted from the substrate are extracted through the objective lens and sent into the magnetic beam separator. Within the beam separator, they are bent so as to be oriented towards the detector system.   The scattered electrons including secondary electrons, Auger electrons, plasmon electrons and backscattered electrons are accelerated and collimated by the objective lens. A transfer lens is used to create a certain energy dispersion at the image plane.   If a linear array or a two-dimensional array of detection elements is placed at the image plane, the full energy spectrum of scattered electrons can, in principle, be monitored. However, no details of this proposal have been published, especially with respect to the objective lens and transfer lens, which must achieve sufficient energy dispersion in order to separate electrons in the entire scattered energy range with adequate energy resolution at the detector.
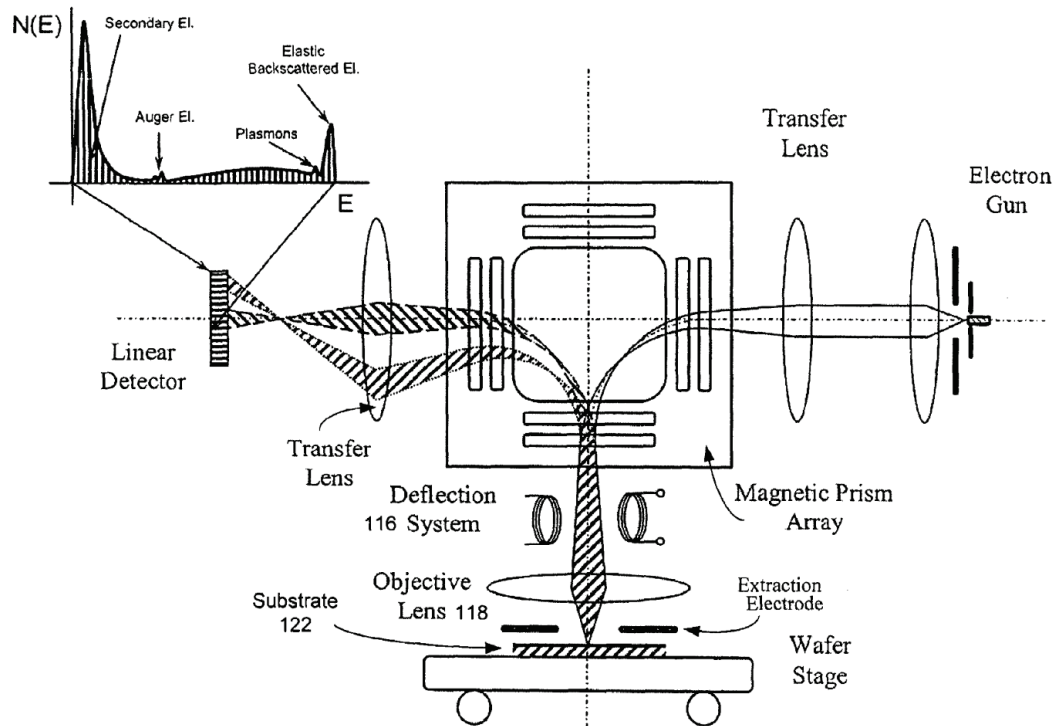
Fig. 2. 2. A curved axis scanning electron microscope proposed by Mankos [2.3].

The other (more complete) parallel energy acquisition electron spectrometer proposal, designed to capture the entire energy range of scattered electrons leaving the specimen, has been reported by Khursheed and Osterberg for the SEM [2.5-2.6]. The layout of their magnetic beam separator spectrometer is depicted in Fig. 2.3. At the heart of the design, there is a circular magnetic sector deflector, which can deflect the primary beam stigmatically (preserves a round beam shape), and acts as a beam separator [2.7]. The design uses a conventional SEM column (electron gun, condenser lens and scanning coils), to project a focused primary beam into the center of a magnetic sector deflector that bends it by 90°, which then goes on to strike the specimen in the normal vertical direction. The specimen in this case is located inside an objective lens, integrated within the specimen chamber. The proposed objective

lens is a mixed electrostatic and magnetic immersion lens that is able to provide high

image resolution at low landing energies [2.1].
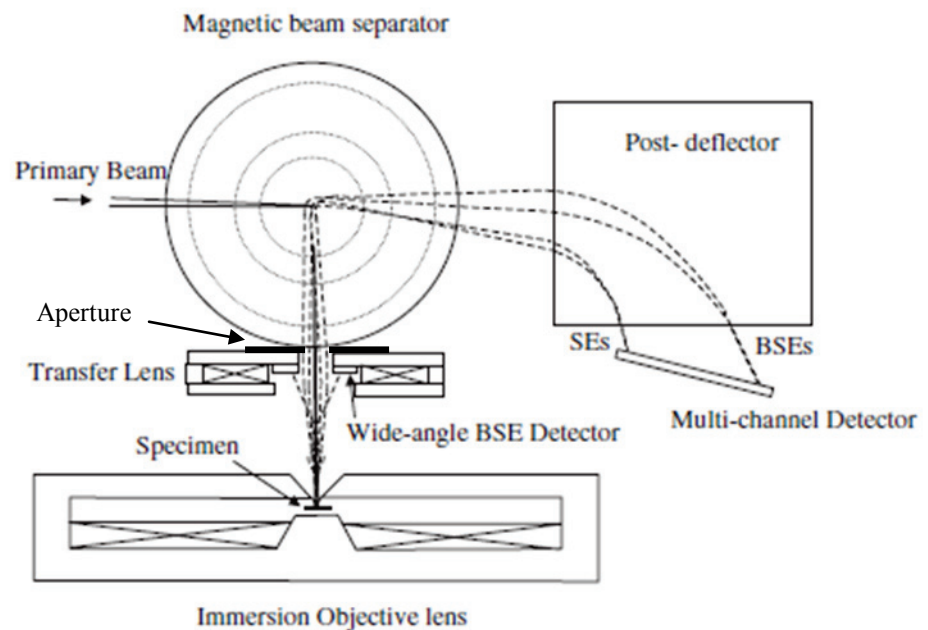
Fig. 2. 3. A magnetic beam separator spectrometer layout principle for full range energy acquisition proposed by Khursheed and Osterberg [2.6]

Scattered electrons are accelerated by the objective lens towards the magnetic sector

beam separator. They are then deflected away from the primary beam and separated

by the magnetic sector beam separator according to their different emission energies.

The transfer lens will tend to focus the scattered electrons to some degree, but there is

no distinct focal point because of the energy spread. Once separated from the primary

beam, it is easy to further disperse the scattered electrons before capturing them. A

post-deflector unit is used to direct and focus them on to a multi-channel detector,

where their spectrum will be monitored in parallel. In principle, all the scattered

electrons including secondary electrons, Auger electrons, and backscattered electrons

can be separated and collected independently because of their different kinetic

energies. However, in order to attain higher energy resolution, an array of electron

detectors/spectrometers can be arranged around the beam separator. These post-

deflector units can be designed to focus the scattered electrons on to a parallel array of detectors. In this way, scattered electrons are essentially unrestricted by space constraints and are expected to be collected with high transport efficiency.

Khursheed and Osterberg [2.5-2.6] did not complete their proposal, in terms of simulation designs and proof-of-concept spectroscopic experiments. The electron energy spectrometer design proposed in this chapter naturally follows on from their proposal. This work aims to use the circular magnetic beam separator to separate scattered electrons from the primary beam and to design a complete electron spectrometer system that can capture the entire energy range of scattered electron emission in parallel with high energy resolution and high transmission efficiency.

The previous work, carried out by Khursheed and Osterberg dealt mainly with the primary beam optics aspects of the spectrometer, while providing preliminary simulations in two dimensions for the scattered electrons trajectory ray paths (Fig. 2.3). They designed the magnetic beam separator to have low primary beam aberrations, and confirmed this by experiment [2.7-2.8]. However, the energy dispersion of the scattered electrons and a scheme to detect them with high energy resolution and high transmittance has not been made. In the following work, ray tracing in three-dimensions will be performed, from which the spectrometer energy resolution and transmittance characteristics can be predicted in detail. In addition, a complete post-deflector arrangement will be designed to capture the whole energy range and optimize energy resolution. Simulation software will be written so that curved edged mixed field (electric/magnetic) post-deflectors can be modeled in three dimensions; the previous simulation was limited to a straight-edged magnetic post-

deflector in two dimensions. To test these simulation predictions, a prototype spectrometer will be made and tested as an attachment inside a conventional SEM, to acquire scattered electron spectra.

2.2 Simulation design of a circular magnetic beam separator spectrometer for full range parallel energy spectral acquisition.

The spectrometer design proposed here, like the one reported by Khursheed and Osterberg [2.5-2.6], uses a circular magnetic sector deflector as a beam separator, which bends the primary beam through 90º, and directs it into a mixed field electric/magnetic immersion lens. However, in this case, the transfer lens is designed to focus scattered electrons into the beam separator in order to maximize energy dispersion and minimize angular dispersion. The beam separator acts as the first stage of an energy spectrometer, subsequent first-order focusing on to multi-channel detectors will be achieved through the use of additional magnetic sector/retarding field units, ones that capture scattered electrons over their entire range with high energy resolution and transport efficiency.

2.2.1 Objective and transfer lens designs

The beam separator spectrometer to be designed here, is one that is specifically meant to fuction with the SEM objective lens that combines an electrostatic retarding field with a magnetic field. This type of objective lens has much lower focal lengths and on-axis aberrations than conventional objective lenses, and is particularly suited to provide high resolution at low landing energies [2.1]. Fig. 2.4 depicts finite-element solved field distributions for the objective/transfer lens combination. All such field distributions, as well as the plotting of trajectory paths through them, were obtained

by running programs from the KEOS package [2.9]. The upper pole-piece of the objective lens has a 2 mm diameter hole through which the primary beam and scattered electrons pass. The distance to the specimen from the upper pole-piece of the objective lens is also 2 mm. The objective lens coil current excitation was adjusted to focus a 10 kV primary beam on to the specimen. The primary beam is assumed to start 50 mm above the transfer lens, corresponding to the beam separator centre.
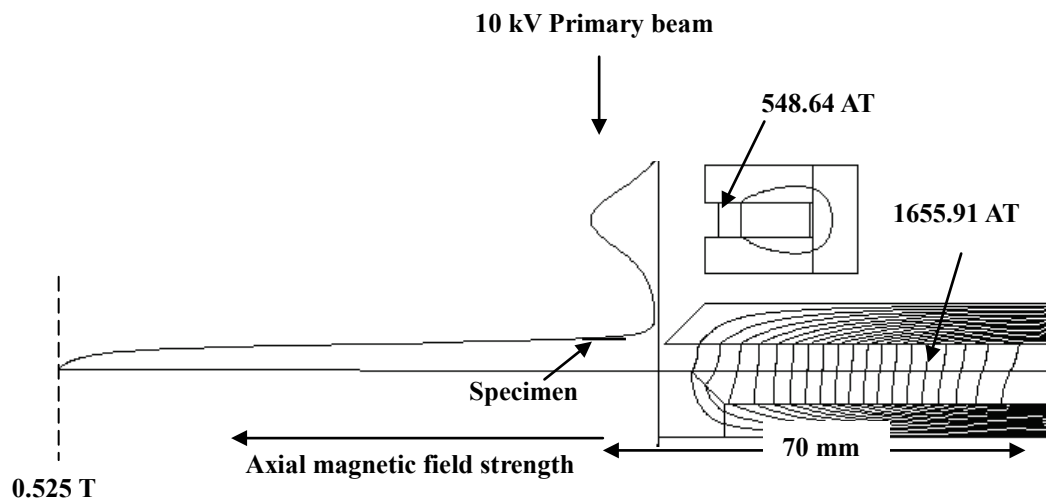
(a)
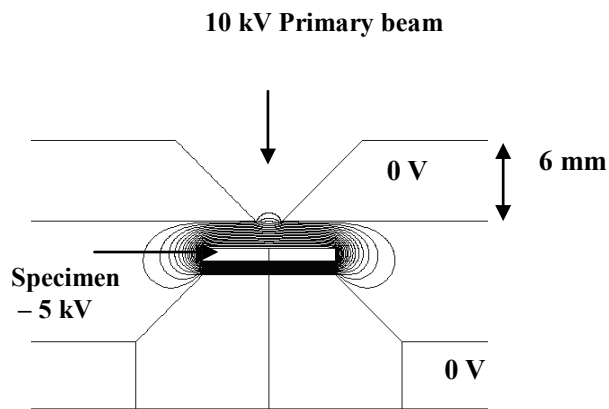
(b)

Fig. 2. 4. Numerically solved lens field distributions required to focus a 10 kV primary beam on to a specimen with 5 keV landing energy: (a) Magnetic; (b) Electrostatic
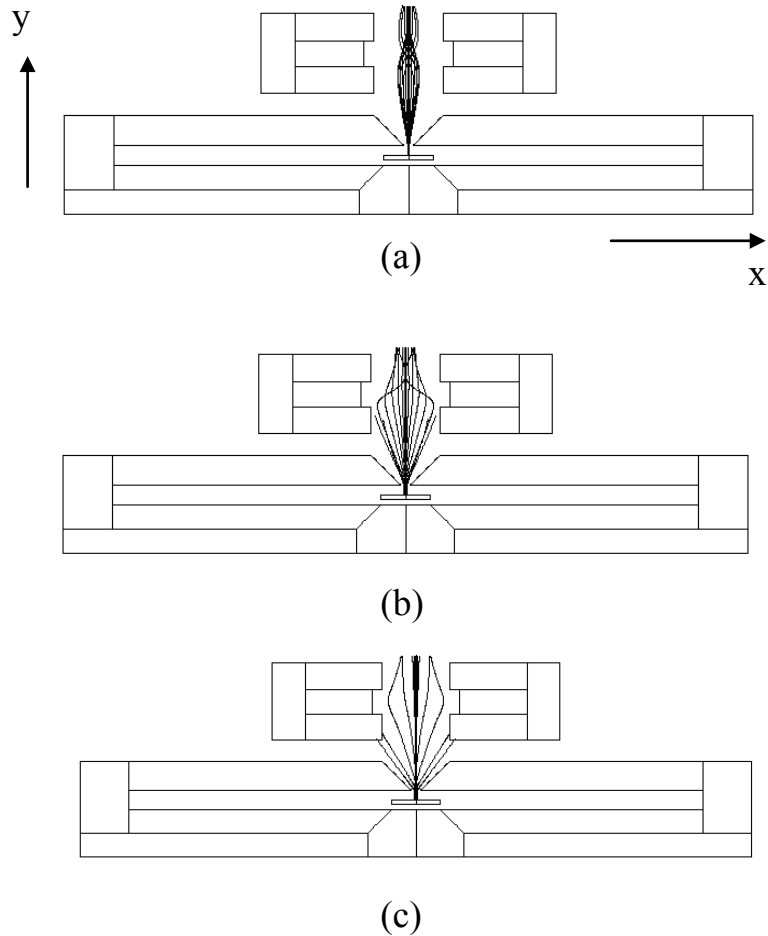
Fig. 2. 5. Simulated scattered electron trajectory paths through objective and transfer lenses for emission angles ranging from 0 to 1.4 rad in 0.2 rad steps: (a) 500 eV; (b) 2 keV; (c) 5 keV (BSE)

Fig. 2.5 shows simulated trajectories of scattered electrons leaving the specimen with emission energies of 500 eV, 2 keV and 5 keV (BSE) over a wide range of emission angles relative to the optical axis (0 to 1.4 radians). The low energy secondary electrons (< 5 eV) were not plot since they remain much closer to the optical axis (within a radius of 0.5 mm). The trajectory paths shown in Fig. 2.5 illustrate how the transfer lens focuses the scattered electrons into the beam separator. In general, the point to which the transmitted scattered electrons focus will depend on their emission energies, however, an energy range corresponding to focal points 20 mm around the beam separator centre (40% of the beam separator radius) will result in scattered

electrons having a reduced angular spread at the detector plane. This is the main benefit of using the transfer lens, and will be discussed more in detail in the following pages. The excitations on the objective/transfer lenses used for the direct ray tracing, as indicated in Fig. 2.5, focuses 1-2 keV Auger electrons emitted within the angular range from 0 to 0.4 radians to approximately within 20 mm of the beam separator centre. The near-axis elastic backscattered electrons are of course, naturally directed into the beam separator because they retrace the path of the primary beam.

2.2.2 Field distribution simulation for post-deflector simulated designs

Simulation of the spectrometer's characteristics requires accurate ray tracing of electron trajectory paths through curved electric/magnetic sector plates. Since magnetic sector field distributions are inherently three-dimensional in nature, and often involve curved boundaries, direct ray tracing of electrons through them is a non-trivial task. Numerical field solving techniques such as the finite element method do not in general provide enough accuracy to extract aberration coefficients from the trajectory paths of focused beams in three dimensions. This is because numerical meshes in three dimensions that model complex shaped boundaries typically need over a million free nodes, requiring prohibitively large amounts of computer memory and unmanageably long program run times [2.10]. The situation is made even more difficult for retarding sector units, where an electric field is overlaid onto the deflecting magnetic field in order to slow down electrons to very low energies (a few eV). Another disadvantage of using a fully finite element approach is that high-order interpolation methods are needed to extract accurate field information from nodal potentials, so, mesh-less methods are preferred [2.10].

A three-dimensional semi-analytical technique, which uses a modified two-dimensional finite element solution in combination with a Fourier Series expansion, to simulate 3D potential field distributions, has been developed for this work. This approach avoids the direct use of a fully three-dimensional finite element solution, helping simulate easily and accurately three-dimensional curved mixed field post-deflectors, and has the desirable feature of not requiring a mesh in the region where electron trajectories are to be plotted. Details of this method can be found in the Appendix A.

2.2.3   The circular magnetic beam separator

The circular beam separator is designed to have the same focusing properties on primary beam electrons traveling both in the plane of deflection (x-y), "in-plane", and in the direction perpendicular to it (x-z), "out-of-plane". It achieves this stigmatic focusing property by segmenting the deflection plates, like the square beam separator proposed by Mankos illustrated in Fig. 2.1, using a pair of inner plates and a pair of outer plates, as shown in Fig. 2.6. The diameter of the beam separator is 100 mm, and the gap between each pair of sector plates in the out-of plane direction (z direction) is 10 mm. The excitations on the inner and outer plates necessary to provide stigmatic focusing of 10 keV primary beam deflected through 90° are 85.85 AT and -12.14 AT respectively, (see Ref. [2.7] for more details on simulating the primary beam aberrations through this beam separator).

Simulated trajectories of scattered electrons traced through the beam separator, after passing through the transfer lens are shown in Fig. 2.6. It indicates that the angular spread effect is relatively small for the lower energy scattered electrons (represented

by 50 eV in this instance), and for the 2 keV electrons. The accelerating field at the specimen surface is responsible for reducing angular dispersion on the lower energy electrons, while the transfer lens focusing effect reduces it for the 2 keV electrons. For the backscattered electrons, the near-axis emission angle electrons clearly have a small amount of dispersion.
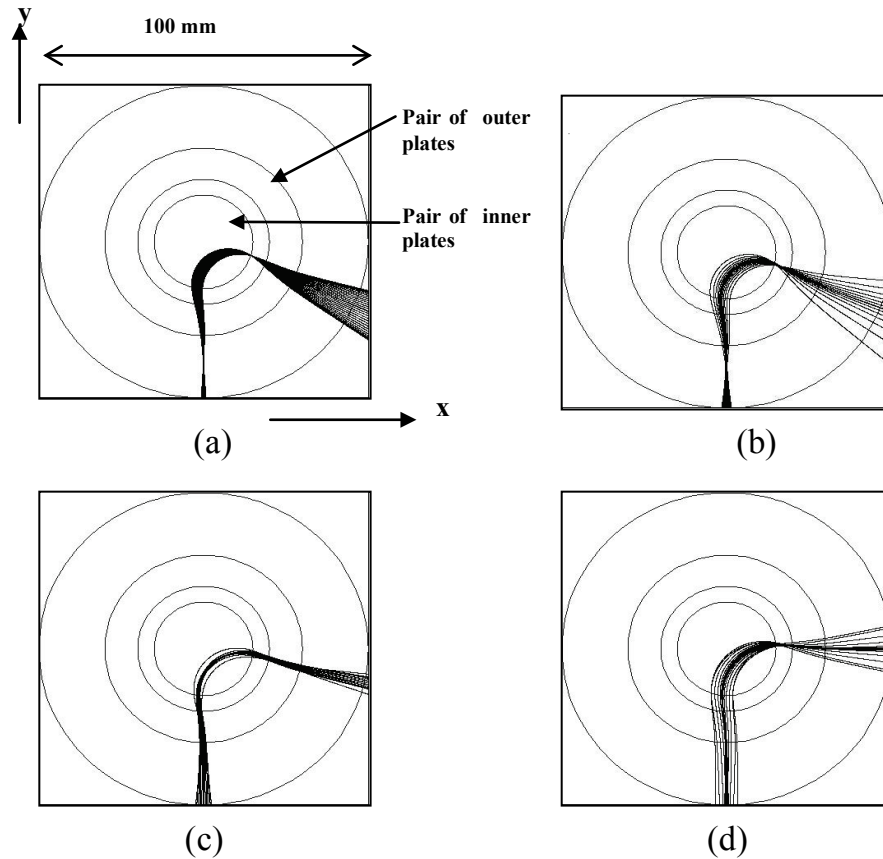
Fig. 2. 6. Simulated in-plane (x-y) scattered electron trajectory paths through the beam separator for a variety of different emission conditions at the specimen. Emission angles are plot in 0.1 radian steps: (a) 50 eV, 0 to 1.5 radians; (b) 500 eV, 0 to 0.6 radians; (c) 2 keV, 0 to 0.7 radians and (d) 5 keV, 0 to 0.9 radians

The aperture placed just below the beam separator restricts the in-plane angular dispersion of the scattered electrons over a wide range of emission energies. For a 2.7 mm wide aperture, the emission angles of scattered electrons that enter the beam separator are limited to 0.4 radians for electrons emitted with energies between 0.5 to

2 keV, 0.5 radians for 3 keV, and 0.7 radians for the backscattered electrons (5 keV).

The angular dispersion of backscattered electrons, however, is further limited by its

post-deflector geometry, effectively providing a 0.6 radian cut-off emission angle.

Note that the aperture acts only to restrict the angular dispersion in the plane of

deflection.
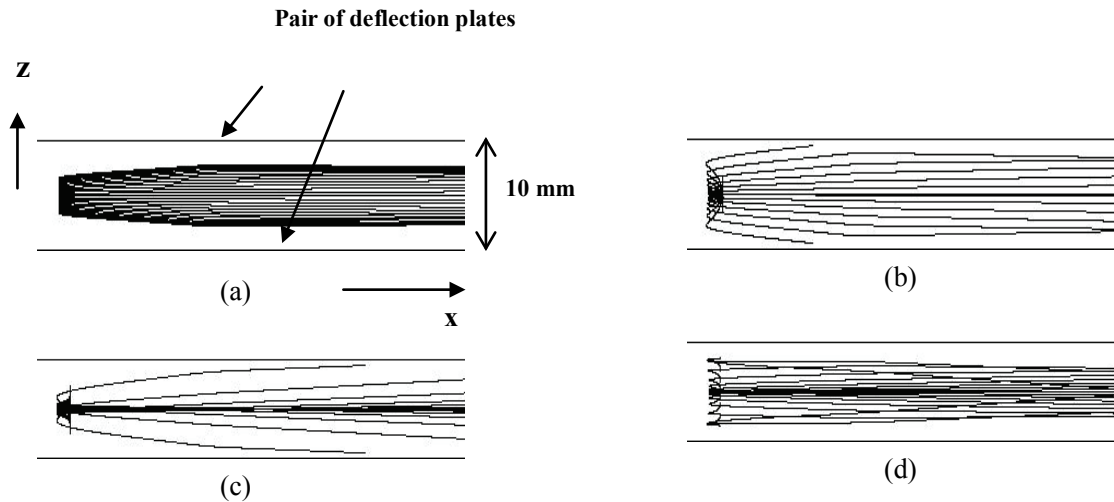
Fig. 2. 7. Simulated out-of-plane (x-z) scattered electron trajectory paths through the beam separator for a variety of different emission conditions at the specimen. Emission angles are plot in 0.1 radian steps: (a) 50 eV, 0 to 1.5 radians; (b) 500 eV, 0 to 0.6 radians; (c) 2 keV, 0 to 0.7 radians; (d) 5 keV, 0 to 0.9 radians.

In the out-of-plane direction, the beam separator dimensions largely determine the

cut-off angle. For a 10 mm gap between each pair of sector plates, the out-of-plane

cut-off angles on scattered electrons are: $\pi/2$ radians for 50 eV, 0.55 radians for 500

eV to 1 keV, 0.65 radians for 2 keV, 0.85 radians for 3 keV, and 0.95 radians for 5 keV

(the backscattered electrons). These results are indicated by the trajectory paths shown

in Fig. 2.7. Obviously, to increase transmission in the out-of-plane, the beam separator

size can be increased, and there is no fundamental limit to transmission of the

scattered electrons in the out-of-plane direction. For the in-plane direction however,

the transmitted scattered electron angular dispersion must be selectively reduced in

order to improve the attainable energy resolution at the detector plane.

2.2.4   Post-deflectors

The post-deflectors considered here, consist of magnetic sector deflectors that incorporate with an electric retarding unit, slowing down electrons as they travel through the deflector. By using the semi-analytical approach for mixed field distributions, these magnetic/electric retarding sector units can be accurately simulated. The advantage of this design is that it increases the energy dispersion of scattered electrons through the deflector, that is, scattered electrons separate more than they would do if a normal magnetic sector deflector is used. For example, scattered secondary electrons can be slowed down by the retarding field even to a few eVs, making them easy to deflect even with a weak magnetic field. At the same time, backscattered electrons go through these deflectors with only a slight influence to their trajectories, due to their much larger kinetic energy, and can then be detected separately.

2.2.5   Energy dispersion properties of beam separator spectrometers

Fig. 2.8 and Fig. 2.9 depict trajectory paths of scattered electrons that leave a -5 kV specimen and travel through a beam separator spectrometer layout that is designed to capture a wide-range of energies. Three magnetic sector post-deflectors separate scattered electrons according to their emission energies. This is represented in simulation by emission energies 3, 500, 1000, 2000, 3000 and 5000 eV. Due to the -5 kV biasing of the specimen, these electrons have kinetic energies of 5.003, 5.5, 6, 7, 8 and 10 keV respectively as they travel through the beam separator and arrive at their respective detectors. Note that the 3 eV secondary electrons are mirrored back into the beam separator for a second pass.
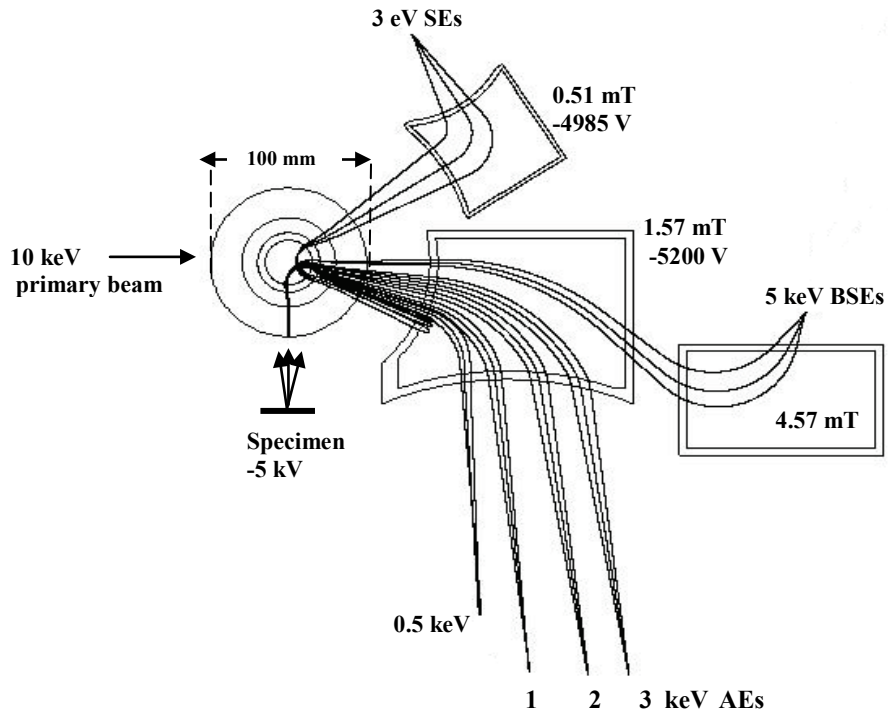
Fig. 2. 8. Direct ray tracing of scattered electrons at a variety of different emission energies that emanate from a source located 5 cm below the beam separator and have angles ± 5 mrad diverging from the vertical axis.
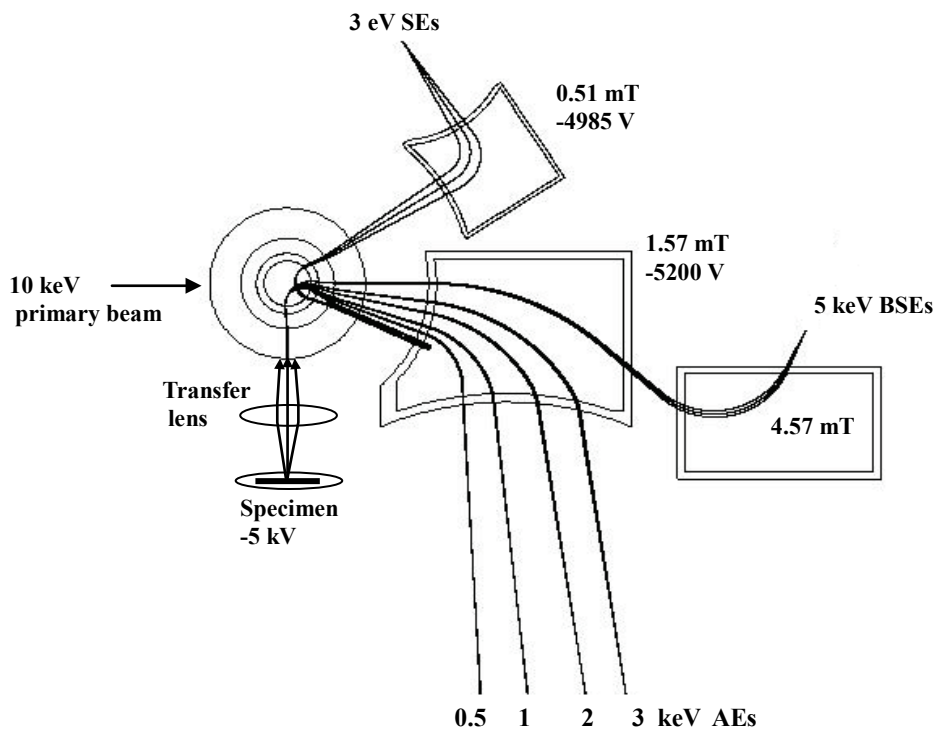
Fig. 2. 9. Direct ray tracing of scattered electrons at a variety of different emission energies that converge towards the centre of the beam separator with entrance angles of ±5 mrad.

In Fig. 2.8, all scattered electrons are assumed to enter the beam separator with diverging ± 5 mrad angles emanating from a point source located 50 mm below it. In Fig. 2.9, they enter the beam separator with ± 5 mrad angles converging towards its centre. Exclusion of the objective/transfer lens system is deliberated here in order to better understand how to minimize angular dispersion through beam separator. On comparing Figs. 2.8 and 2.9, it is clear that angular dispersion is greatly reduced where a transfer lens is used to focus the incoming scattered electrons towards the beam separator centre. This is also why the primary beam is also pre-focused towards the beam separator centre, by doing this, spherical aberration is minimized [2.9].

Simulations predict that an energy range corresponding to a focal point spread of 20 mm around the beam separator centre (40% of the beam separator radius) will result in scattered electrons having a reduced angular spread at the detector plane. This is an important result, since most of the scattered electrons have energies well below the primary beam energy, they will be over-focused by the transfer lens. These simulation results also indicate that there is a relatively wide range of converging input angle conditions for which the output angular dispersion is relatively small, and therefore predicts that the beam separator spectrometer will have good focusing properties for parallel detection across the full range of emission energies.

2.2.6　Full range energy parallel acquisition design

Fig. 2.10 shows a simulation of scattered electron trajectory paths through the spectrometer after having been traced through the objective/transfer lenses. Here the beam separator is set to deflect a 10 keV primary beam through 90°. The simulation takes into account Auger electrons, as well as secondary and backscattered electrons.

Although only ray paths through the beam separator and post-deflectors are shown, they are actually traced from the specimen, which is biased at -5 kV, with a wide-variety of emission energies and angles. The transfer lens excitation is adjusted to minimize the angular dispersion for scattered electrons having energies from 1 to 2 keV. The shapes, retarding voltages, and magnetic excitations on the post-deflectors were designed so that the secondary, Auger and backscattered electrons are well separated and first-order focusing is achieved on their respective detector planes. The secondary electrons are mirrored back into the beam separator for a second pass.
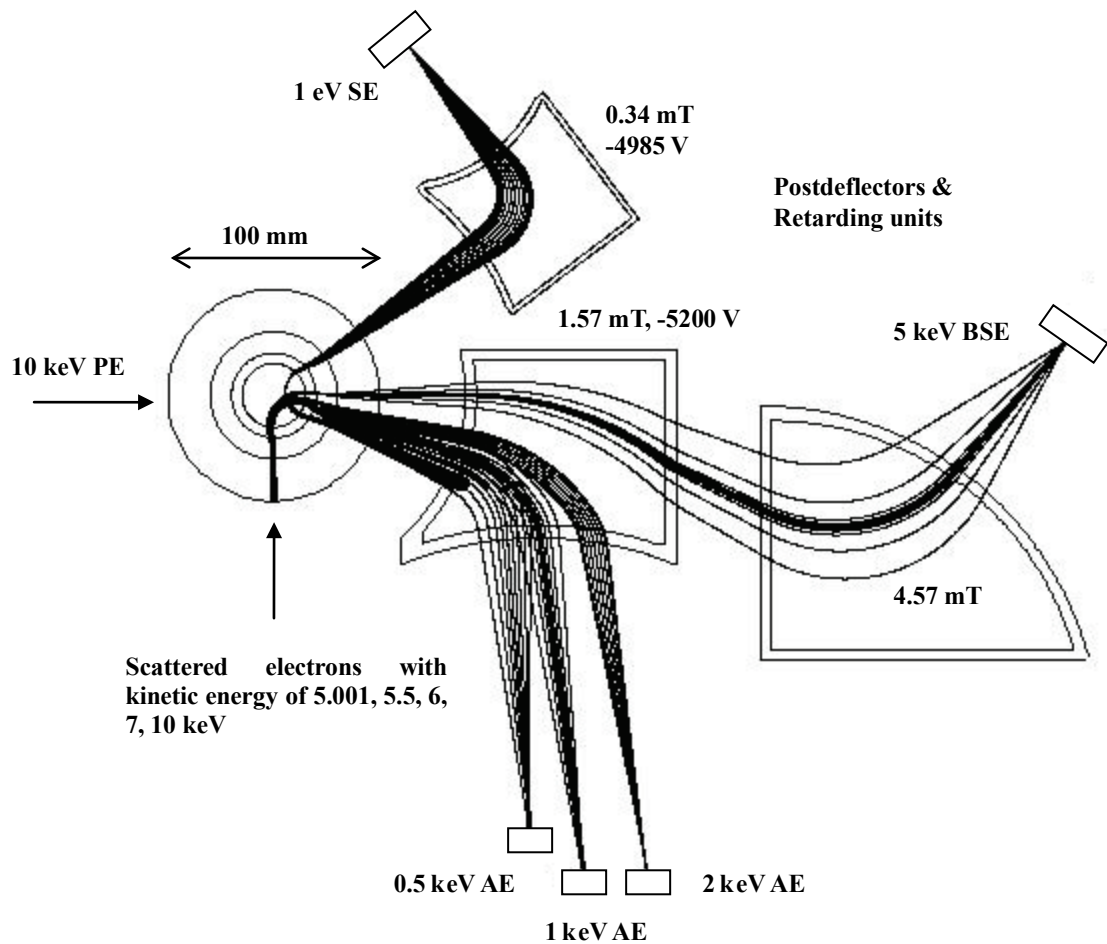
Fig. 2. 10. Simulated scattered electron trajectory paths in the spectrometer for 1 eV SEs, 0.5, 1, and 2 keV AEs, and 5 keV BSEs through the beam separator. The emission angles are plot in steps of 0.1 radians and range from 0 to 1.5 radians for SEs, 0 to 0.4 radians for AEs and 0.6 radians for BSEs.

Flat-plane detectors can be used for the secondary and backscattered electrons, however for the Auger electrons, due to their wide energy range; it is recommended that several detectors be used in parallel over smaller energy ranges. An example of using flat-plane detectors is shown in Fig. 2.10.

2.2.7 Energy resolution estimation

In order to estimate the energy resolution achievable for a given degree of angular dispersion on the scattered electrons, detailed diagrams of simulated ray paths around the detection plane were plot. Some examples of these diagrams are shown in Fig. 2.13. By examining the relative dispersion created by different emission energies and angles at the detector plane, an energy resolution estimate was made. A cosine distribution of the emission angle is assumed (relative to the optical axis), which, after taking into account the azimuthal direction, is proportional to sin2θ, giving the distribution peak to be 45° emission ($\pi/4$ radians). The average dispersion, Δx, was calculated by the following weighted average expression

$$\Delta x = \frac{\sum_{i=1}^{N} |x_i| \sin 2\theta_i}{\sum_{i=1}^{N} \sin 2\theta_i} \qquad (2.1)$$

Where, x_i is the position dispersion to the zero emission angle rays of the electrons with emission angle θ_i.

The energy resolution was then calculated by using the simulated dispersion along detection plane, like that shown for Auger electrons in Fig. 2.12. The overall behavior of the spectrometer does not necessarily follow simple dispersion rules where the energy resolution is proportional to the energy.

(a)

(b)
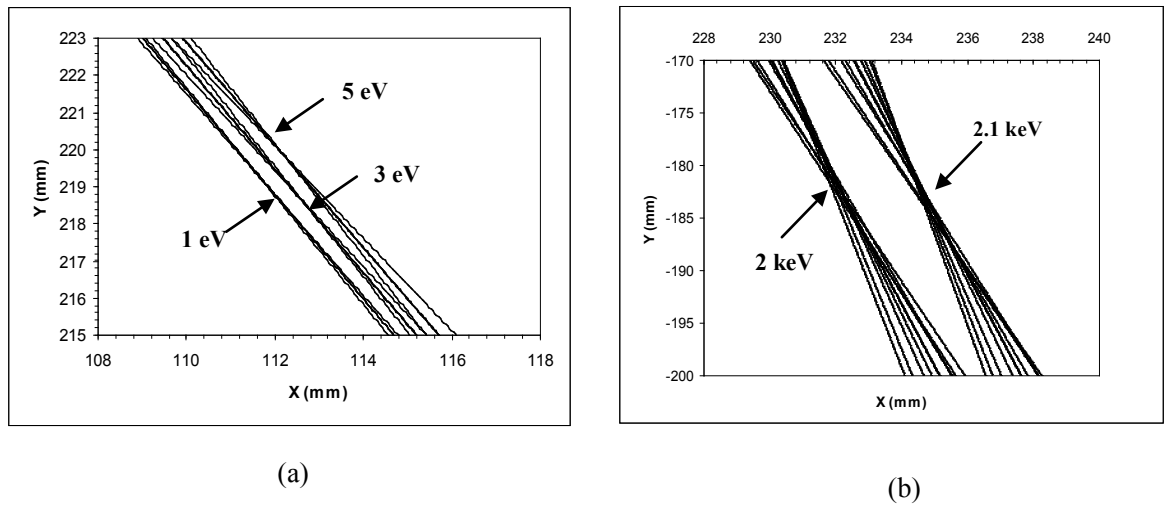
Fig. 2. 11. Simulated trajectory paths around the detection plane for different emission conditions: (a) 1, 3 and 5 eV SEs at 0, ± 0.8 radians; (b) 2 and 2.1 keV AEs at 0 to 0.4 radians in 0.1 radian steps.
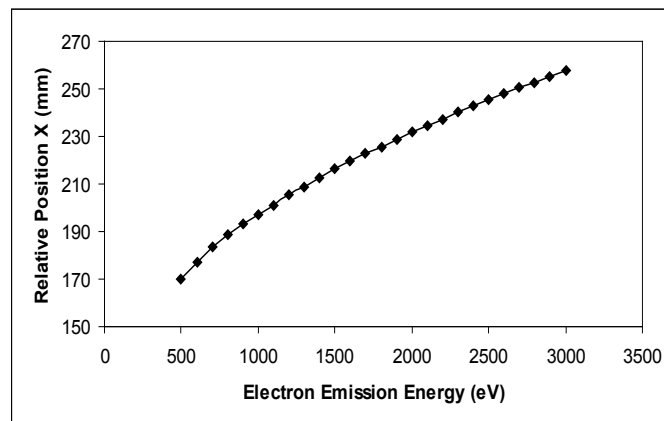
Fig. 2. 12. Simulated energy dispersion of Auger electrons.

The relative number of transmitted scattered electrons is proportional to 0.5 (1 − cos2θ_c), where θ_c is the cut-off angle as described in Chapter 1. The total transmission is estimated by averaging the respective transmissions for the in-plane and out-of-plane. The results are summarized in Table 2.1. They predict that the transmission of scattered electrons from the specimen to the detector plane for a given energy resolution will be relatively high. The transmission for 1 to 5 eV secondary electrons

having an energy resolution of 148 meV to 193 meV is predicted to be 100%. The transmission varies between 20 to 40% for 0.5 to 3 keV Auger electrons whose energy resolution is between 4 to 7 eV, and is approximately 50% in the case of 5 keV elastic backscattered electrons having an energy resolution of 42 eV. The relative energy resolution for the Auger and backscattered electrons for these conditions typically lies between 0.2 to 0.9%. It should be noted that the out-of-plane cut-off angles do not represent a fundamental limit to the spectrometer, since the beam separator size can always be scaled up to allow for 100% transmission in this direction, if this is done, the total transmission value is likely to exceed 50%.

Table. 2.1. Simulated energy resolution and transmission characteristics of the spectrometer at optimal focal plane.

Emission energy E (eV)	In-plane cut-off angle (radians)	Out-of-plane cut-off angle (radians)	Transmission (%)	ΔE (eV)	ΔE/E (%)
1 (SE)	$\pi/2$	$\pi/2$	100	0.148	14.8
3 (SE)	$\pi/2$	$\pi/2$	100	0.193	6.4
5 (SE)	$\pi/2$	$\pi/2$	100	0.175	3.5
500 (AE)	0.4	0.55	21.24	4.30	0.86
1000 (AE)	0.4	0.55	21.24	6.88	0.69
2000 (AE)	0.4	0.65	25.90	6.67	0.33
3000 (AE)	0.5	0.85	39.50	6.93	0.23
5000 (BSE)	0.6	0.95	49.02	41.93	0.83

2.2.8 Spectrometer performance comparison

The predicted performance summarized in Table 2.1 for the present beam separator spectrometer compares well with other types of electron energy spectrometers. It compares favorably for instance, with the well-known Cylindrical Mirror Analyzer (CMA) for Auger electrons operating at the second-order focusing condition, where the CMA mid-entrance angle is 42.3° [2.11]. Under this condition, the CMA for an

entrance angular width of $\pm$ 6° gives a relative theoretical energy resolution of around 0.328% and a transmission (over 2π sr) of around 20.6% transmission (neglecting scattering by its entrance/exit grids). However, a detailed comparison between the CMA and the present spectrometer is not meaningful, since the CMA does not provide a parallel energy spectrum. A better comparison would be with the parallel energy spectrometers proposed by Jacka et al [2.12-2.13], F. H. Read [2.14-2.15] or Kienle and Plies [2.2].

Both the HFA reported by Jacka and the PCMA reported by Read require relatively small entrance angular spreads, typically in the 1° to 3° range, and depending on the mid-entrance angle, their transmissions will be smaller than 5%. For the widest energy range reported by Read, 125 to 3000 eV and an energy resolution of around 0.4%, the relative transmission (over 2π sr) is around 2% (mid-entrance angle at 27.04^o). The widest energy range presented by Jacka is a few tens of eV to 2000 eV, the energy resolution of a few eV and the relative transmission is around 0.05% (mid-entrance angle at 20.76^o). The second-order versions of the spectrometers reported by Read and Jacka cannot be compared to the present spectrometer since the detectable energy range becomes considerably restricted. The spectrometer presented by Kienle and Plies is similar to the present beam separator spectrometer in that it can obtain good separation between secondary and backscattered electrons. However, it cannot obtain them at the same time and the secondary electron energy range is limited to 20 eV, therefore, a detailed comparison to the present beam separator spectrometer is also not meaningful. In the present context, it is sufficient to note that the present beam separator spectrometer is predicted to have a high transmission-energy resolution performance, comparable or better than the CMA operating at its optimum condition,

while at the same time being capable of capturing the entire range of scattered electrons in parallel.

2.3 An experimental magnetic beam separator spectrometer setup as a SEM attachment.

2.3.1 Experimental setup

The simulated magnetic beam separator spectrometer is predicted to capture electrons over the entire energy range in parallel. However, for small angular dispersion, large energy dispersion, as well as high transmission, the size of beam separator needs to be relative large, around 100 mm in diameter, as assumed for the simulation model used in the previous section. This involves using a SEM with a large vacuum chamber, especially custom built to incorporate it. In order to test the basic concepts behind the spectrometer proposal outlined in the previous section, a much smaller magnetic beam separator spectrometer was made, so that it could fit into a conventional SEM chamber as an add-on attachment. For the following feasibility studies, a JEOL 5600 SEM was used. Fig. 2.13 depicts the layout of the spectrometer attachment. Due to the limited size of the vacuum chamber, it is difficult to incorporate an array of post-deflector sectors together with the beam separator. Another possible solution to overcome this is to use electric retarding field grids/sectors, which can be designed with smaller dimensions and suitable shapes for integration into a smaller space.

Fig. 2.13 also depicts predicted electron trajectory paths inside the add-on spectrometer SEM attachment. The electron primary beam is supplied from a SEM column (not shown) and bent 90° by the magnetic sector beam separator towards the mixed magnetic and retarding electric field objective lens, and focused onto the specimen, which is biased at a certain negative voltage V_S. The scattered electrons

travel back into the beam separator, which acts as the first stage of an energy spectrometer. The retarding sector mirror, which is biased at V_M, is used to mirror back the secondary electrons into the beam separator for a second pass. Secondary electrons then hit a scintillator placed before a (photomultiplier tube) PMT, to generate light, which is then detected by the PMT and amplified and converted into current. The PMT current is measured by a Keitley 617 electrometer and monitored by a PC. The integrated spectrum of secondary electrons can then be obtained as the collected current of the PMT by ramping the retarding voltage V_M of the retarding sector mirror as illustrated in Fig. 2.14. Backscattered electrons travel through the first retarding unit and, in principle, can be separately detected by another detector. For simplicity, the present setup does not use a transfer lens to focus scattered electrons into the beam separator, which was proposed in chapter 2. The lack of transfer lens may cause lower collection efficiency and more angular dispersion of scattered electrons.
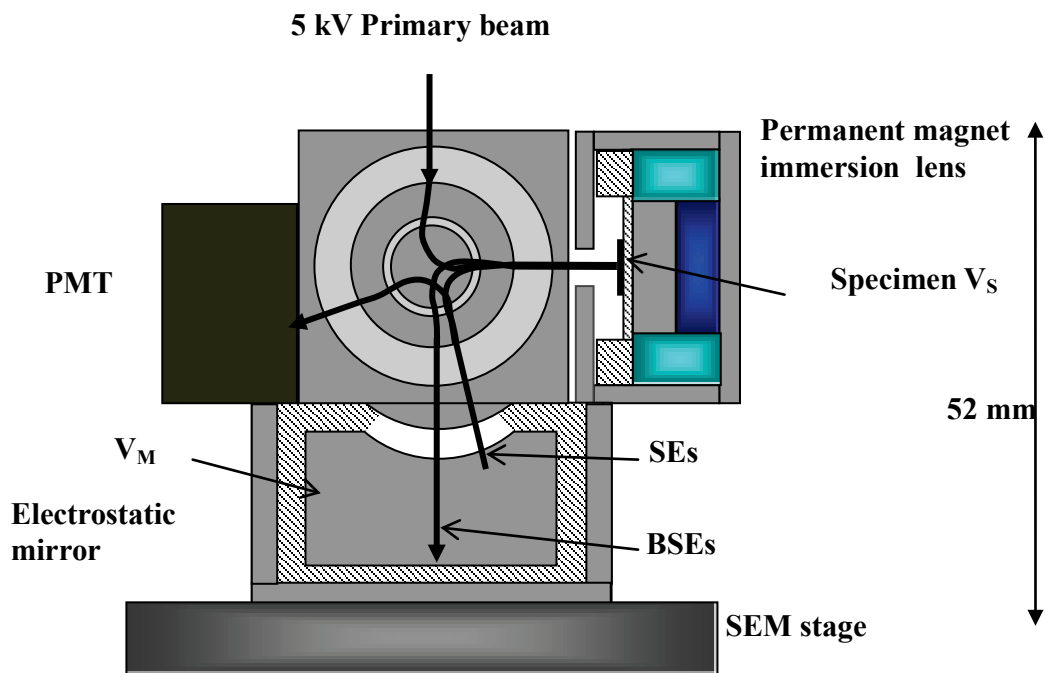
Fig. 2. 13. The magnetic beam separator spectrometer setup as a SEM attachment.
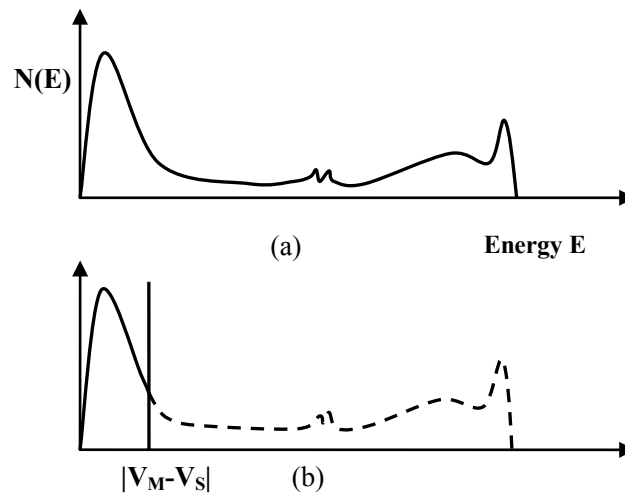
Fig. 2. 14. Electron energy spectrum: (a) Typical scattered electron energy spectrum; (b) Ramping voltage of the mirror V_M

A schematic of the magnetic beam separator is shown in Fig. 2.15a, while a photo of the manufactured unit is presented in Fig. 2.15b. Its outer casing dimensions are 30 mm x 30 mm x 78 mm. The inner sector plate has a diameter of 10 mm, the outer sector ring has an inner diameter of 12 mm and an outer diameter of 20 mm. The sectors are fitted into a mild-steel rectangular block casing with a bore diameter of 26 mm. In between the inner and outer sectors and in between the outer sector and the casing are non-magnetic alignment pieces made of brass. The transverse magnetic gap is kept at 2 mm. A copper wire with a diameter of 0.5 mm was used to wind 150 turns on the inner solenoid coils and 50 turns on the outer solenoid coils.
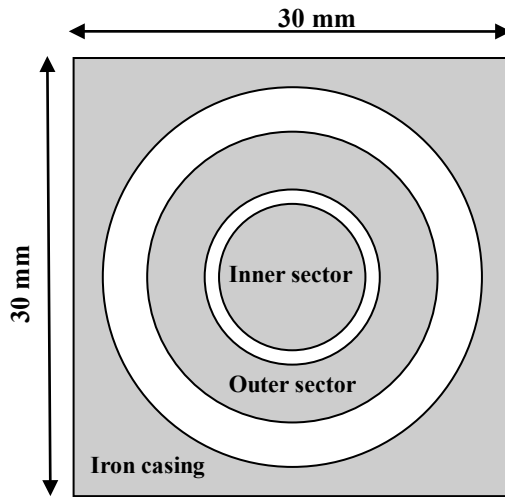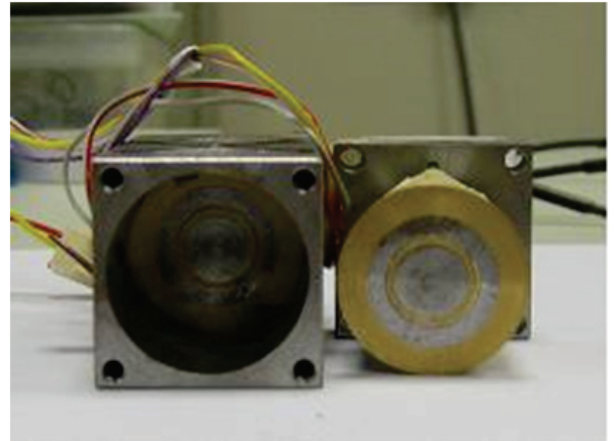
Fig. 2. 15. A circular magnetic sector deflector: (a) drawing of the side view; (b) a photo of the attachment design

The overall diameter of the immersion lens casing is 30 mm (the inner diameter is 26 mm). A NeFeB permanent magnet disc (9000 AT/cm) is used for the magnetic excitation having a diameter of 15 mm and the height of 5 mm, and provides a magnetic excitation of 4500 AT. Copper wire with a diameter of 0.4 mm was used to wind 230 turns on an iron core (diameter 15mm and height of 5 mm) placed onto the top of the permanent magnet for fine focusing control, as shown in Fig. 2.16a. However, during the experiments, it was realized that the copper coil generated heat, which caused a reduction in the permanent magnet strength, this prevented the possibility of fine focusing, which in turn meant high resolution images could not be acquired. The lens pieces are held together and held to the separator by magnetic force.
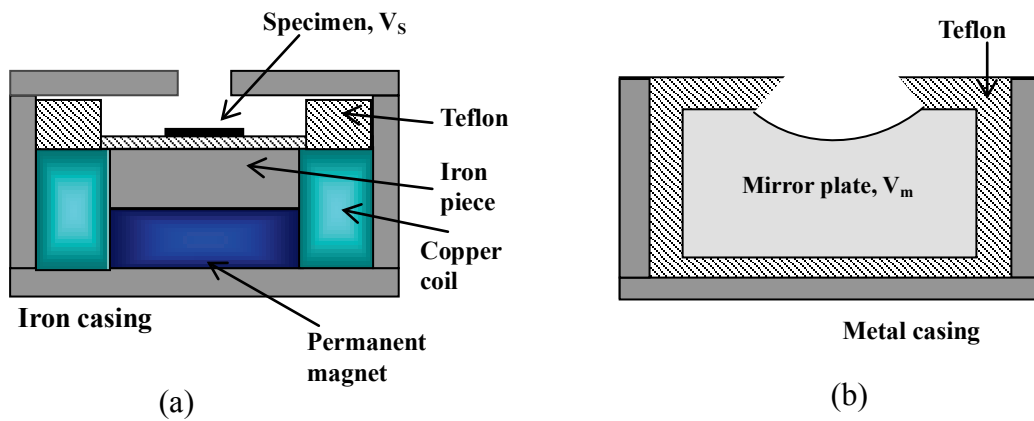
Fig. 2. 16. (a) Add-on mixed-field immersion lens; (b) Electric retarding field mirror

The electric retarding field mirror is simply designed using two copper plates placed in parallel with a 3 mm gap between them. The copper plates have a circular curved shape with the same center as the sectors of the beam separator, as illustrated in Fig. 2.16b, to ensure that the scattered electrons escape the separator perpendicular to the mirror electric field.
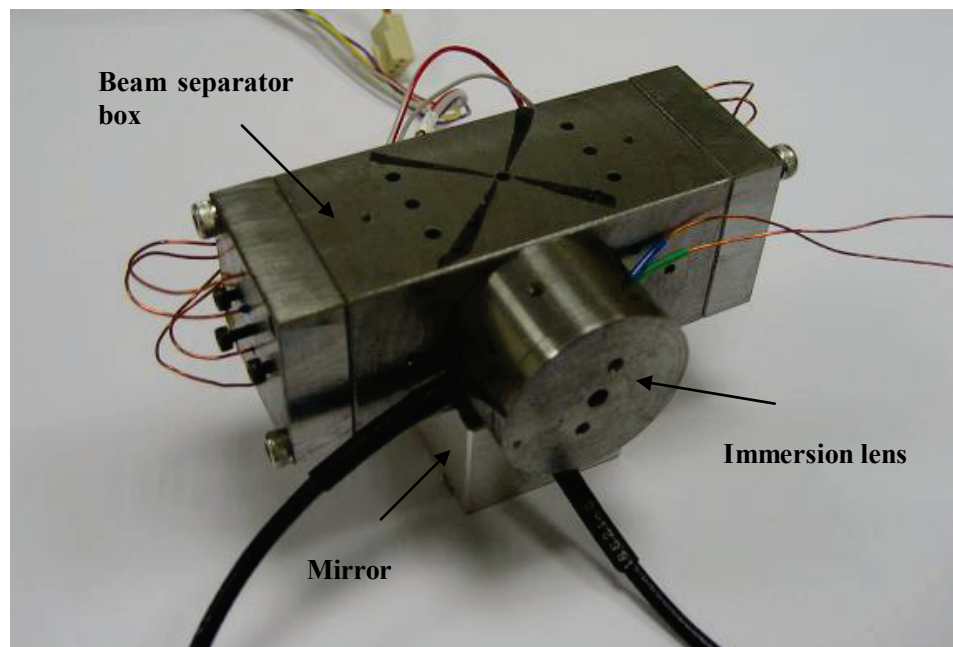
Fig. 2. 17. A photo of the assembled spectrometer attachment

Fig. 2.17 shows the assembled spectrometer attachment. With a total height of 52 mm, it can be used in a normal SEM (JEOL 5600 in this case)

2.3.2 Preliminary experimental results

Fig. 2.18 shows the secondary electron image of a copper grid specimen on carbon with a periodicity of 15 μm. The image is formed from scattered secondary electrons that travel through the objective lens and beam separator before being mirrored back and deflected out of the beam separator. The electrons then hit a copper plate in order to generate slow secondary electrons that can be detected by the SEM's own SE detector. In this way, it is relatively straight forward to form an image. The backscattered electrons pass through the retarding sector mirror due to their high kinetic energies and are absorbed by a carbon block placed at the back of the mirror. In the present setup, it is not possible to capture high resolution images due to the lack of a fine focusing mechanism.

30 μm
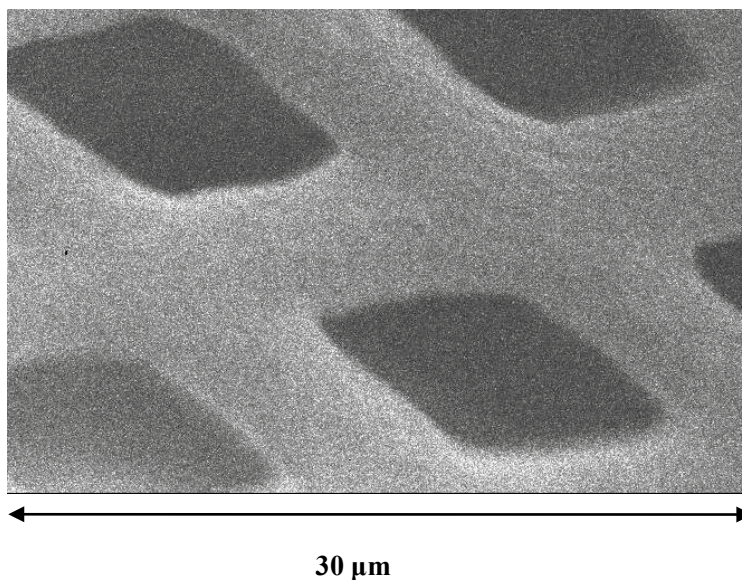
Fig. 2. 18. An SE image of a copper grid specimen on carbon, with a periodicity of 15 μm

The excitations of the beam separator and the specimen biasing voltage were obtained by imaging the copper grid specimen, which involved stigmatic focusing of the beam separator and setting the objective lens focus onto the specimen. The excitations of the beam separator to do this were 70.5 AT for the inner sector and -9 AT for the outer sector. The specimen was biased at V_s = -3650 V and 5 keV primary beam energy was used.

Fig. 2.19 shows the collected PMT current as a function of mirror voltages for different specimen biasing voltages V_S. The specimen voltage, V_S, is changed in one volt steps. For each value of V_S, the PMT signal is curved fitted, normalized, and then differentiated with the help of software to obtain the SE spectrum. The results are given in Fig. 2.20. The SE spectrum linearly shifts as a function of specimen voltage, as expected. These preliminary results serve to demonstrate that spectral information of the scattered electron spectrum can be obtained through the use of a magnetic beam separator spectrometer.
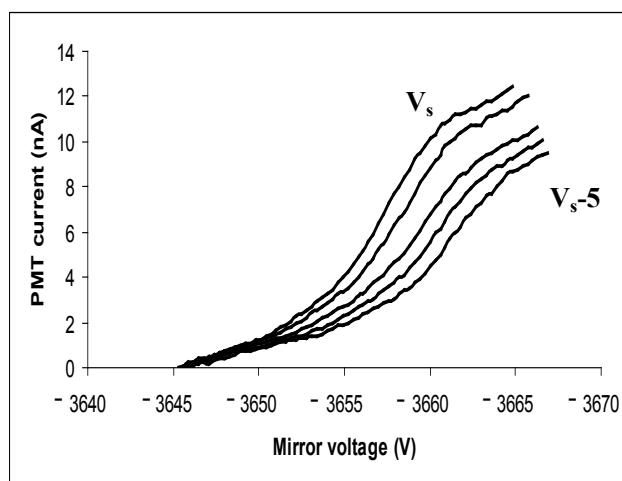
Fig. 2. 19. Experimental collected PMT currents as a function of the specimen voltage varying in one volt steps
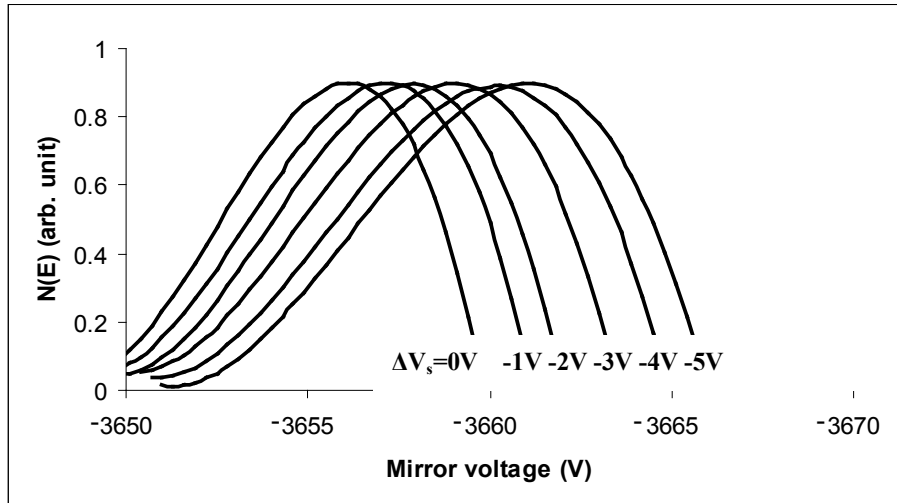
Fig. 2. 20. Secondary electron spectra obtained by curve fitting, normalizing and differentiation of experiment data. The influence of changing the specimen bias is clearly shown

For each spectrum, most of the electrons having energy larger than 9 eV were lost. This effect can be explained by loss of transmission in the out-of-plane direction, due to the relative small size of spectrometer attachment (plate separation of 2mm). Simulations of this experimental setup were carried out for scattered secondary electrons to confirm this effect, and predict that the setup accepts all the 1 eV secondary electrons with the emission angles larger than 1 rad in the out-of-plane direction. The 10 eV secondary electrons can only pass through the setup in the out-of-plane direction if the emission angles are smaller than 0.1 rad. The simulation results predict that most of the high energy secondary electrons (>9eV) are lost in the out-of-plane. This explains why the experimental secondary electron spectra drop sharply in the high energy region.

2.4   Conclusions

A circular magnetic beam separator spectrometer has been investigated by direct ray tracing simulations. The design is based upon the use of a magnetic sector deflector as

a beam separator, which bends the primary beam 90°. The primary beam then enters a mixed field electric/magnetic immersion lens. The scattered electrons travel back through a transfer lens and into the beam separator, which acts as the first stage of an energy spectrometer. An aperture is placed at the entrance of the beam separator in order to restrict the angular dispersion of the transmitted scattered electrons in the plane of deflection. A series of retarding field magnetic sector post-deflectors are then used to focus the scattered electrons on to multi-channel detectors.

By using the transfer lens to focus the scattered electrons into the centre of the beam separator, the effect of angular dispersion at the detector plane is predicted to be significantly reduced. The transfer lens does not significantly degrade the primary beam optics, and small adjustments in the objective lens excitation can be used to refocus the primary beam on to the specimen if changes in the transfer lens excitation are made in order to optimize scattered electron collection at the detection plane.

It is predicted that the spectrometer can acquire the entire energy range of scattered electrons, including secondary, Auger and backscattered emissions with high transmission (around 30% for Auger range and up to 100% for the secondary electron range). The energy resolution is simulated to be comparable to that of the CMA for the Auger and backscattered electron ranges (less than 0.5%) and to be acceptable for the secondary electron range.

A preliminary proof-of-concept experiment was carried out using a small add-on beam separator spectrometer attachment inside the specimen chamber of a conventional SEM. Initial experimental results of secondary electron spectra acquired

from the prototype were obtained, confirming that a circular beam separator can function as an energy spectrometer for scattered electrons in the SEM. However, these results also demonstrate that the beam separator spectrometer concept requires a custom built SEM, which has an enlarged SEM specimen chamber, in order to reduce out-of-plane scattering.

References

2.1 A. Khursheed, N. Karuppiah, " A high resolution mixed field immersion lens attachement for conventional scanning electron microscopes", Rev. Sci. Instrum. 73 (2002) 2906.

2.2 M. Kienle and E. Plies," An off-axis multi-channel analyzer for secondary electrons", Nucl. Instrum. And Method. in Res. A **519**, (2004) 325

2.3 M. Mankos, "Scanning electron microscope with curved axes", US patent 7,205,542 B1 (2006).

2.4 M. Mankos, "Prism array for electron beam inspection and defect review" US patent 6,878,937 B1 (2005).

2.5 A. Khursheed, and M. Osterberg, " A spectroscopic scanning electron microscope design", Scanning 26 (2004) 296.

2.6 A. Khursheed, and M. Osterberg, "Developments in the design of a spectroscopic scanning electron microscope", Nucl. Instrum. Meth. A 556 (2006) 437.

2.7 M. Osterberg, and A. Khursheed, "Simulation of magnetic sector deflector aberration properties for low energy electron microscopy", Nucl. Instrum. Meth. A 555 (2005) 20.

2.8 M. Osterberg, "Magnetic sector deflector aberration properties for low energy scanning electron microscopy", PhD thesis, National University of Singapore (2006).

2.9 A. Khursheed, "KEOS", Electrical and Computer Engineering Department, National University of Singapore, Singapore.

2.10 A. Khursheed, "The finite element method in charged particle optics", Kluwer Academic Publishers, Boston (1999).

2.11 H. Hafner, J. A. Simpson, and C. E. Kuyatt, Rev. Sci. Instrum., **39,** No. 1, 33-5 (1968).

2.12 M. Jacka, and M. Kirk, M. M. El Gomati and M. Prutton, " A fast parallel acquisition electron energy analyzer: The hyperbolic field analyzer", Rev. Sci. Instrum. **70** (1999) 2282

2.13 M. Jacka, A. Kale and N. Traitler, "Hyperbolic field electron analyzer with second order focussing", Rev. Sci. Instrum*.,* **74** (2003) 4298

2.14 F. H. Read, "The parallel cylindrical mirror electron energy analyzer", Rev. Sci. Instrum. **73** (2002) 1129

2.15 F. H. Read, D. Cubric, S. Kumashiro and A. Walker, "The parallel cylindrical mirror analyzer axis-to axis configuration" Nucl. Instrum. and Meth. in Phys. Res. A **519** (2004) 338

Chapter 3: A second-order focusing toroidal spectrometer

3.1   Introduction

In the previous chapter, a circular magnetic beam separator spectrometer for in-lens SEMs was proposed. In general, incorporation of an energy spectrometer into such SEMs requires redesign of the SEM column, this is because the energy spectrometer is both in the path of the primary beam and scattered electrons. The energy spectrometer cannot, therefore, function as an add-on attachment. In conventional SEMs, the specimen is placed in a free-field region below the final pole-piece of the objective lens and it is possible to place the spectrometer off-axis, where it acts on scattered electrons well away from the path of the primary beam. This provides the possibility of using an energy spectrometer as an add-on attachment. Both this chapter, and the following one, present add-on energy spectrometer designs for conventional SEMs.

Rau and Robinson proposed a SEM electrostatic toroidal deflection spectrometer attachment for microtomography and electron spectroscopy analysis [3.1, 3.2]. This design has a 65$^\mathrm{o}$ deflection angle, ϕ, in the polar direction and fully 2π transmittance in the azimuthal direction, as shown in Fig. 3.1. The spectrometer is placed in between the final pole-piece of the objective lens and the specimen. Scattered electrons enter the spectrometer at the input angle, θ, of 25$^\mathrm{o}$ with an angular spread of ±3$^\mathrm{o}$, and are deflected through a 65$^\mathrm{o}$ angle. The energy resolution of this initial spectrometer design was simulated to be 0.7% (haft-width) [3.3]
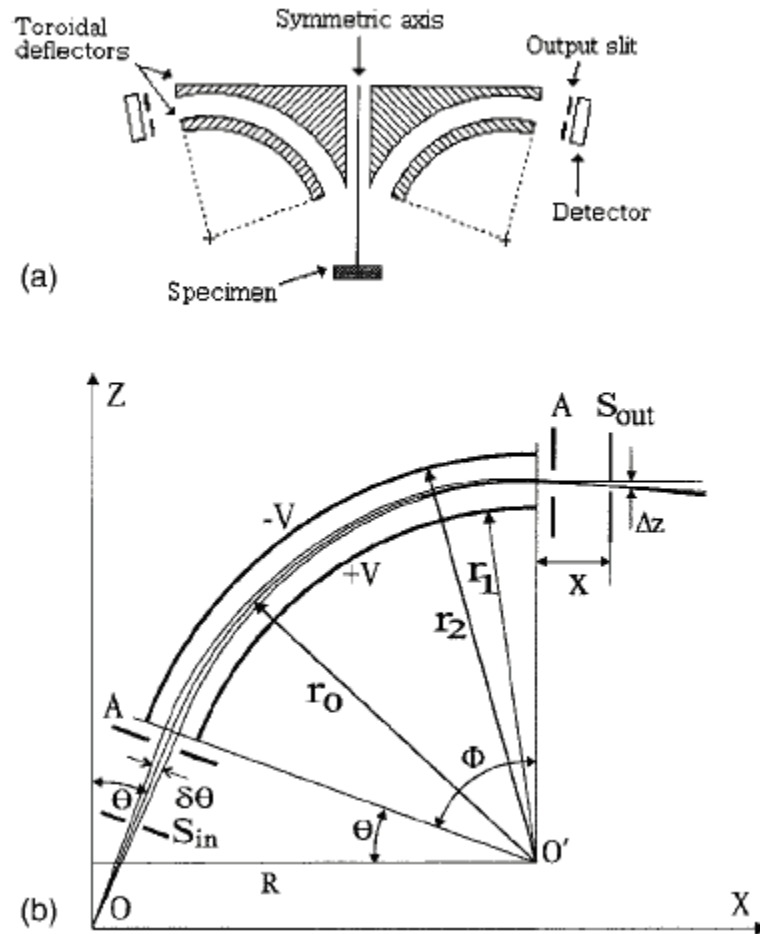
Fig. 3. 1. Schematic diagram layout of a first-order focusing toroidal spectrometer reported by Rau and Robinson: (a) Cross-section showing specimen and detector; (b) Simulation layout, OZ is the rotational axis of symmetry [3.1].

The spectrometer design was later improved, in which a deflection angle of 59° was used instead of 65°. This second spectrometer design was simulated to have an energy resolution of 0.25% (haft-width) for an angular spread of $\pm3^{o}$, corresponding to a base resolution of around $2\Delta\theta^2$ (0.5% for $\pm3^{o}$) [3.3] . It was used for providing depth information of multi-layer thin films by monitoring BSE energy spectra inside the SEM. The same spectrometer design was also recently used for monitoring specimen charging, where specimen surfaces charge to -5 kV [3.4]. The Rau and Robinson toroidal spectrometer, however, does not provide multi-channel energy spectral information, since the detector must lie on a cylindrical wall shaped surface. In

63

addition, these spectrometers still have first-order focusing properties that limit the energy resolution at high transmittance.

Toroidal shaped spectrometers have been used in many applications, both for energy and angular electron spectroscopies, due to their wide collection angle in the azimuthal direction (up to 2π) as well as their ability to provide limited parallel detection (like the hemispherical deflection analyzers described in Chapter 1). Examples of these spectrometer designs include a first toroidal shaped electrostatic spectrometer for momentum determination [3.5]; a multichannel toroidal spectrometer for angular and momentum measurements [3.6-3.7]; for gas phase studies electron impact ionization measurements [3.8-3.10]; for photoelectron applications [3.11]; or a design for general energy and angle resolved applications, namely TEARES [3.12-3.13].

So far, all of the previously reported toroidal spectrometer designs, including the Rau and Robinson spectrometer designs for the SEM, have first-order optics, which makes their attainable energy resolution (for a given entrance angular spread) inferior to other types of 2π radian collection spectrometers such as the Cylindrical Mirror Analyzer (CMA), commonly used in Scanning Auger Microscopy (SAM) [3.14].

At its second-order focusing condition (only possible at an entry angle of 42.3º), the CMA energy resolution has a cubic dependence on input angular spread, approximately 1.38 $\Delta\theta^3$ for acceptance angles between ± 6º [3.14], indicating that its energy resolution is limited by 3rd order spherical aberration. This gives an average theoretical relative energy resolution ($100 \times \Delta E/E$) of around 0.155%. Assuming a

cosine emission distribution with respect to the polar angle θ (measure relative to the z-axis) and 2π radian emission in the azimuthal angular direction, the total theoretical transmission is proportional to $\sin(2\theta)$, around 20% for $\pm$ 6º. In practice, grids are used at the spectrometer entrance and exit which typically lower the transmission to around 14%. In contrast, toroidal spectrometers (non-retarded) have a theoretical energy resolution of around 0.25% at $\pm$ 3º acceptance angles (around 10% transmission). This value was predicted by simulation for both a toroidal spectrometer in photoemission applications [3.11], and the Rau and Robinson toroidal backscattered electron spectrometer for the SEM [3.1-3.2]. The energy resolution of 0.25% at $\pm$ 3º acceptance angles is also comparable to the one usually quoted for the Concentric Hemispherical Analyser (CHA) on its Gaussian focal plane [3.15], given by $\Delta\theta^2$, where $\Delta\theta$ is the angular spread.

Higher energy resolution spectrometers for the SEM are needed if applications such as Auger electron spectroscopy is to be carried out. Therefore, designing a new spectrometer based on the toroidal shape one that has high energy resolution, high transmittance, and can be incorporated into the SEM chamber as an attachment is the motivation of this chapter.

The spectrometer presented in this chapter, is a new toroidal spectrometer, which is designed to capture electrons in the full 2π azimuthal angular direction while at the same time having second-order focusing optics. The design is based upon the spherical aberration cancellation idea reported by Khursheed [3.16], in which the spherical aberration is cancelled by obtaining an intermediate focus in the r-z plane. This allows for second-order spherical aberration contributions accumulated before

and after the intermediate focus to cancel, since electrons with emission angles to either side of the central ray gain spherical aberration are of opposite sign. The remaining spherical aberration is therefore of third-order.

3.2   Simulation design of a second-order focusing toroidal spectrometer

3.2.1   Simulation design

The design approach taken in the following section is essentially a simulation one, where two software programs were used to verify the results. The first software is part of the KEOS package [3.17]. Finite element programs were used to solve for two-dimensional rotationally symmetric electrostatic field distributions on a polar mesh. Numerical ray tracing of electrons through these field distributions were then plot using bi-cubic interpolation and the 4th-order Runge-Kutta method. The meshes were graded so that smaller mesh cells are used within the centre region between the deflection plates: the size of each adjoining mesh cell increases by 10% in the radial direction, and mesh cells mid-way between the plates are typically 276 smaller than those at electrode boundaries. The base mesh resolution for each field solution uses 145 by 145 mesh lines. The accuracy of the simulation was continually checked by repeating all results with finer numerical meshes and smaller trajectory step sizes, ensuring that the final simulated parameters such as rms trace width did not change significantly (by less than 1 %).

The second software is a commercial one called Lorentz-2EM [3.18], a hybrid software that combines boundary element and finite element techniques. The boundary element method avoids well-known mesh generation/interpolation problems

of the finite element method [3.19], especially difficult for curved boundaries. The finite element method is used for non-linear field solutions, such as those that arise in the presence of magnetic saturation, problems that are difficult to solve directly by boundary element methods. Both numerical techniques are coupled together, utilizing their relative strengths. In addition, an adaptive segment technique varies the density of charge segments on conductor surfaces, refining it according to local field strength. The subsequent improvement on field accuracy and shortening of trajectory run times for a given number of charge segments, allows for greater complexity of problems to be modeled. The software is able for instance, to simulate electrostatic structures that are very small, embedded in much larger conductor layouts. In the present context, this feature was used to plot accurate direct trajectory paths through an aperture slit, microns in size, placed within the fringe fields of a spectrometer measuring many centimeters. The use of a 5th order Runge-Kutta method in which the trajectory step-size varies according to local truncation error also helped in making this kind of problem much easier to simulate. It also has the advantage of having a friendly interface with CAD tools that allows for designing complex boundaries, so that the simulation model can be more realistic, closer to the final engineering design. The results generated from these two programs were compared to each other and showed good agreement with a mismatch of less than 1%. This agreement between both KEOS and Lorentz-2EM indicates that the following spectrometer design results are reliable.
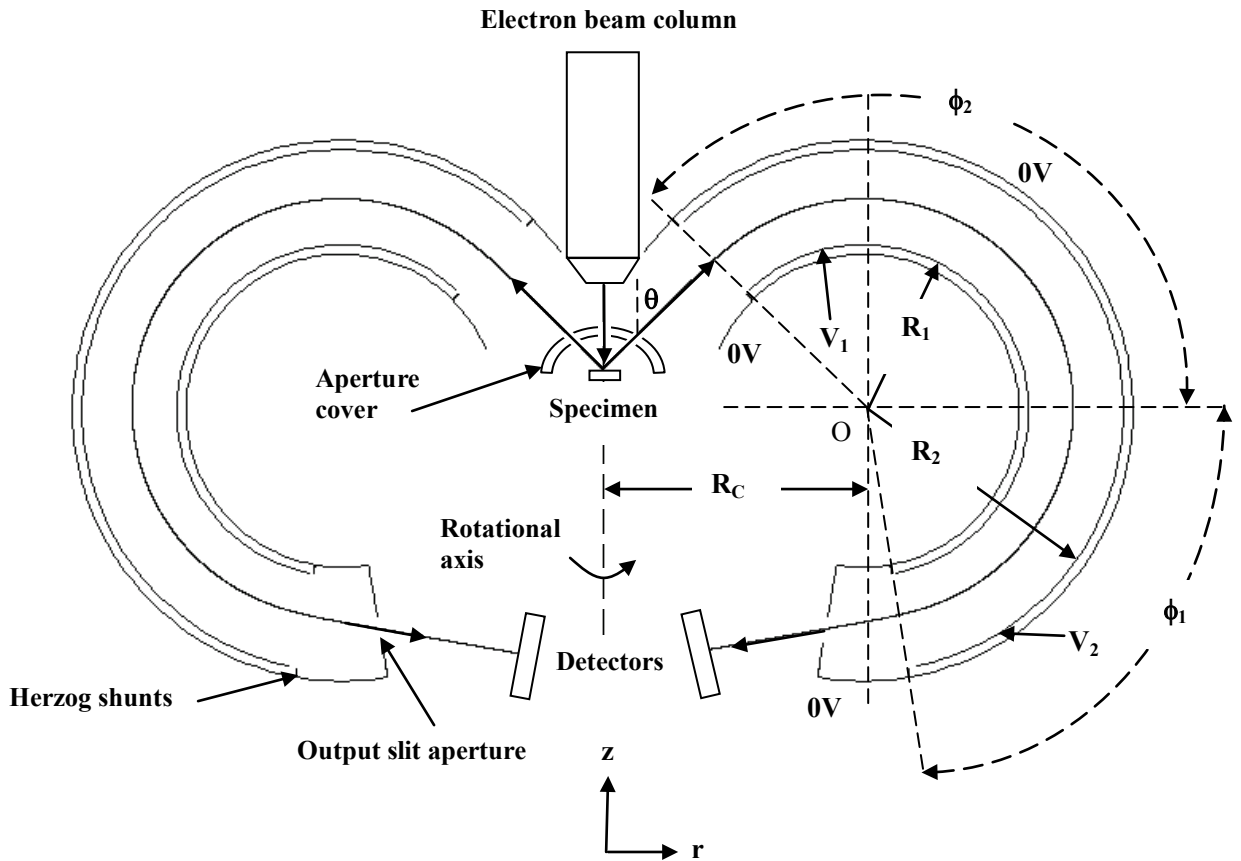
Fig. 3. 2. Overall schematic layout of 2π radian collection second-order focusing Toroidal spectrometer design.

Fig. 3.2 shows a cross-sectional schematic of the kind of toroidal spectrometer designs considered in this chapter. An illuminating beam, of either photons or electrons is directed and focused on to the specimen through a hole in a hemispherical aperture cover. The subsequent scattered/secondary electrons travel from the specimen through a ring slit in the aperture cover, entering the spectrometer at an angle θ with respect to the vertical axis. The width of the annular slit defines the input angular spread, $\pm\varDelta\theta$. The polar coordinates ϕ_1, ϕ_2, R_1 and R_2 define the length and radii of the spectrometer deflection plates around the centre point O in the r-z plane, while V_1 and V_2 represent the voltages to which they are biased (+1 and -1 for the purposes of this simulation). The distance of the point O to the rotational axis is

denoted by R_C, and the instrument is surrounded by zero volt shielding plates, where normal Herzog shunt plates smoothly attenuate fringe fields. Electrons that pass through the spectrometer, can either be filtered by an output annular slit aperture before being collected by a 2π collection detector (or an array of detectors distributed in the azimthual direction), or they can pass through a zero volt grid and strike an array of multi-channel plate detectors for energy parallel acquisition, where the detection plane is defined on a shallow cone surface.

Table 2.1. Design parameters of the spectrometer.

Input angle (rad)	θ	$\pi/4$ (45°)
Angular Length (rad)	ϕ_1	$-\pi/2.25$
	ϕ_2	$3\pi/4$
Radii (cm)	R_1	1.4
	R_2	2.2

Many designs were investigated by varying the angular length (ϕ_1, ϕ_2) and the input angle, θ of the spectrometer to optimize the energy resolution. The highest energy resolution was achieved for the design parameters shown in table 2.1. Fig. 3.3 depicts 16 equipotential lines between -1 to +1 V in equal steps for this spectrometer design. These radii are nominal, since all important optical/aberration parameters, including the pass energy, scale linearly with spectrometer dimensions. Fig. 3.3 shows that although fringe fields generated from the deflection plates penetrate into the entrance and exit regions of the spectrometer, they are greatly attenuated by the Herzog shunts. With this electrode arrangement, variations in the precise shape of the shielding plates beyond the Herzog shunts do not greatly affect the focal properties of the spectrometer.
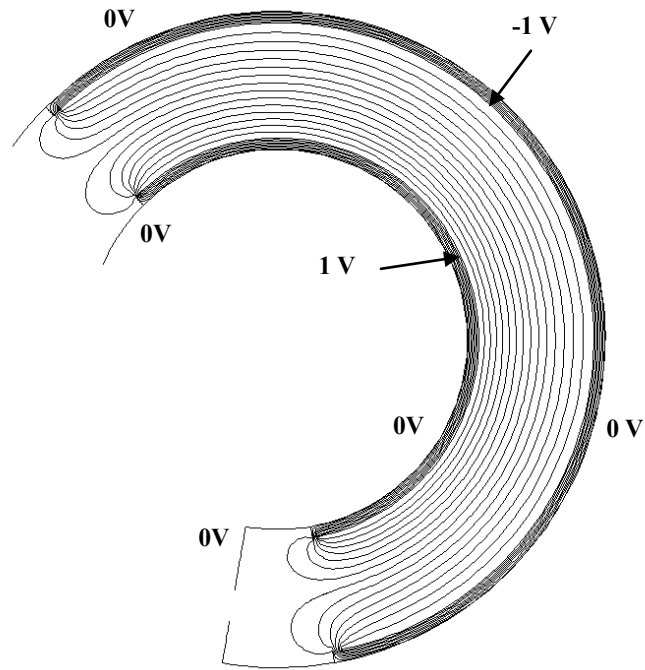
Fig. 3. 3. Equipotential lines from a numerically solved field distribution for the spectrometer. 16 equal potential intervals are taken between -1 V to +1 V.

Electron trajectory paths are traced from the specimen into the spectrometer, starting with the central ray whose energy is automatically scaled so that its trajectory path is always normal to the deflection plates on exit. This condition means that the central trajectory does not necessarily exit mid-way between the deflection plates, and indeed, there is no need to enforce it to do so. For the deflection plate potentials normalized to -1 V and +1 V, the pass energy for the toroidal spectrometer shown in Figs. 3.2 and 3.3 was found to be 2.293 eV.

Fig. 3.4a shows trajectory paths of scattered electrons leaving a point on the rotational axis with the pass energy 2.293 eV for an entrance angle of 45º and an input angular spread of ±6º, 21 trajectories are plot in uniform angular steps. These ray paths clearly indicate a much sharper focus at the exit of the spectrometer than for the intermediate focus and this suggests that second-order focusing is taking place at the

spectrometer exit. Fig. 3.4b shows that the spectrometer plate geometry can in principle accept an input angular spread of up to $\pm10^{\circ}$, corresponding to a transmission of around 34% for a cosine distribution of emission.

PE

First-order focus

$\phi_2 = 3\pi/4$ rad

Specimen

(a)

$\phi_1 = -\pi/2.25$

Second-order focus

(b)
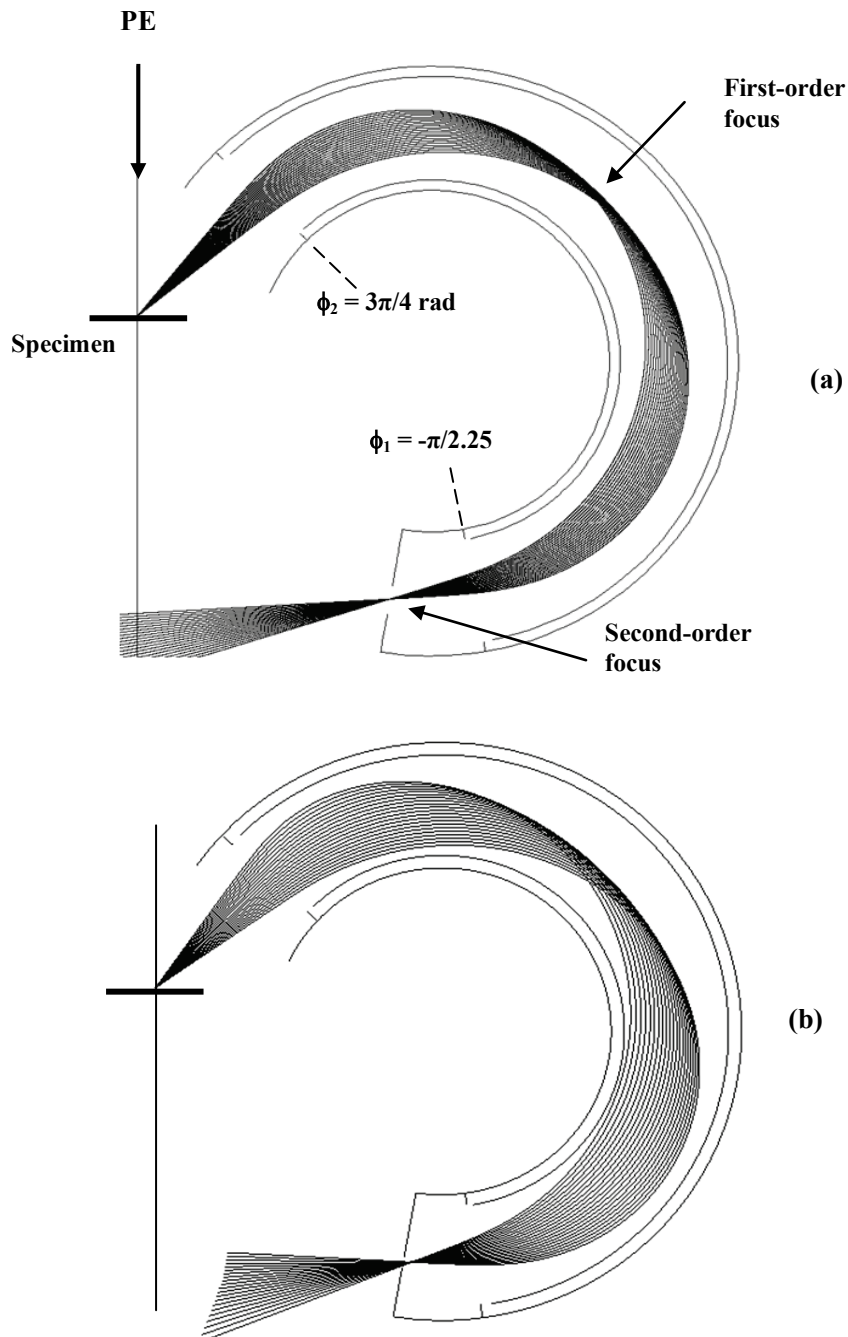
Fig. 3. 4. Simulated ray paths of electrons through the spectrometer at the pass energy for a wide variety of entrance angles. The central ray enters in at 45° and 21 trajectories are plot over uniform steps for an input angular spread varying from: (a) -104 mrad to +104 mrad (-6° to 6°); (b)-173 mrad to +173 mrad (-10° to 10°).

3.2.2 Energy resolution

By monitoring intersection points and angles with the central ray, it is relatively straightforward to plot the beam trace width as a function of input angle at the output Gaussian focal plane, which is shown in Fig. 3.5a. This graph shows that second-order focusing is predicted for the spectrometer since the trace width at the Gaussian plane clearly exhibits third-order (cubic) spherical aberration dependence with respect to the input angular spread. Fig 3.5b depicts the dependence of the trace width at the output Gaussian focal plane caused by the relative energy spread in the beam, and as expected, it takes a first-order linear variation (dispersion).

The trace width at the output focal plane, ΔTR, is then a combination of energy dispersion and spherical aberration, and can be approximately represented by fitting a cubic expression to Fig. 4a and a straight line to Fig. 4b, which is given by

$$\Delta TR = 0.553 R_1 \left(\frac{\Delta E}{E} \right) + 1.925 R_1 \Delta \theta^3$$

(3.1)

Proceeding with the normal method of estimating energy resolution, which assumes that the minimum energy resolution is equivalent to half the spherical aberration contribution distributed over the full input angular variation [$-\Delta\theta$, $+\Delta\theta$], the first term in the above equation is equated to the second term, obtaining,

$$0.553 R_1 \left(\frac{\Delta E}{E} \right) = 1.925 R_1 \Delta \theta^3$$

(3.2)

$$\Rightarrow \left(\frac{\Delta E}{E} \right) = 3.48 \theta^3$$

(3.3)

At say 104 mrad (6º), the relative base energy resolution is predicted to be 0.392%, or 0.049% at 52 mrad (3º).
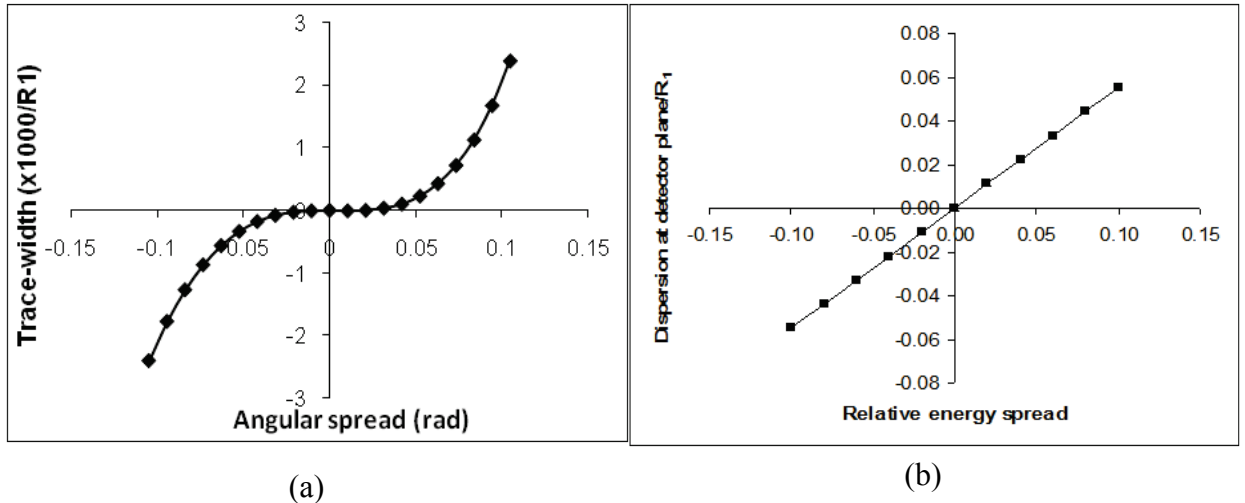
Fig. 3. 5. Simulated normalized trace width at the output plane: (a) due to spherical aberration; (b) due to relative energy spread

A more accurate method of calculating the relative energy resolution is simply to estimate it to be twice the value of the rms value of the graph depicted in Fig. 3.5a, which is 2.054×10^{-3}, and divide it by the gradient of the line shown in Fig. 3.5b, 0.554, to obtain an estimated theoretical relative base energy resolution of 0.37%. The rms approach is more general and has the advantage of not depending on the precise form of spherical aberration distribution, which will inevitably contain within it, higher order terms, and residual traces of the second-order term. The rms approach is also better suited to investigate the improvement in energy resolution that can be obtained by shifting the output slit plane slightly away from Gaussian focal point along the central ray. It was noticed for instance that shifting the output slit plane to -0.17 mm before the Gaussian focal plane resulted in the energy resolution improving by a factor of 2.53, to 0.146%. This is a well known property of third-order aberration limited focusing systems, and a similar factor of improvement has been incorporated into the best theoretical energy resolution estimate already cited for the CMA. The simulated energy resolution for the present second-order focusing toroidal

spectrometer is therefore comparable to the theoretically best energy resolution of the CMA [3.14].

For input angles of ±3º, the relative energy resolution based upon calculating the spherical aberration distribution rms value was found to be 0.0446% at the Gaussian focal plane, which at a distance of -0.04 mm along the central ray falls to 0.0188% (factor of 2.36 improvement), over an order of magnitude better than the 0.25% simulated energy resolution reported for previous first-order toroidal spectrometers. Based upon the foregoing simulated energy resolution estimates of 0.146% and 0.0188% at input angular spreads of ±6º and ±3º respectively, the best relative energy resolution of the second-order focusing toroidal spectrometer presented in this paper is given approximately by $1.314\theta^3$.

A spectrometer designed to accept a 45º central ray with respect to the vertical axis was found to provide the best predicted resolution. Due to less dispersion and a longer exit focal length, a 60º entrance angle (for a ±6º angular spread) spectrometer geometry has a predicted energy resolution that is more than two times worse. For a 30º entrance angle design, although the dispersion is greater, the second focal point lies within the main body of the spectrometer, making it difficult to place detectors at the seond-order focus plane. For these reasons, a spectrometer designed to accept a 45º central ray is used.

3.2.3   Parallel energy acquisition

Fig. 3.6 shows simulated electron trajectory paths leaving a point on axis with a range of different emission energies through the second-order focusing toroidal

spectrometer design, with no angular dispersion considered. Eleven trajectories are plot in uniform steps over an energy range spanning 90% to 110% of the pass energy. There is clearly considerable energy dispersion at the spectrometer output, where a tilted detector for parallel energy acquisition is marked in the figure. Simulation results also showed that the spectrometer plate geometry can in principle provide greater energy dispersion, more than ±15% (total of 30%) of the pass energy. Although the energy resolution will naturally be much worse at the edges of such a large energy pass band range, there are situations where high transmission of this kind may be useful. In the SEM for instance, electrons close to the centre of a wide energy pass band can be used for spectroscopy, while those outside the centre region can be simultaneously used to form a topographical image of the specimen.
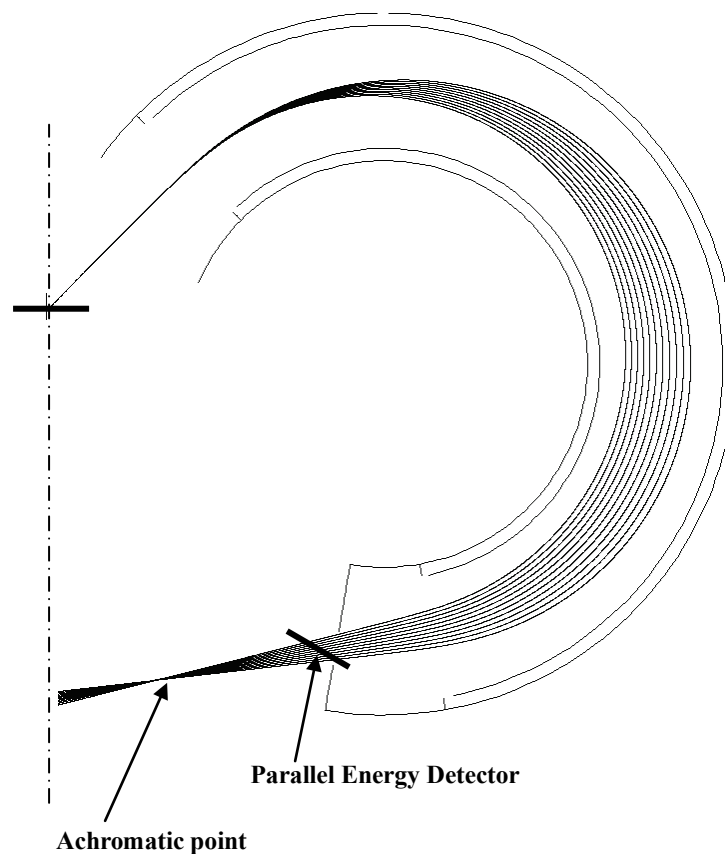
Fig. 3. 6. Simulated zero angle trajectories at 11 emission energies spread uniformly from 90% to 110% of the pass energy

It is interesting to note the existence of an achromatic point located further down the central ray in Fig. 3.6. If the electric field distribution in the spectrometer had been perfectly symmetric before and after the intermediate focus, one would expect a reduction in chromatic aberration, leading to a substantial reduction in dispersion at the output plane, similar to the cancellation of second-order spherical aberration. Fortunately, due to the asymmetric nature of the field distribution in the toroidal geometry, chromatic aberration does not cancel as much as spherical aberration, and a significant amount of dispersion at the output focal plane is predicted: a dispersion of 155 μm is expected for a relative energy spread of 2×10^{-2} (R_1 = 1.4 cm), compared with a trace width of 11.31 μm produced by spherical aberration with an input angular spread of ±6º.

Fig. 3.7a shows a magnified set of simulated rays paths around the output focal plane that have different emission energies and angles. There are eleven different energies uniformly spread over the energy interval ranging from 95% to 105 % of the central band energy (2.293 eV). For each energy, there are eleven trajectories whose input angles are uniformly spread between -52 to 52 mrad around the central entrance angle (45º). Also marked on Fig. 3.7a is the plane normal to the central ray Gaussian focal point, and the line joining the Gaussian focal points on each central energy ray. These results indicate that the influence of spherical aberration for parallel energy acquisition will be greatly reduced if the detection plane is aligned to the line joining Gaussian focal points at different energies, rather than be normal to the central ray. Fig. 3.7b shows the case where the detector plane is orientated to be 26.4º with respect to the horizontal axis, a line that is formed by joining together the Gaussian

focal points of rays at either extreme of the energy band (95% and 105% of the pass

energy). All eleven rays across the energy band appear well focused along this line.

(a)

(b)
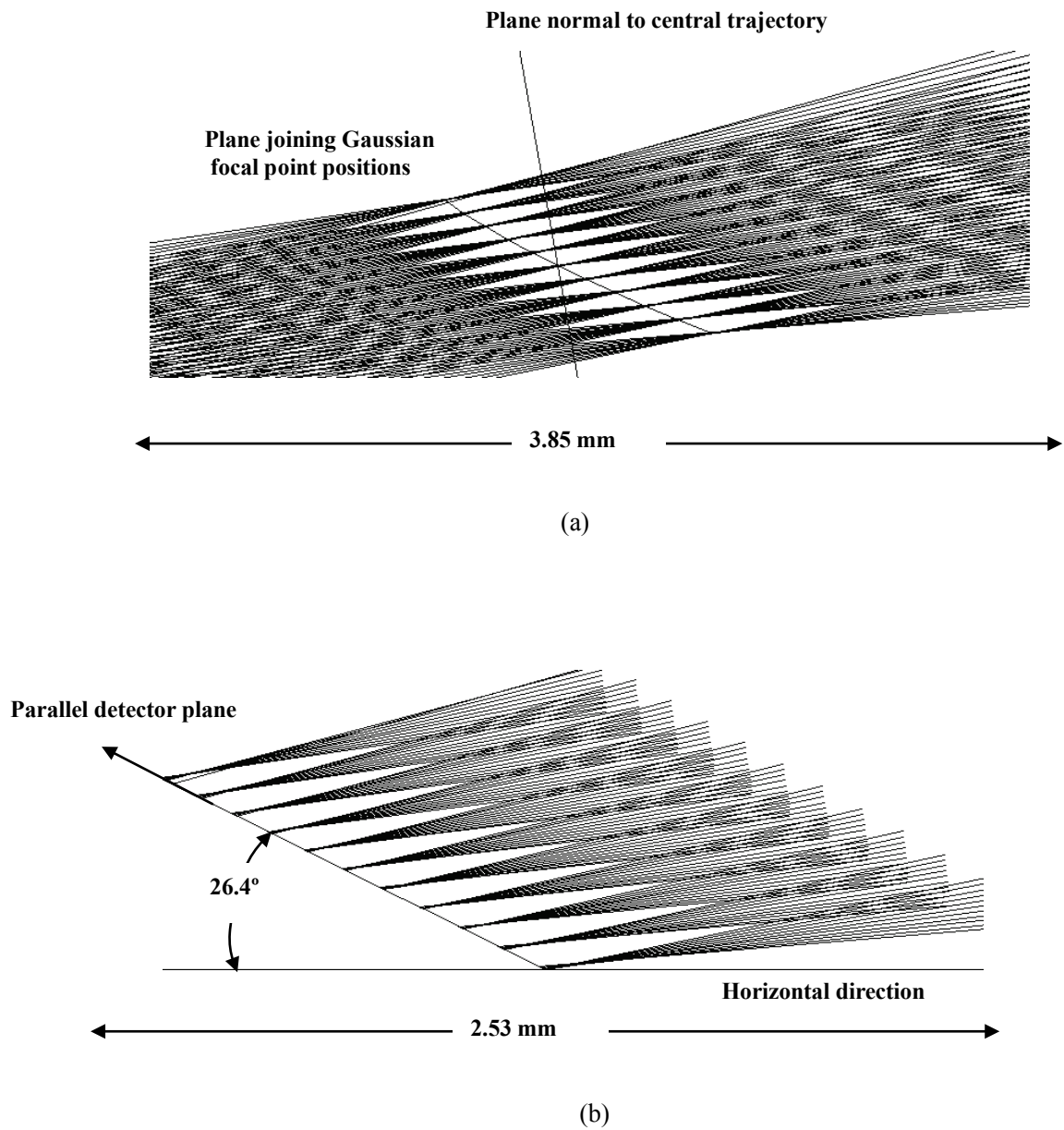
Fig. 3. 7. Simulated trajectories around the output focal plane for 11 emission energies ranging from 95% to 105% of the pass energy and 11 input angles from -52 mrad to 52 mrad around the central ray in uniform steps: (a) the normal plane and line joining up Gaussian focal points; (b) detection plane at 26.4° with respect to the horizontal axis

In order to quantify the information depicted in Figs 3.7a and 3.7b, the rms value of

the trace width at each energy along the detection plane (at angle of 26.4º to the horizontal axis) was calculated, and normalized to its value at the centre of the band. This quantity is a direct measure of the relative rise of the energy resolution across the energy band, and is shown in Fig. 3.8. As expected, there is a relative increase in trace width as a function of how far the pass energy deviates from the central one, however, it rises relatively slowly, meaning that the second-order focusing region extends across a significant portion of the energy band: the trace width limited by spherical aberration rises by less than a factor of two for an energy pass band range defined approximately by 96% to 104% of the pass energy. Within this energy range, the focusing properties of parallel energy detection are still approximately of second-order. By way of comparison, the hemispherical spectrometer in retarding mode, has a bandwidth of only a few percent (the energy range over which its resolution rises by a factor of two to three) [3.20].
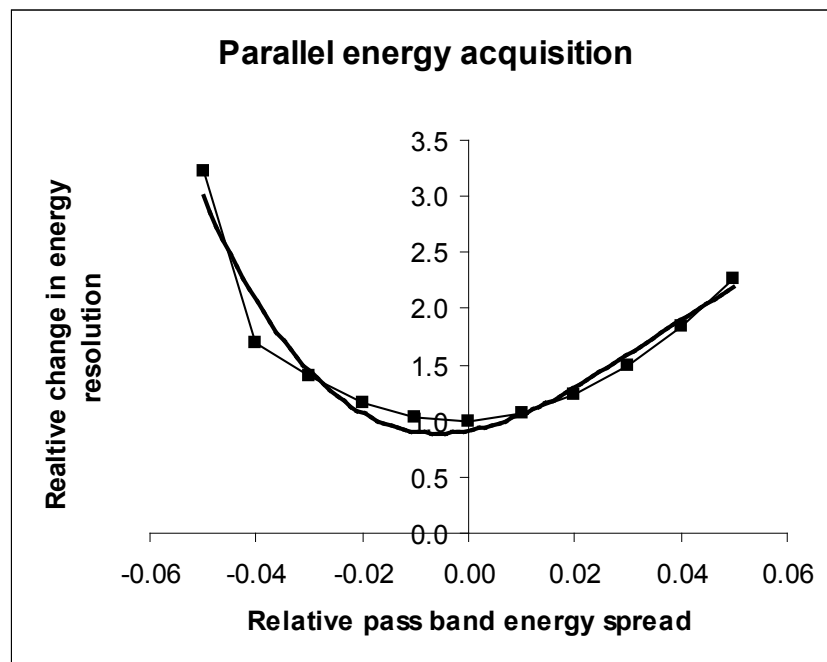
Fig. 3. 8. Simulated increase in energy resolution across the energy band spanning 95% to 105% of the pass energy

How to achieve parallel detection on the surface of a cone which has a slant of 26.4º with respect to the horizontal axis is a matter for future investigation. One possibility may be to use an array of multi-channel flat strip detectors that are evenly distributed in the angular azimuthal direction. Fig. 3.9 shows how a portion of this array would appear looking down on to the detection plane for 40 flat strip detectors, each detector captures electrons over a 9º window in the azimuthal direction. The detector array is placed on the cone slant at the point of second-order focus, the radius, R_D at this point is relatively large, around $1.33R_I$. Due to the relatively shallow angle of the cone slant and its large radius, the size of each flat strip detector is relatively small in comparison to the detection cone surface: it has an extension in the azimuthal direction of approximately $0.157R_D$, and its length on the cone slant for a ±10% wide pass energy band is $0.0749R_D$, giving an apparent width of $0.0669R_D$ in the plan view. These dimensions are relatively small with respect to R_D, which means that the detector array provides a good approximation to the detection cone surface. If α is the semi-angle of collection for each detector, 4.5º in this case, it is straightforward to show from simple trigonometric considerations that the maximum positional error relative to R_D due to the detector being flat is $1 - \cos\alpha$, whose average value is given by, $1 - (\sin\alpha)/\alpha$. This translates to an average positional error of $1.03 \times 10^{-3} R_D$, which when used as an off-set around the optimum position for second-order focusing only results in the spherical aberration trace width growing by 4.7%, giving an energy resolution of 0.152% on each flat strip detector, as opposed to the former value of 0.146% for perfect cone surface detection.
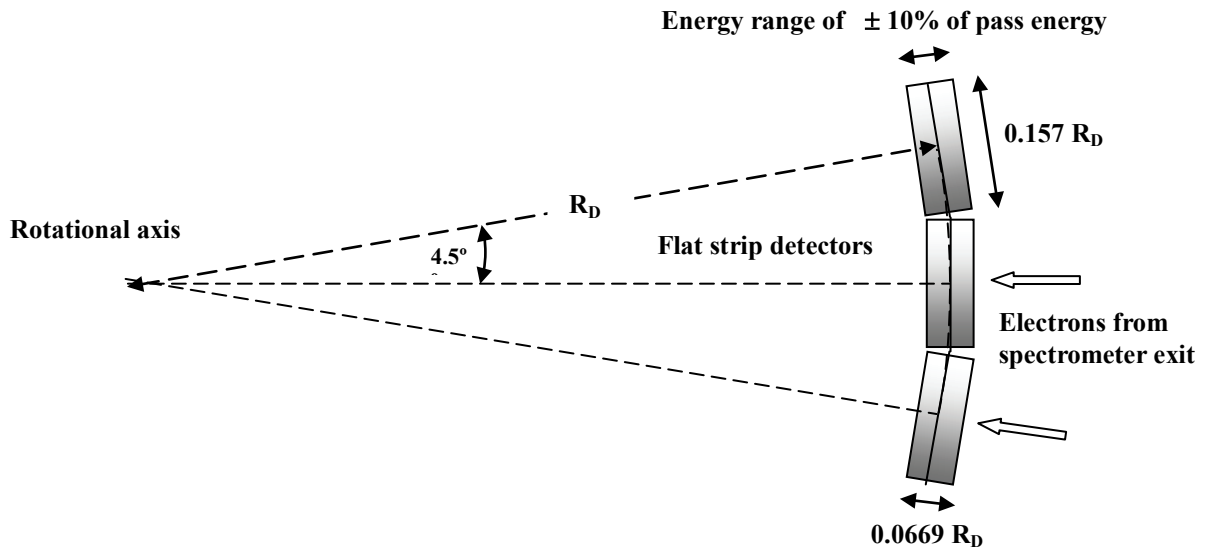
Fig. 3. 9. Part of the plan view of a flat strip multi-channel array in the angular azimuthal direction. 40 strip detectors fit on to the conical detector plane of radius R_D. The 0.0669 R_D apparent width corresponds to 0.0749 R_D in the r-z plane, which captures an energy range of $\pm$ 10% of pass energy.

3.2.4   A parallel detector design for low energy electrons

For relatively low pass energies (typically less than 50 eV), pass energies that are much lower than voltages required to bias the detector (say 1 to 2 kV), a flat plane detector design is possible. In this case, electrons that pass through the spectrometer can be further deflected by an electric field created between a negative lower electrode, biased at V_1, and an upper flat plane detector biased to V_2, typically biased positive to several kV, as shown by simulated trajectory paths in Fig. 3.10. In this example, electron trajectory paths are traced through the spectrometer for five emission energies: 47.5 to 52.5 eV in steps of 1.25 eV , that is, within the 95% to 105% range of a 50 eV pass energy. They enter the spectrometer with eleven angles uniformly distributed between -52 to + 52 mrad ($\pm 3°$), where V_1 = -160V, and V_2 = +2.5 kV.
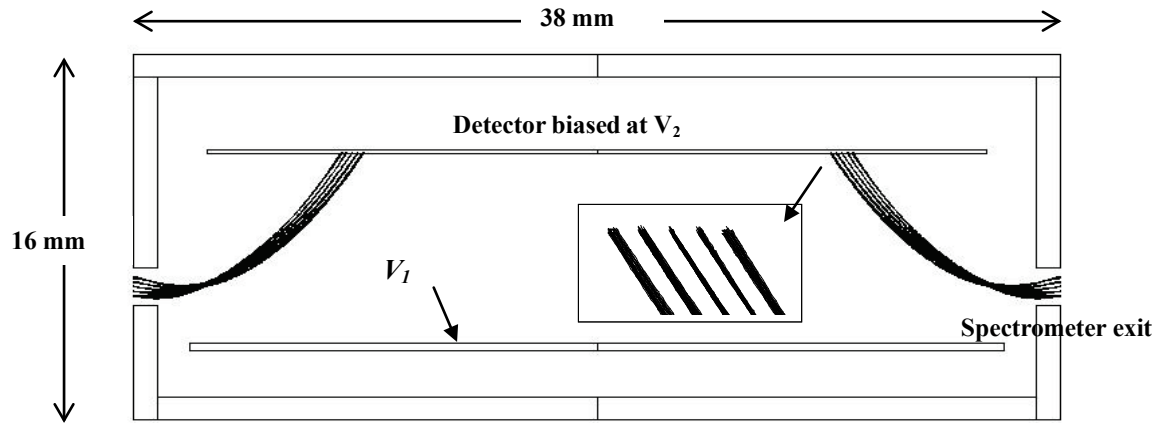
Fig. 3. 10. Simulated trajectory paths for flat plane detection at a pass energy of 50 eV. There are 5 emission energies ranging from 95% to 105% of the pass energy in constant steps, and 11 input angles uniformly varying from -52 mrad to 52 mrad around the central ray (45°). V_1=-160 V, V_2=2500 V.

 The predicted energy resolution on the flat plane detector is 0.196% for the centre of the pass band, and 0.769% for the outer energies (at 95% and 105% of the pass band energy). Although the trace width due to angular dispersion on the flat detection plane is larger than its value on the conical detection plane, the dispersion is also correspondingly larger, leading to the prediction that the energy resolution on the flat plane detector will be only marginally worse than its value at the conical detection plane, 0.196% compared to 0.146% respectively. These simulation results indicate that at least for relatively low pass energies (< 50 eV), the complications of detection on a conical surface may be avoided.

3.3 Experimental results from a toroidal spectrometer attachment for the SEM

In the previous section, simulation of a second-order focusing toroidal spectrometer design has been presented. This section presents experimental results from a spectrometer prototype based upon this design as an attachment inside the SEM. Both SE and the BSE energy spectra are recorded. By monitoring the BSE spectrum, the

energy resolution of the spectrometer is estimated. In addition, a specimen bias technique is developed to enhance the signal-to-noise ratio (SNR) of the spectrometer.

3.3.1 The experimental setup

Fig. 3.11 depicts the experimental setup of the spectrometer, fit as an attachment inside a conventional SEM. The inner sector is grounded and the outer sector is biased with a negative potential $-V_D$ that is ramped to capture the scattered electron spectrum. The spectrometer is designed to capture an angular spread of $\pm\ 8^{\circ}$ with respect to the central entrance angle of 45° in the polar direction. The input angular spread in the azimuthal direction is 100°. In this design, the specimen is surrounded by two hemi-spherical caps, where the inner cap is electrically connected to the specimen and the outer cap is grounded. This arrangement keeps a field-free region around the specimen surface while setting up a radial field in the space in between the two caps, allowing the specimen to be biased to a certain negative or positive potential. This arrangement can be used for extraction and collimation of SEs into the spectrometer. An aperture is placed vertically at the spectrometer exit to select electron energy. The aperture has a thickness of 100 μm and its width is fixed around 100 μm for all the following experiments. A scintillator is used to convert the output electrons into light, which is then detected by a photo multiplier tube (PMT). The whole setup is placed right below the final pole-piece of the SEM objective lens to minimize the working distance, as shown in Fig. 3.11. The minimum working distance for this setup is 15 mm. For the acquisition of SE spectra, the scintillator voltage, V_{SC}, was biased to +5 kV. A 3D drawing of one half of spectrometer attachment prototype is illustrated in Fig. 3.12.
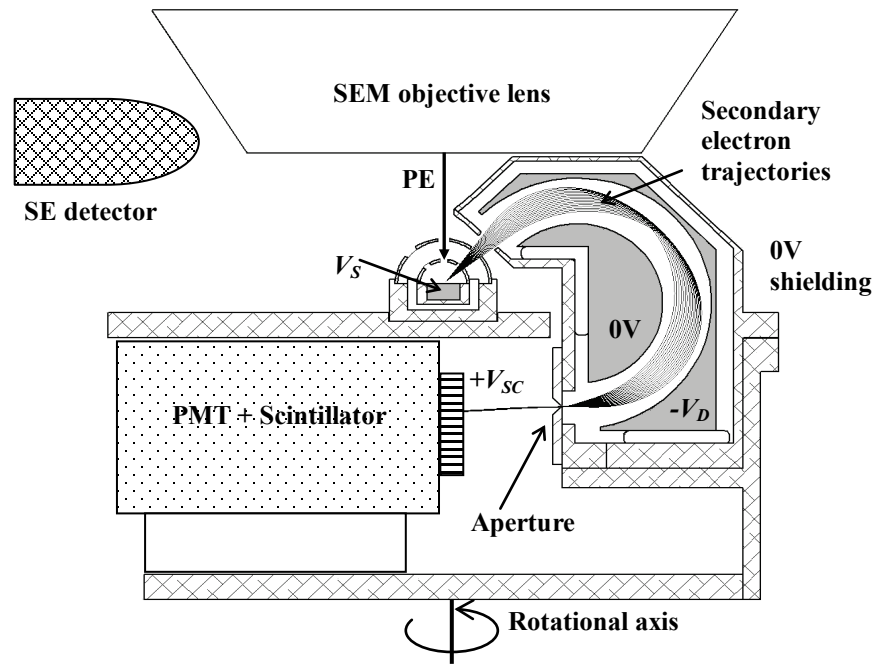
Fig. 3. 11. Experimental layout of the high-resolution toroidal secondary electron spectrometer inside the SEM. 16 electron trajectory paths with an input angular spread of $\pm\,8^{\circ}$ around the central angle of 45° are simulated.
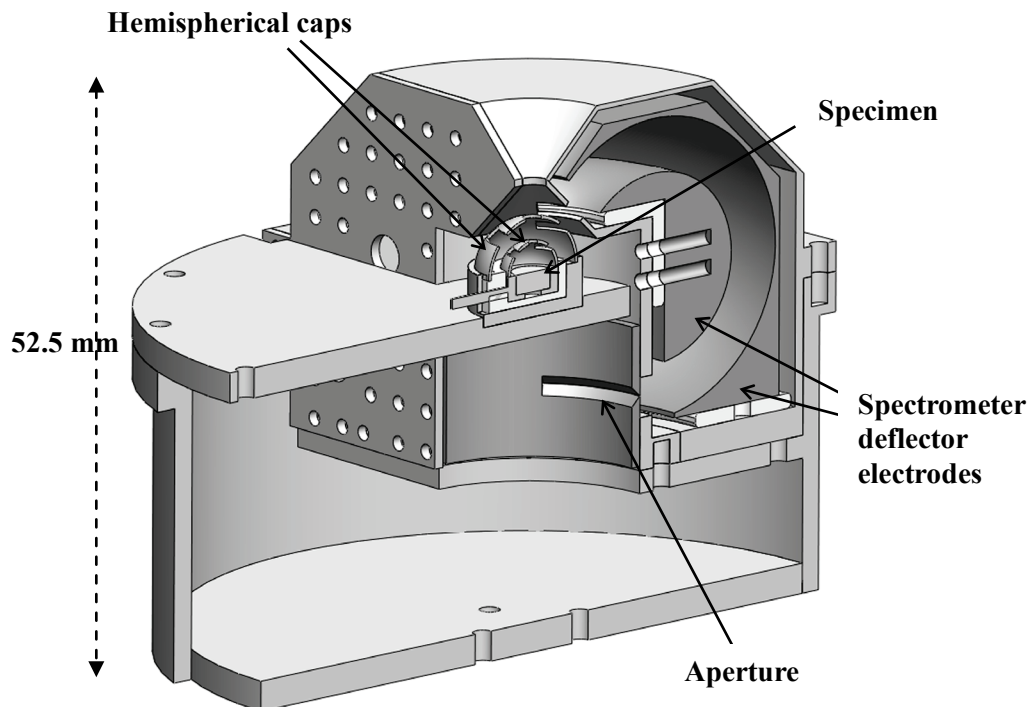
Fig. 3. 12. A prototype of the toroidal spectrometer attachment (a half). The azimuthal deflection angle is 100°. The whole attachment is placed on the SEM stage for experiments.

Fig. 3.11 also depicts 16 simulated secondary electron trajectory paths traced from the specimen through the spectrometer on to the scintillator, demonstrating how the spectrometer functions. The electric field distribution solution and electron trajectories were obtained by running the program, LORENTZ-2EM [3.18]. In this simulation, the specimen and the inner cap were grounded. The scattered electrons are emitted from the specimen in all directions and a wide range of energies, from the low energy secondary electrons through to the elastic backscattered electrons enter the spectrometer. However, only electrons having an initial energy around the spectrometer pass energy with polar emission angles between 37° to 53° will travel through the spectrometer and strike the scintillator.

3.3.2 The secondary electron spectrum and voltage contrast effects

A chromium specimen was used to investigate the SE spectrum inside the SEM. The specimen was cleaned by using an ultrasonic cleaner with acetone solvent. The specimen was polished to have a smooth surface, in order to minimize the influence of surface topography. All experiments were carried out inside a Tungsten JEOL JSM-5600 SEM, where a 5 kV, 10 pA primary beam was focused on to a 3 nm diameter spot on the specimen. The deflection voltage V_D in Fig. 3.11 is software controlled through a Personal Computer (PC), and the output signal on the PMT is fed into an electrometer, converted into a digital signal and monitored by the PC as V_D is scanned. Around 150 to 200 points are used in the generation of a full SE spectrum, with each point having a primary beam dwell time of 0.1 s on the specimen. The output signal is typically captured at a rate of around 3 points per second. Hence, the total acquisition time for each spectrum is about 50-100 s.

Agilent E3631A triple output power supplies were used for the spectrometer deflection voltage as well as specimen biasing. The voltage ripple of this power supply is less than 0.35 mV rms and the voltage drift over a single spectrum acquisition is less than 8 μV.

Fig. 3.13a shows an experimentally acquired SE spectrum, while Fig. 3.13b displays a selected part of it, in order to study the noise on the signal. In this experiment, the specimen and the inner cap were grounded. The deflection voltage here refers to V_D in Fig. 3.11, the voltage of the outer sector plate. Fig. 3.3b shows that the noise is relatively small, allowing for SE spectral shifts of 12 mV or lower to be monitored, about 5 times better than the multi-channel SE spectrometer proposed by Kienle and Plies [3.21].
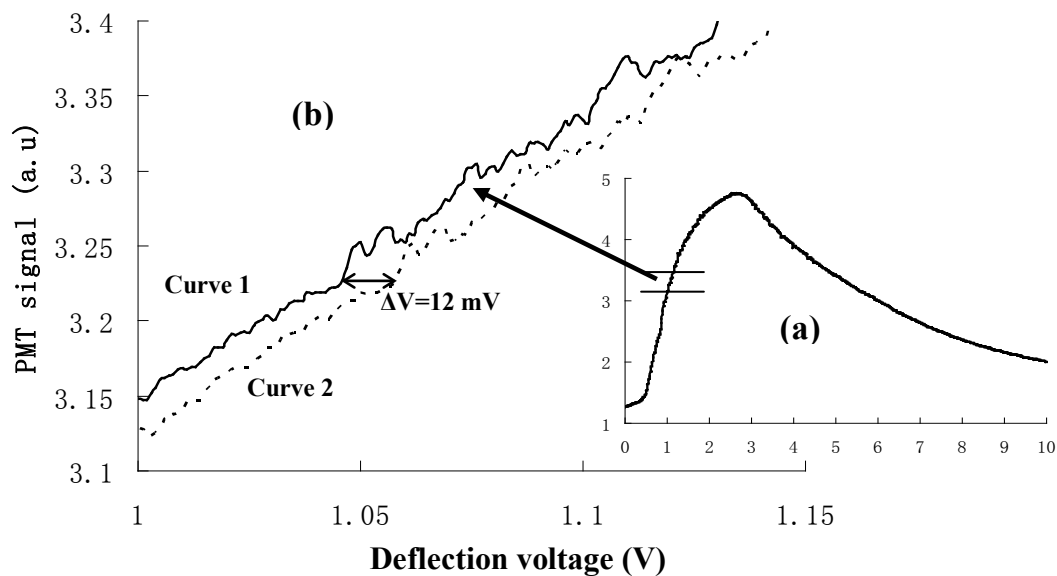
Fig. 3. 13. An experimental SE spectrum: (a) full range; (b) selected range in which curve 2 is shifted 12 mV with respect to the curve 1.

For the next experiment, the specimen is biased with a negative voltage together with the inner cap, while keeping the outer cap grounded. Fig. 3.14 shows the output

signals of the collected SEs as a function of deflection voltage at different negative specimen biasing voltages. Compared to 0V bias, the output signal not only shifts to the right (as expected) but also grows significantly in intensity as the biasing voltage increases, forming a sharper peak, which no longer directly represents the SE spectrum. The increase in signal height comes from the fact that negative specimen voltages accelerate secondary electrons towards the spectrometer entrance, giving them a higher pass energy, enabling a wider energy range to travel through the spectrometer exit slit. This negative biasing also creates an accelerating leakage field that penetrates into the inner cap near the specimen surface, creating a weak lens focusing action, and effectively widening the angular spread into the spectrometer. Since the output aperture size is unchanged, a correspondingly higher proportion of secondary electrons pass through the output slit. The electric field generated between the inner and the outer caps pulls through secondary electrons that would otherwise strike the inner surface of the inner cap. Simulations confirmed that this effect contributed to the increase in SE signal height as the specimen/inner cap were biased negatively, in addition to a wider range of energies passing through the spectrometer exit slit. Details of this effect will be discussed later.

Although the SE spectrometer output signals no longer represent the SE energy spectrum as the extractor field increases (more negative specimen voltages), they are in a more useful form for the purposes of quantifying specimen contrast effects due to the formation of a sharp peak. These results illustrate an important point about the acquisition of the SE spectra in general: high energy resolution is not required, and accurate recording of the SE energy spectrum is unnecessary. By biasing the specimen/inner cap negatively, the SE spectrum is transformed into a much more

convenient form for open-loop specimen voltage measurement than the original SE spectrum. If the surface potential does not change by large amounts over the area scanned, it is possible to store several images, each at a different analyzer deflector voltage, thereby obtaining an estimate of the peak position in the output signal for each pixel in the image. In this way, a quantitative voltage map can be superimposed upon the normal SE image, rapidly acquired in open-loop mode.
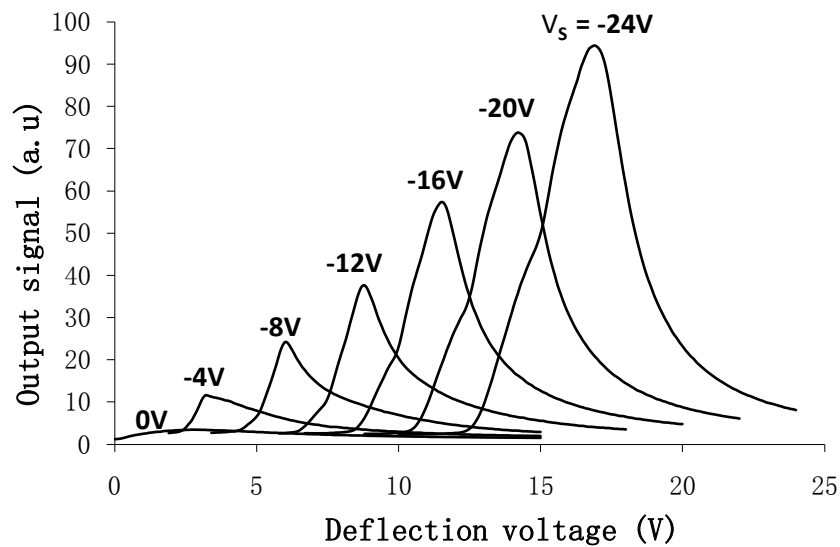
Fig. 3. 14. Experimental secondary electron output signals at different specimen biasing voltages.

Not only does the output signal develop a sharp peak, which can be precisely tracked as a function of specimen potential, but the signal-to-noise ratio is more than an order of magnitude higher than the case when there is no specimen bias. This is illustrated by the experimental signals shown in Fig. 3.15, where the bias voltage on the specimen/inner cap changes from -10 to -10.1 V. In this case, the spectrometer deflector voltage is restricted to a small range (1 volt) around the peak signal value. The presence of shot noise on these signals is relatively small, less than 4mV, a few times better than the case of 0V bias.
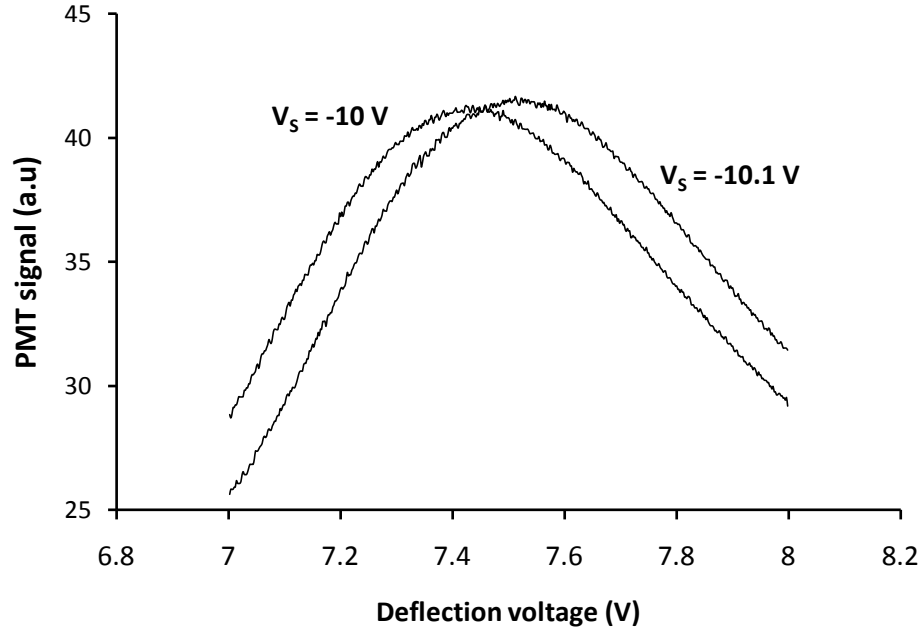
Fig. 3. 15. Experimental secondary electron signals for the specimen voltage changing from -10V to -10.1V.

A higher estimate of the signal-to-noise ratio (SNR) on the experimental signals shown in Fig. 3.15 is obtained if signal mean around the peak value is monitored. The signal mean for each signal (deflection voltage average) is given by expectation value $E(V)$:

$$E(V) = \sum_{j=1}^{N} P_j V_j \qquad (3.3)$$

where the index j runs from 1 to the number of points sampled in the output signal that is examined, N; V refers to the deflector voltage; P_j refers to the probability of each point in the output signal, obtained from the output height normalized to the area under the output curve. The expectation function is a convenient way of monitoring small changes in the peak value, since the peak position shifts significantly as the specimen voltage changes. Also, it takes advantage of the fact that the peak shape is approximately symmetric. If the peak is perfectly symmetric for the deflector voltage range monitored, the expectation value provides the peak position along the x-axis

(deflector voltage), and the noise on either side of it cancels out, providing a measure of specimen voltage changes in the output signal, which are relatively insensitive to the noise present on the signal. These points are illustrated by examining the expectation values of the signals shown in Fig. 3.15, in which the number of samples, N=500 is used. Here the expectation values are E_1 = 7.49405 V for V_S = -10 V, and E_2 = 7.511865 V for V_S = -10.1 V, giving a change of ΔE_S = $E_2 - E_1$ = 17.8154 mV for the specimen/inner cap voltage changing by 100 mV. The change in expectation value (refer to the noise ΔE_N) due to shot-noise of each signal is calculated by comparing its expectation value to the expectation value of a smoothed fit. For the signal at V_S = -10.1 V, ΔE_N is calculated to be 6.272 μV, giving a signal-to-noise ratio of 2,840 (SNR = $\Delta E_S/\Delta E_N$ = 17.8154 mV/6.272 μV). Assuming that the minimum measurable voltage occurs at a signal to noise ratio of unity, this sets the minimum detectable shift due to shot noise to be around 32.2 μV. These kind of low noise spectra are expected to be useful for mapping dopant carrier concentrations in semiconductor devices, where shifts in SE spectra of several mV need to be monitored [3.22].

Simulations were carried out to help understand the specimen biasing effect. The specimen and the inner cap were biased as the same potential V_S = V_{cap}, while the outer cap was grounded. The width and the thickness of the output aperture were set to 200 μm and 100 μm respectively. A Chung-Everhart SE distribution was assumed for the simulations, as shown in Fig. 3.16, in which the energies taken for simulation are represented by the dots. For each energy, the total number of electrons corresponds to the "area under the graph" with the width is taken as the difference between neighboring midpoints on either side, and this width is then multiplied by the average intensity value. This provides a normalized current value that is assigned to

each ray plot by the Lorentz software [3.18]. More take-off energy points are used in the low energy range of the spectrum, and take-off energies above 23eV do not contribute to the collected signal. In that way, 41 discrete energy intervals are graded from the minimum value of 0.02eV in the low energy region (around the peak) to about 2eV in the high energy region (near the tail of the spectrum).
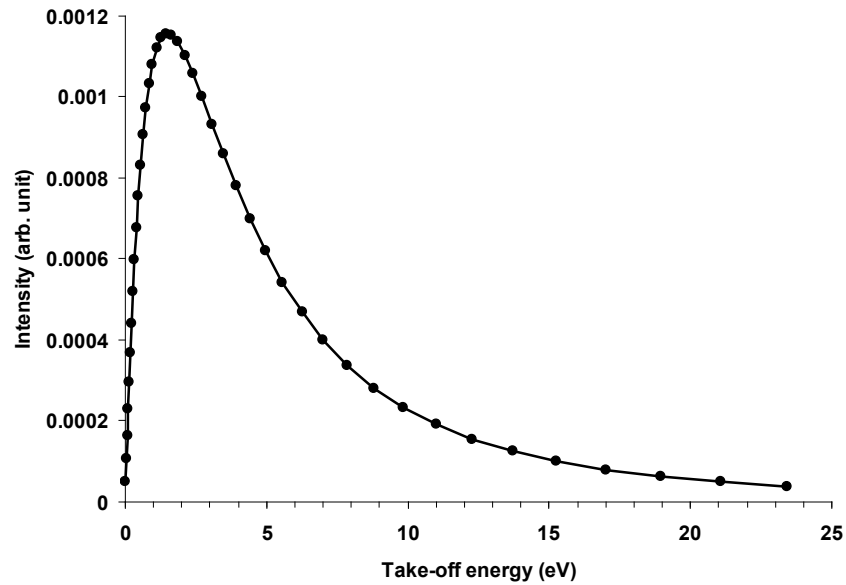
Fig. 3. 16. Chung-Everhart distribution of the SE emission used in the simulation.

Fig. 3.17 shows examples of simulated trajectory paths from the specimen to the positively biased scintillator for 42 emission energies ranging from 0.02eV to 23eV in graded steps, as shown in Fig. 3.16, and 30 emission angles from 30° to 60° in uniform steps. Scattered electrons over a wide range of energies and angles can enter the spectrometer, but among them only electrons within a small energy window can go through the output aperture to be detected. A few trajectories on the left side illustrate that very few low energy electrons can even be reflected from the slit of the first cap to travel through the slit on the other side to enter the spectrometer.
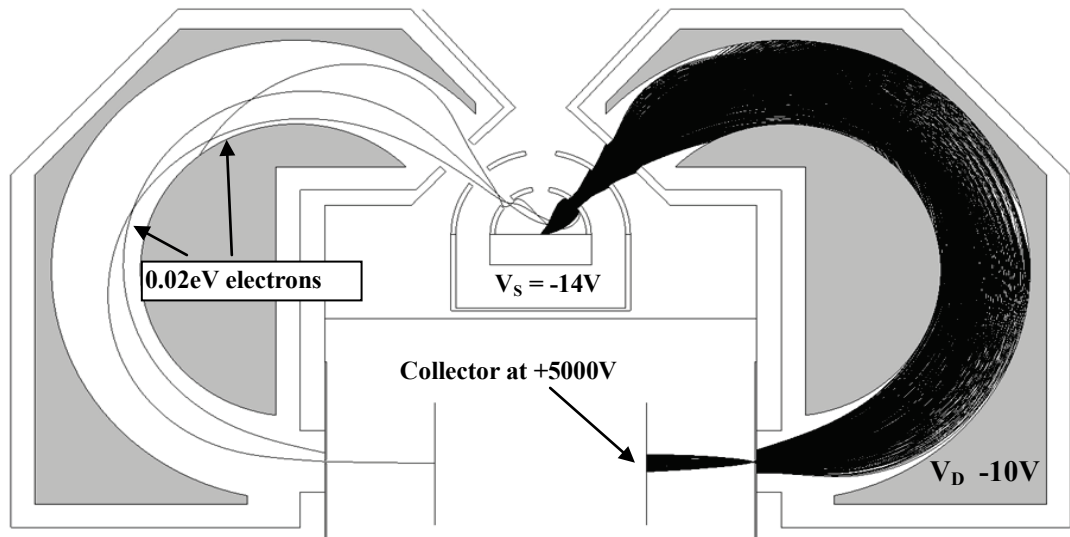
Fig. 3. 17. Simulated electron trajectory paths of a wide range of energies and angles through the spectrometer.
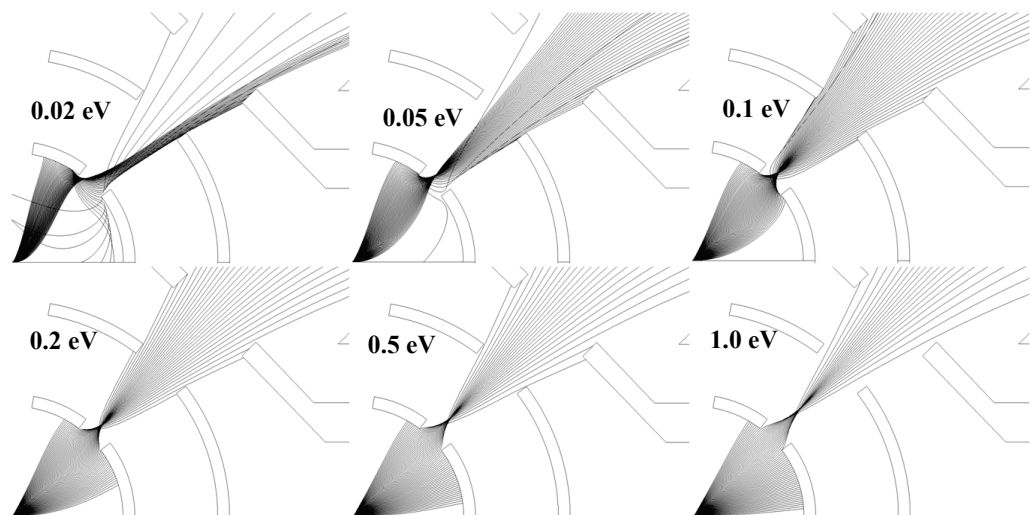
Fig. 3. 18. Electron trajectories traced from specimen through the cap arrangement to enter the spectrometer of different energies below 1eV. 60 trajectories of each energy with the polar angular spread from 1° to 60° in step of 1° are plot.

Fig. 3.18 shows simulated emitted electrons for various energies and a take-off angular range of 1° to 60° in steps of 1°. The specimen bias is -14V. Fig. 3.18 indicates that the polar angular range of electrons that enter the spectrometer is highly energy dependent at low energies. In general, scattered electrons with take-off energies below

1.0 eV are pulled into the toroidal deflector by the electric field set up by the specimen bias.

Fig. 3.19 shows the simulated upper and lower limits of the polar angular range accepted into the toroidal spectrometer for different take-off energies at a specimen/inner cap bias of -14 V. It shows that the accepted take-off polar angular range into the spectrometer is sharply energy dependent at low energies. In general, scattered electrons with take-off energies below 1.0 eV are pulled into the toroidal spectrometer by the electric field set up by the specimen bias. Therefore, more low energy electrons enter the spectrometer, up to a 50º range for 0.1 eV SEs, compared to the 16º acceptance polar angle range for zero specimen/inner cap voltage. When the specimen is biased, the kinetic energies of low energy electrons increase by several orders of magnitude, greatly increasing the number of secondary electrons that pass through the spectrometer exit slit, creating a sharp peak in the output signal that has a much higher amplitude than the case for no biasing.
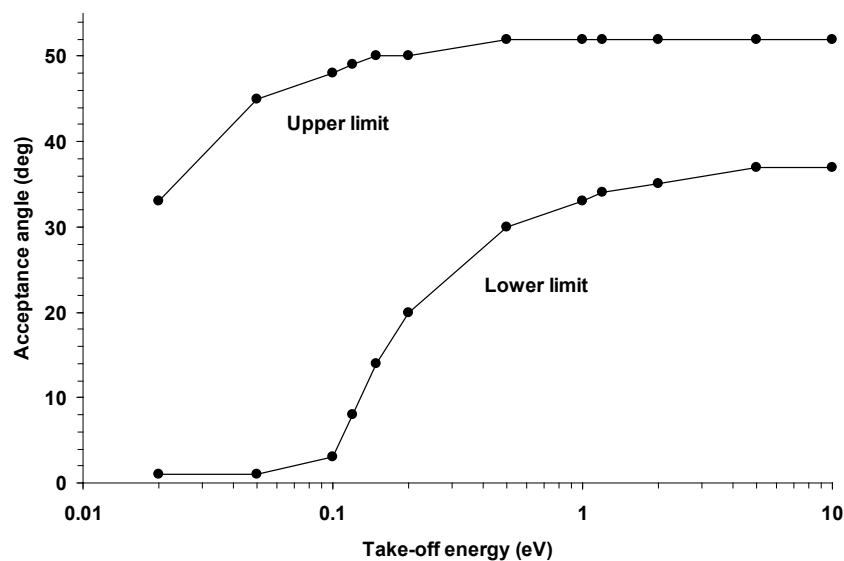
Fig. 3. 19. Collection efficiency of different SE energies through the two hemispherical caps when the inner cap is biased at -14 V
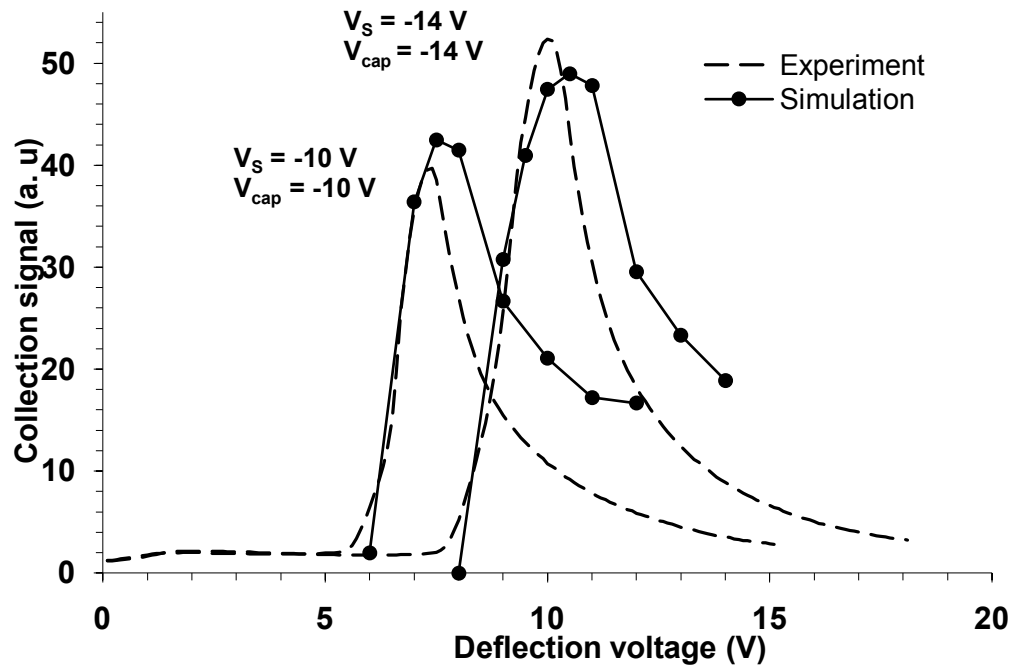
Fig. 3. 20. Comparison of experimental and simulated SE output signals for the specimen/inner cap voltages of -10 and -14 volts.

The simulated SE collection current was compared to the experimentally obtained spectrum as illustrated in Fig. 3.20, for two specimen/inner cap voltages, -10V and -14 V. It shows that the relative position of the simulated and experimentally obtained curves match closely, with the rising edge almost identical. However, the simulation curve width is larger than the experimental one. This may be due to manufacturing tolerance and differences in the energy distribution of the experimental signal from that assumed in the simulation model (Chung-Everhart distribution). In addition, the BSEs from specimen, which would strike the hemispherical cap, may reflect back to the specimen to generate more SEs. It may also be due to poor electrical connection between the specimen and the inner cap as well as specimen charging, causing the actual potential of the specimen to differ from that of the inner cap. Two other bias conditions were simulated to further understand these effects: firstly, where the

specimen bias is more negative than the inner cap bias, and secondly, where the specimen bias is less negative with respect to the inner cap bias. The results show that when the specimen voltage is more negative than the inner cap the simulated curve fits better to the experimental one than the other two cases where the specimen bias potential is either the same or less negative than the inner cap voltage. The best fit to the experimental spectra is obtained when the specimen voltage is set to be one volt more negative than the inner cap voltage. One possible explanation for this is that the specimen is locally charged up to create a more negative potential compared to the inner cap.

3.3.3 BSE spectrum acquisition

The spectrometer was tested inside a JEOL 5600 Tungsten gun SEM using a 5 keV primary electron beam. The BSE spectra for different elements were recorded. Fig. 3.21 shows experimentally obtained BSE spectra for specimens made from Gold (Au), Chromium (Cr) and Aluminum (Al) and Carbon (C). The acquisition time for each spectrum is approximately 2 minutes. This acquisition time is limited by the response time of the power supplies as well as the detector system. In principle, faster acquisition times are possible for better power supplies and detectors. Note that, each spectrum plot here is a single recorded data set that contains the shot-noise of the setup. It is clear that the shot-noise of the setup is relatively small. These experimental results illustrate how the BSE spectrum changes with specimen atomic number, which as expected, generates higher BSE yields and narrower widths as the atomic number rises.

The BSE spectrum obtained from the spectrometer is also compared to Monte-Carlo

(MC) simulations [3.23]. Fig. 3.22 presents how the experimental BSE spectrum of Gold is close to its MC-simulation one. It is clear that the two spectra match closely with one another.
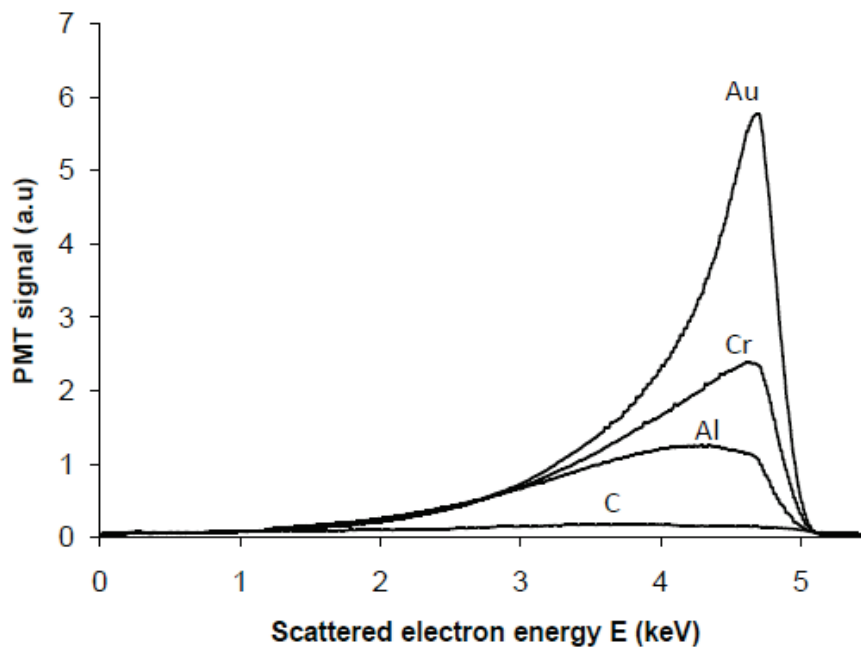
Fig. 3. 21. BSE spectra of different materials
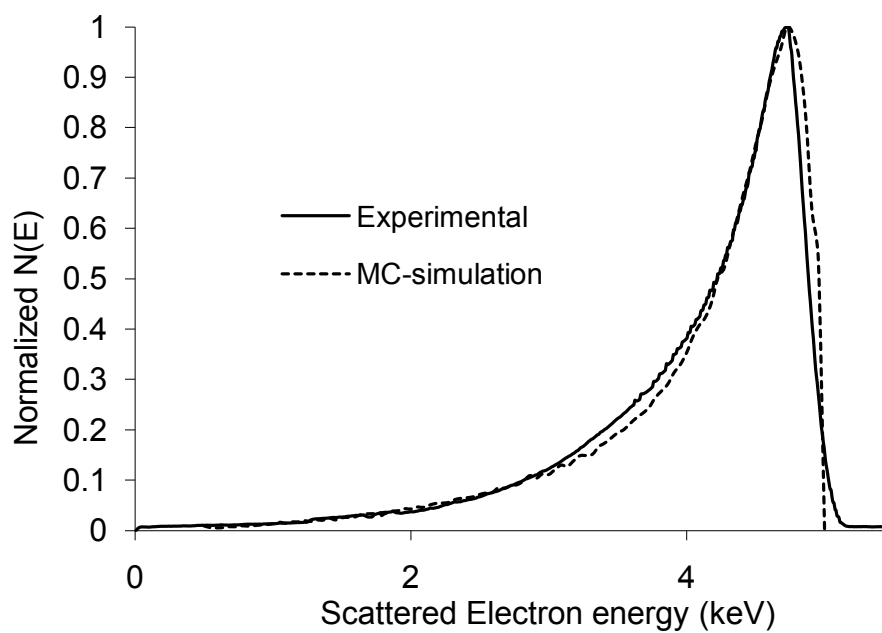
Fig. 3. 22. Experimental and MC-simulated BSE spectra of Gold.

3.3.4 Material quantification from the BSE spectrum

It is well known that backscattered electrons can be used for composition contrast due to the variations of the emitted signal on the effective Z-number. This information is usually used in imaging mode, qualitatively illustrating sample areas of different composition by brightness variations. Previous work on using backscattered electrons to estimate atomic number have for the most part, been based upon calculating the backscattered yield coefficient η [3.24-3.25]. Although some degree of energy filtering has also been attempted [3.26-3.27], it was not based upon acquiring the shape of the energy spectrum, as proposed here, but was still reliant on calculating the backscattered yield coefficient.
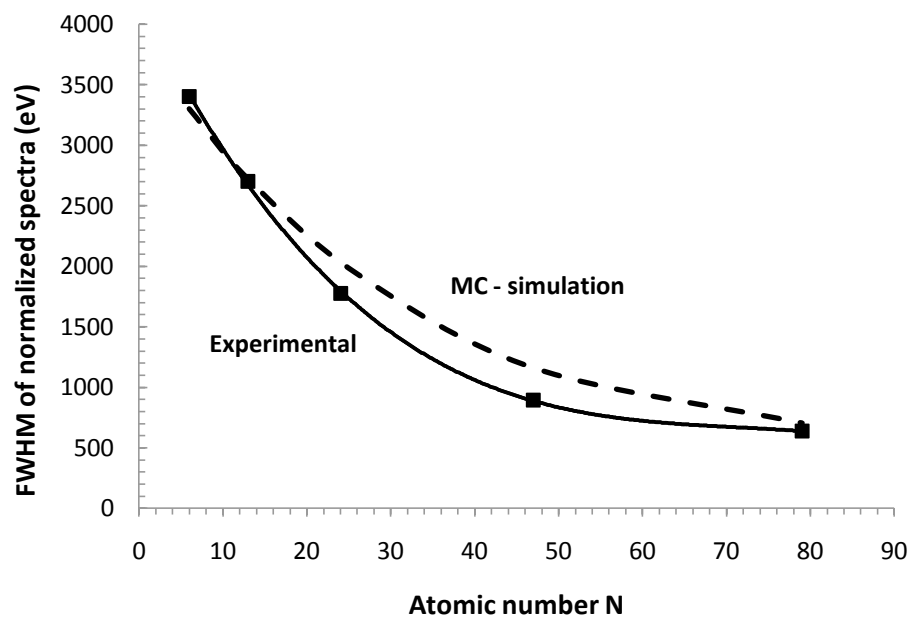
Fig. 3. 23. Dependence of the BSE spectrum full width at half maximum (FWHM) on atomic number. Curve fitting was used for both experiment and simulation. The black square dots indicate actual measured values

Here a new method for quantifying material contrast from the BSE spectrum is

presented, which is based upon monitoring its full width at half maximum (FWHM) height. A graph illustrating how the FWHM changes with atomic number from experimental data together with the MC-simulation is shown in Fig. 3.23. The experimental curve is more sensitive to material contrast variations than the MC-simulation curve. It also shows that the FWHM is more sensitive for light elements than for heavy elements.

To estimate how effective the method is in differentiating between materials that have similar atomic numbers, an approximate calculation for the signal-to-noise ratio (SNR) is performed by comparing changes in the FWHM parameter for close atomic numbers with the changes in the FWHM parameter caused by noise. Measurements to distinguish Silver, Ag (atomic no. 47) from Palladium, Pd (atomic no.46) were made. The spectra of Ag and Pd were acquired through the spectrometer and were normalized as shown in Fig. 3.24. It shows that the Palladium spectrum is wider than that of Silver. Each spectrum is then fit with a high order polynomial around its half maximum height. The signal is then calculated from the difference of their respective FWHMs. The noise is taken as an average variations of FWHM around the one for the fit function. The results are as follows: for Silver and Palladium, the signal from their respective FWHMs is $S_{\text{Ag-Pd}}$ = 122.8 eV, while the noise of Silver is N_{Ag} = 5.249 eV and the noise of Palladium is N_{Pd} = 4.928. So that the SNR to distinguish Silver from Palladium is $\text{SNR}_{\text{Ag-Pd}}$ = 122.8/5.249 $\approx$ 23.4 while the SNR to distinguish Palladium from Silver is $\text{SNR}_{\text{Pd-Ag}}$ = 122.8/4.928 $\approx$ 24.9. These high SNR results are sufficient to indicate that it is feasible to use the toroidal spectrometer to perform quantitative material analysis in the SEM by capturing of the BSE spectrum and monitoring a parameter related to the shape of the spectrum, such as its full width at half maximum (FWHM). This method has the advantage of being much simpler than the

backscattered coefficient method, since it is dependent on less parameters (it for instance, avoids the need to measure the beam current), and is also much less affected by topographic contrast.
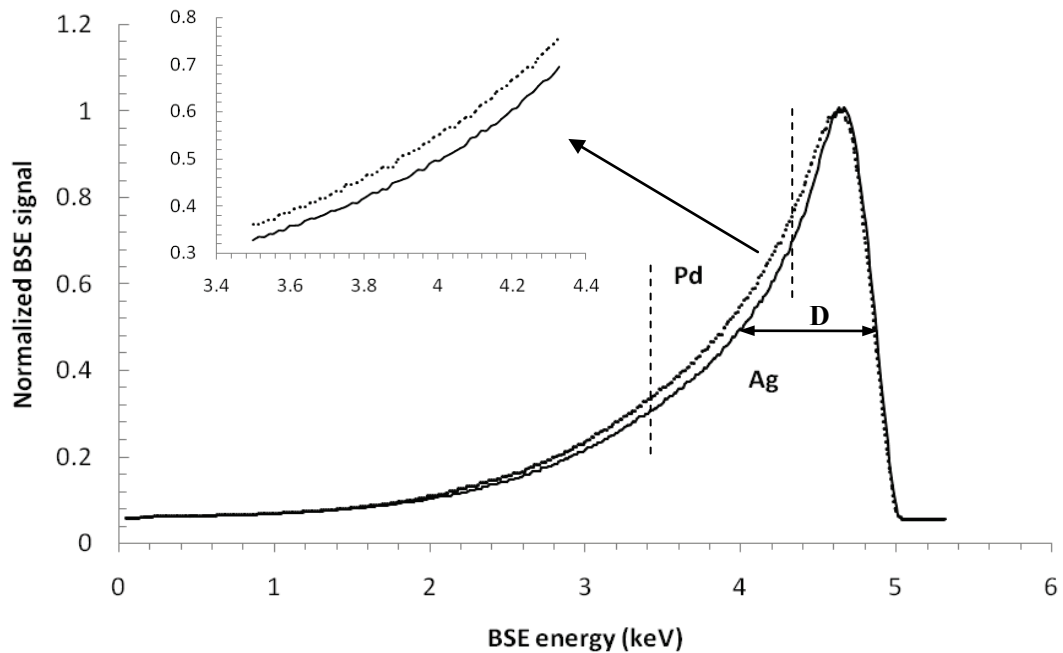
Fig. 3. 24. BSE spectra of two close atomic number elements, Silver and Palladium. D represents the FWHM of the spectrum.

3.3.5 Energy resolution measurement.

Energy resolution is an important parameter characterizing the performance of any electron energy spectrometer. For the recent attachment design, the energy resolution was simulated to be 0.32% (haft-width) corresponding to an angular spread of ±8°. Fig. 3.25 shows simulated trajectories of three energies with an energy difference of 2% from each other, visually depicting the predicted resolution of the spectrometer for an angular spread range of ±8°. An annular aperture of 100m is also presented in this simulation to illustrate how it operates. In principle, smaller apertures (same size of the beam width or less) can be used to achieve the best attainable spectrometer

resolution. In the recent experimental setup, however, it is very difficult to make an aperture smaller than 100 μm.
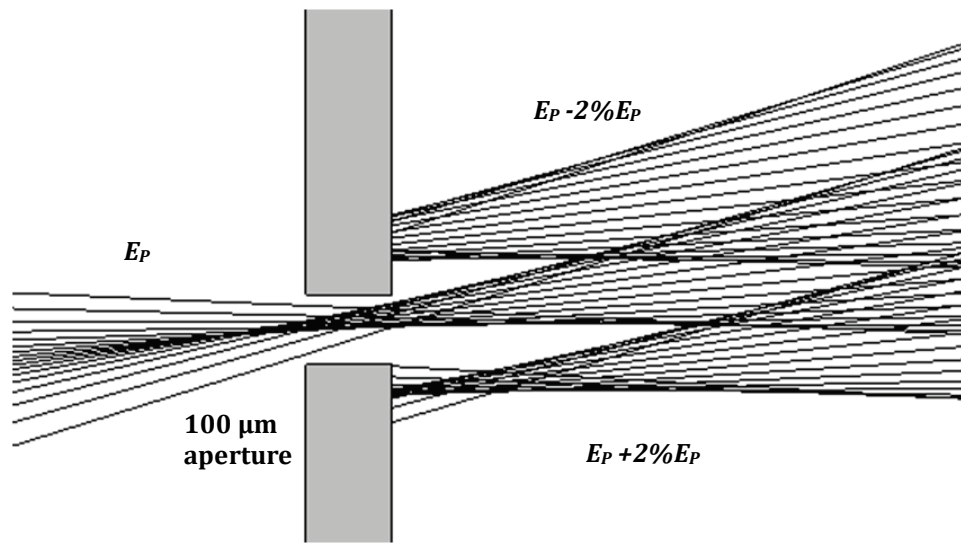
Fig. 3. 25. Simulated electron trajectories of three different energies around an aperture of 100 μm for an angular spread range of $\pm 8°$. E_P is the pass energy of the spectrometer. The aperture thickness is also 100 μm.

Ideally, a sharp electron spectral peak with small width such as a BSE elastic peak should be used to estimate the energy resolution of the spectrometer. However, it is not possible to generate such a narrow spectral peak inside the poor vacuum of conventional SEM chambers. Here, an alternative method to estimate the energy resolution of the recent spectrometer design is employed, one that uses the BSE spectrum. The method is based up on the fact that the measured BSE energy spectrum from the spectrometer comes from the convolution of two spectra: the spectrometer/slit energy response (window), and the intrinsic BSE energy distribution. The intrinsic BSE spectrum (unlimited by the spectrometer/slit) falls to zero discontinuously, characterized by a corner at the top part of its spectrum. The experimentally measured BSE spectrum falls in a smooth continuous way, and can be modeled as the convolution of a BSE discontinuous intrinsic signal with a Gaussian shaped spectrometer signal, as depicted in Fig. 3.26. A Gaussian shaped spectrometer

signal comes from both finite exit aperture thickness and spherical aberration, different from an ideal step-function response, as illustrated by the dotted-line window in Fig. 3.26. The full-width of the assumed Gaussian analyzer energy distribution (at half-height) is taken to be equal to the ideal energy window limited by the aperture, as illustrated in Fig 3.26. The intrinsic BSE spectrum can easily be constructed from the measured BSE spectrum by using its falling slope and projecting it linearly on to the energy axis. Two aperture sizes were used, 200 μm and 100 μm wide, both 100 μm thick. For each aperture, the BSE spectrum was measured, and the full-width (at half height) of an assumed spectrometer/slit Gaussian energy distribution was varied and combined with the intrinsic BSE energy distribution by convolution, to produce a "simulated" output signal, as shown in Fig. 3.27. The Gaussian full-widths that produced the best fit to each experimentally measured signal were monitored $(\Delta E_1$ and $\Delta E_2)$, and taken to represent the analyzer/slit energy resolution. The solid lines in Fig. 3.27 represent conditions of best fit for each aperture. In this way, the analyzer slit energy resolution was estimated to be $\Delta E_1 = 1\%$ (for the 200 μm wide aperture), and $\Delta E_2 = 0.6\%$ (for the 100μm wide aperture).

Energy window   **Intrinsic BSE spectrum**   **Measured BSE spectrum**
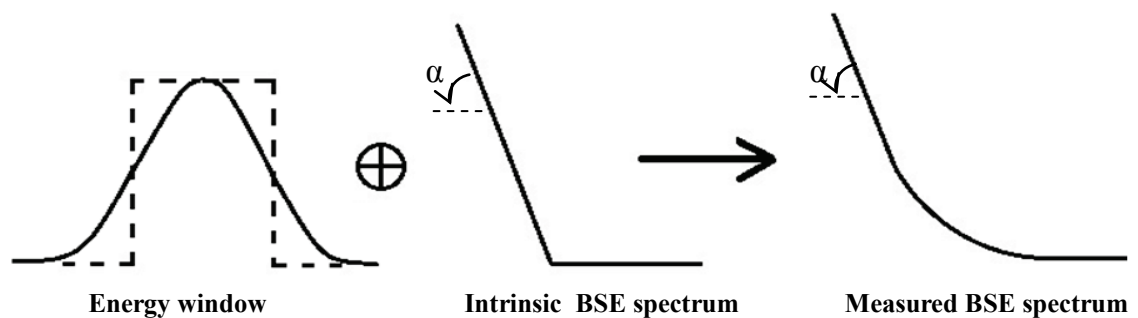
Fig. 3. 26. Convolution of an energy window with an intrinsic BSE spectrum results in the measured BSE spectrum. The dashed line indicates the ideal energy window that is approximated by a Gaussian one.
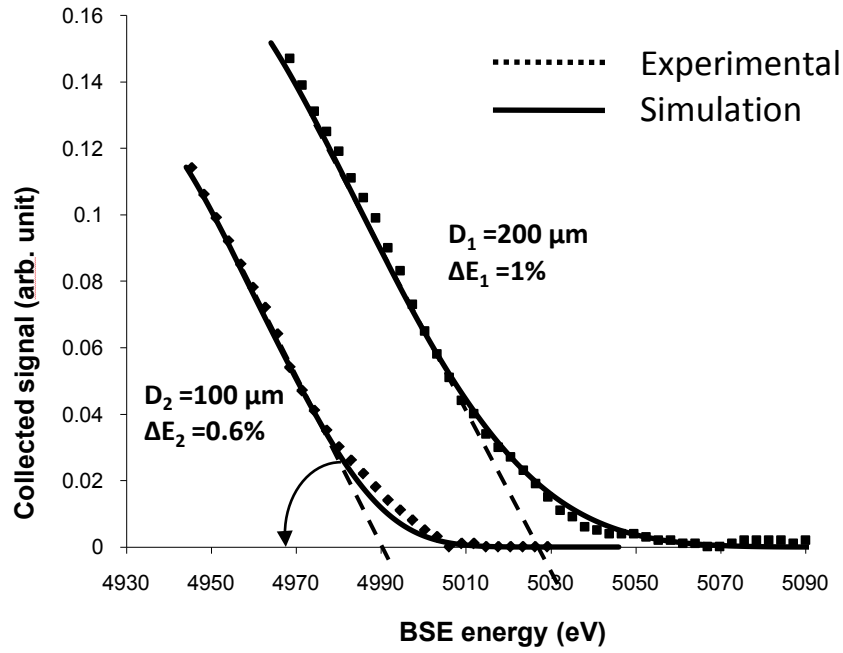
Fig. 3. 27. Experimental and simulated convolution BSE spectra of different energy windows.

The total energy resolution of the spectrometer slit has two components (neglecting the chromatic aberration of the primary beam) approximately described by

$$\Delta E^2 = \Delta E_A^2 + \Delta E_S^2 \qquad (3.5)$$

Where ΔE_A is the resolution due to the finite aperture size and ΔE_S is the resolution due to the spectrometer spherical aberration. Since dispersion in the detection plane is approximately linear, the energy resolution limited by finite aperture size will naturally have a linear dependence on the aperture width, producing ΔE_{A1} for the first aperture (200 μm) and ΔE_{A2} for the second aperture (100 μm), where it can be assumed that $\Delta E_{A2} = 0.5\Delta E_{A1}$, resulting in the two following equations

$$\Delta E_1^2 = \Delta E_{A1}^2 + \Delta E_S^2 \qquad (3.6)$$

$$\Delta E_2^2 = \frac{\Delta E_{A1}^2}{4} + \Delta E_S^2 \qquad (3.7)$$

Solving the two above equations (3.6) and (3.7) gives an estimated spectrometer

101

resolution (limited by spherical aberration) of $\Delta E_S = 0.38\%$. This value is slightly bigger than the simulated resolution of 0.32% for an angular spread of ±8º.

One reason for the slightly bigger experimental value may come from misplacement of the exit slit, ideally, an electronic means of varying the position of the exit focal point needs to be found in order to optimize the analyzer's performance. However, this initial result provides experimental confirmation of the superior (second-order focusing) optical properties predicted for the spectrometer, as compared to previous toroidal spectrometers.

3.4   Proposals to improve the energy resolution of the second-order focusing spectrometer.

Lenses are often used to project incident scattered electrons into the entrance of energy analyzers. The hemispherical analyzer normally utilizes a column of rotationally symmetric lenses [3.20], whereas toroidal analyzers use cylindrical slit lenses and conical slit lenses [3.12]. These kinds of lenses often have a strong focusing action, and provide the possibility of retarding electrons down to a smaller pass energy. In the following section, a pre-collimating lens is proposed as an entrance lens to improve performance of the toroidal spectrometer. This pre-collimating lens is only weakly focusing, and uses an acceleration electric field to minimize the effect of spherical aberration. It collimates wide solid emission angles of the electron beam to smaller input angles entering the analyzer to improve the energy resolution for a given entrance angular spread by an order of magnitude (up to 0.02% for a ± 6º entrance angular spread).

3.4.1 Incorporation of an accelerating pre-collimating lens

Fig. 3.28 shows both simulated ray paths of electrons through the toroidal spectrometer with the presence of a pre-collimating lens for an angular spread of $\pm 6°$. These simulations were carried out using Lorentz-2D [3.18]. The spectrometer design is characterized by the same five parameters as described in section 3.1, in which $\phi_1 = -\pi/2.25$, $\phi_2 = 3\pi/4$, $R_2 = 1.57R_1$ and $R_T = 2R_2$, and the deflection plate potentials are normalized to $V_1 = +1V$ and $V_2 = -1V$. No value of R_T is deliberately given here, since the spectrometer's optics does not depend on its absolute size, it can in practice, be scaled up as required for different applications, therefore, only relative dimensions are specified.
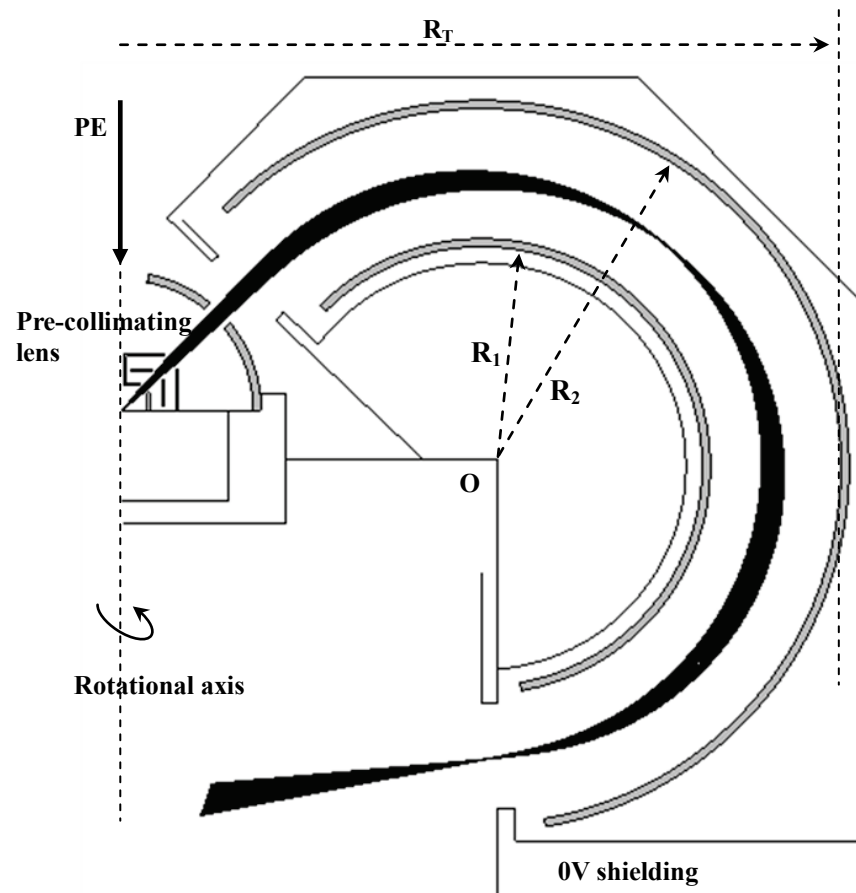
Fig. 3. 28. Simulated ray paths of electrons through the spectrometer at the pass energy for a wide variety of entrance angles. The central ray enters in at 45° and 21 trajectories are plot over uniform steps for an input angular spread varying from -6° to +6°.

The pre-collimating lens used in this design is a three-element annular slit lens, in which the outer electrodes are grounded and the two middle electrodes are biased positively at the potentials V_{L1} and V_{L2} as shown in Fig. 3.29. The lens radius is denoted by R_L. An accelerating lens of this type has relatively low spherical aberration. Figure 3.29 also shows the simulated electrostatic equipotential distribution of the pre-collimating lens and direct ray tracing of electrons emitted from the specimen as they travel through the lens, 14 equipotential lines of uniform steps and 21 electrons with emission angles between 39° and 51° are used (central ray at 45°). The lens bias voltages were chosen to be $V_{L1}=V_{L2} = E_P$, where E_P is the pass energy through the toroidal spectrometer. The collimating action of the lens on the scattered electron beam is evident from the simulated ray paths. This collimating action reduces the angular spread of scattered electrons before they enter the spectrometer. Hence, scattered electrons travel closer to the spectrometer's central region as depicted by in Fig. 3.28, thereby improving the energy resolution (incurring less spherical aberration). These results can be compared to the original toroidal spectrometer design without the pre-collimating lens in section 3.1, where simulated rays at an emission angular spread of $\pm 6^o$ travel much closer to the deflection plates inside the spectrometer as depicted in Fig. 3.4, producing larger spherical aberrations at the detector plane.
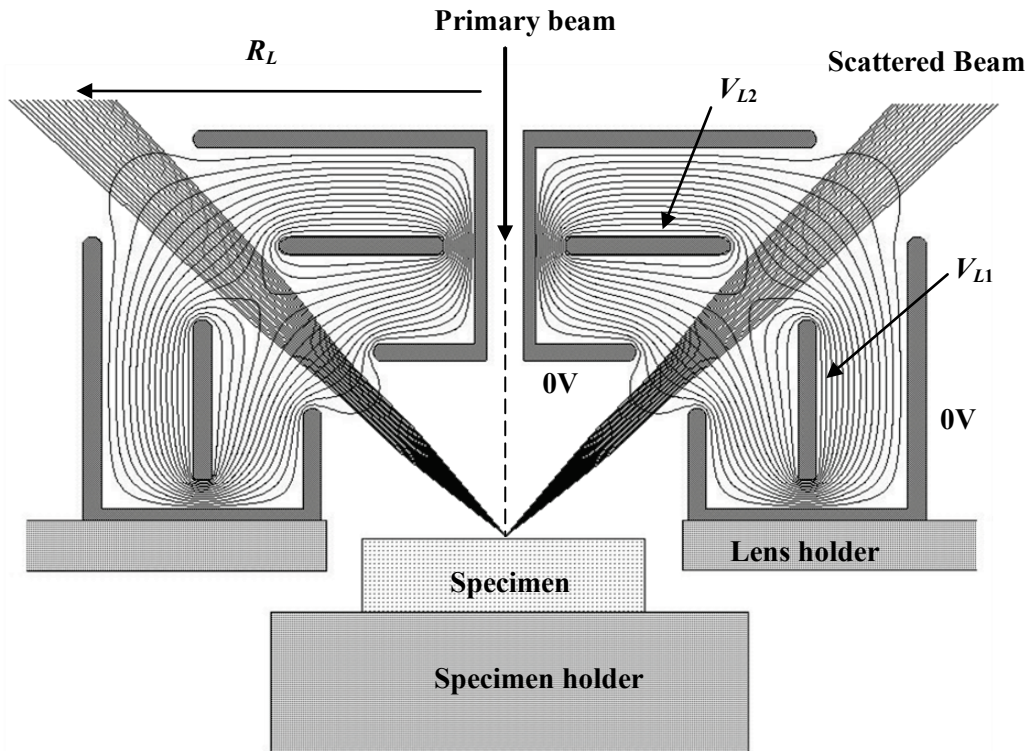
Fig. 3. 29. Equipotential lines from a numerically solved field distribution for the pre-focusing lens. 14 equipotential intervals are taken between 0 V to 2.293 V ($V_{L1}=V_{L2}=2.293V=E_P$) and 21 electrons of 2.293 eV leave the specimen with an emission angular spread of $\pm6°$.

The energy resolution of the setup depends on the relative sizes of the pre-collimating lens and the toroidal spectrometer. This is because the focusing effect of the pre-collimating lens has a certain spherical aberration, resulting in a virtual source size for electrons entering the spectrometer (instead of a point source at the origin). This virtual source is projected on to the spectrometer detector (image) plane. This means that the final spot-size of the scattered electron beam is a combination of the size of both the spherical aberrations of the spectrometer and the pre-collimating lens. Since the aberration width produced by the pre-collimating lens is proportional to its size, a well known property of the electrostatic lens, the final energy resolution is predicted to improve by the decreasing of the size of the pre-collimating lens.

Fig. 3.30 shows the dependence of the simulated energy resolution on the relative size of the pre-collimating lens and the spectrometer. The energy resolution is derived from the energy width corresponding to half the final trace-width, at the point where the trace-width is a minimum (not on the Gaussian plane). The lens radius R_L, is normalized to R_T, the spectrometer radius. This graph shows that when the pre-collimating lens radius is smaller than 0.09 times the spectrometer radius, the energy resolution can be improved. Beyond this size, the spherical aberration of the lens is too large, degrading the final trace-width, causing it to be larger than the one obtained by the spectrometer alone. This result predicts that the energy resolution of the spectrometer can be enhanced by using a relatively small pre-collimating lens at the entrance of the spectrometer. The predicted energy resolution obviously improves as the relative size of the pre-collimating lens decreases. In the next section, a small entrance lens is simulated, showing that the energy resolution can be improved by an order of magnitude.
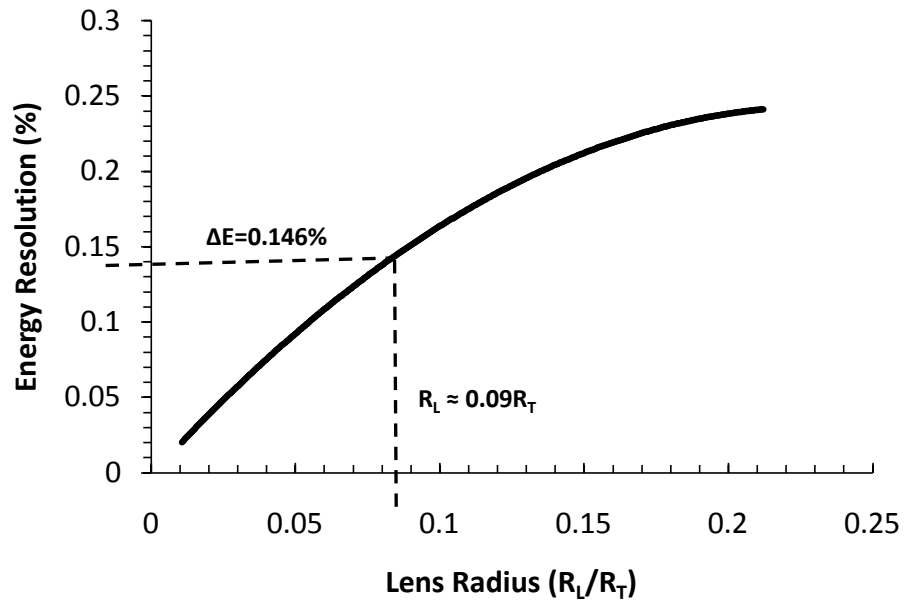
Fig. 3. 30. The dependence of energy resolution on relative size of the pre-collimating lens and the toroidal spectrometer.

3.4.2 A small pre-collimation lens high energy resolution spectrometer

As discussed, the pre-collimation lens dimensions can be scaled down (relative to the toroidal spectrometer size) in order to reduce its spherical aberration contributions to the final spot size. Consider the case where $R_T/R_L = 180$. In order to achieve the best energy resolution results, it was found that the lens central voltages V_{L1} and V_{L2} need to be slightly different from one another. If a parameter γ defines the ratio between the two excitation voltages V_{L1} and V_{L2}, then the best energy resolution is achieved when $\gamma = 0.94$. Fig. 3.31 shows the dependence of both simulated energy resolutions at the Gaussian focal plane and at the least confusion focal plane, on the excitation voltages of the pre-collimating lens. The energy resolution reaches a minimum value at a certain excitation voltage, which occurs when the voltage V_{L1} is around $1.22E_P$. The energy resolution is limited by the toroidal spectrometer spherical aberration when the excitation voltage of the lens is smaller than this value, and limited by the pre-collimating lens spherical aberration when it is higher than this value.
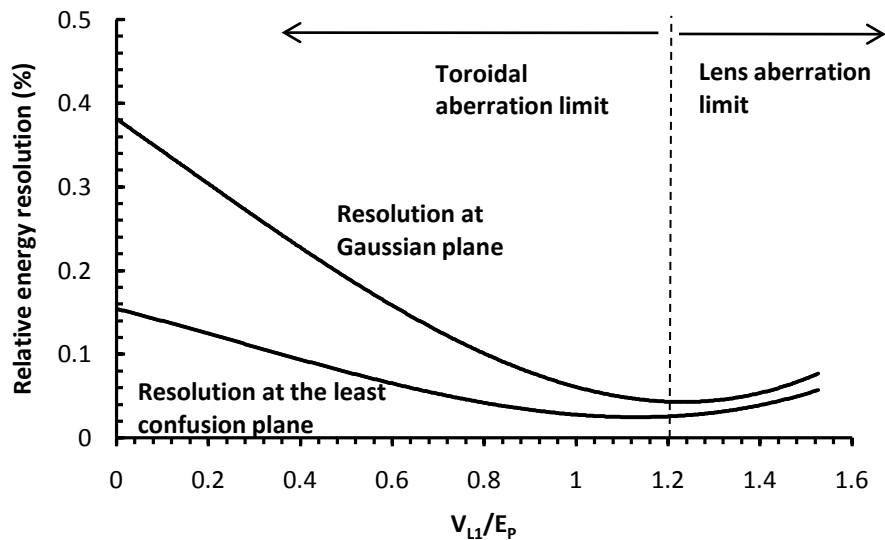
Fig. 3. 31. Dependence of the base and the best energy resolutions on the excitations of the pre-focusing lens, parameter γ is chosen to be 0.94.

By choosing the parameter $\gamma = 0.94$ and excitation voltage $V_{L1} = 1.22E_P$, the best simulated relative energy resolution was found to be 0.021% for an input angular spread of ±6º, corresponding to a transmittance of 20% (assuming a polar angle cosine distribution), which is an order of magnitude better than that of the second-order focusing toroidal spectrometer without the pre-collimating lens. For input angles of ±10º, corresponding to a transmittance of 34%, the best relative energy resolution is simulated to be 0.088%. The simulated energy resolution improvement of the spectrometer by use of the pre-focusing lens can be visually demonstrated by examining focal points at the detection plane, as shown in Fig. 3.32, in which three electron beams of different energies with an input angular spread of ±6º were plot. The difference in energy between these electron beams is 0.05% of the pass energy. It is clear that these three electron beams are well separated, visually confirming that the spectrometer design has a relative energy resolution well below 0.05%.

The predicted high energy resolution for the small pre-collimation lens/toroidal spectrometer is comparable to the energy resolution of the spheroidal spectrometer recently proposed by Cubric for the same transmittance [3.27]. For the second-order focusing cylindrical mirror analyzer (CMA) commonly used in Auger spectroscopy, the best simulated relative energy resolution is around 0.155% for ±6º entrance angles [3.14], therefore, the recent toroidal analyzer with the pre-collimating lens design is expected to be an order of magnitude better than the CMA for the same entrance angular spread. Hemispherical deflection analyzers with retardation of the pass energy can provide an energy resolution of 0.05% but have much lower transmittance (<0.5%). [3.20]
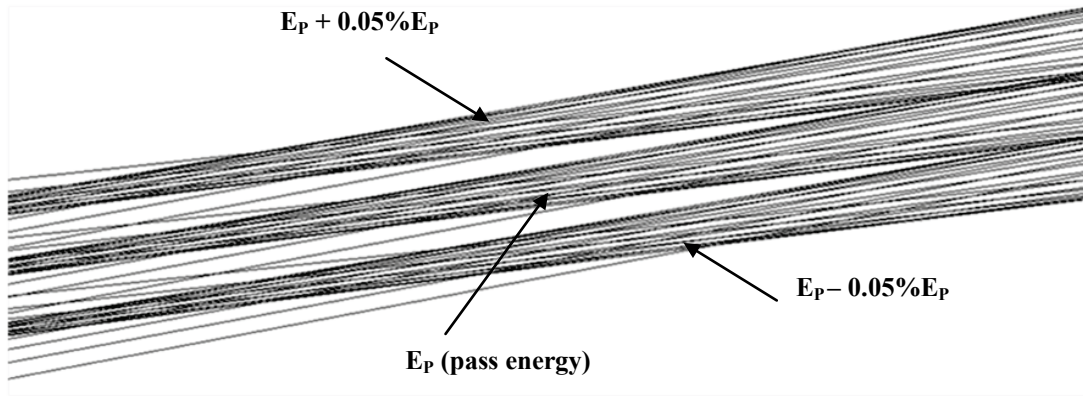
Fig. 3. 32. Simulated trajectories around the output focal plane for 3 emission energies $E_P - 0.05\%E_P$, E_P and $E_P + 0.05\%E_P$, where E_p is the pass energy, and the input angles range from -6º to 6º around the central ray in uniform steps.

Simulation results predict that the addition of the pre-collimating lens will also improve the toroidal spectrometer parallel energy detection mode of operation. A comparison of ray paths around the detection plane with different energies and angles for the toroidal spectrometer with and without the pre-collimating lens is shown in Fig. 3.33. There are eleven different energies uniformly spread over an energy interval ranging from 95% to 105 % of the pass energy (indicated by E_p in the diagram). For each energy, there are eleven trajectories whose input angles are uniformly spread between -6° to +6° around the central entrance angle (45º). Fig. 3.33a shows trajectory ray paths for the toroidal spectrometer only, while Fig. 3.33b shows trajectory ray paths produced with the addition of the small pre-collimating lens. The improvement of energy resolution is clearly maintained across the entire energy pass band range.
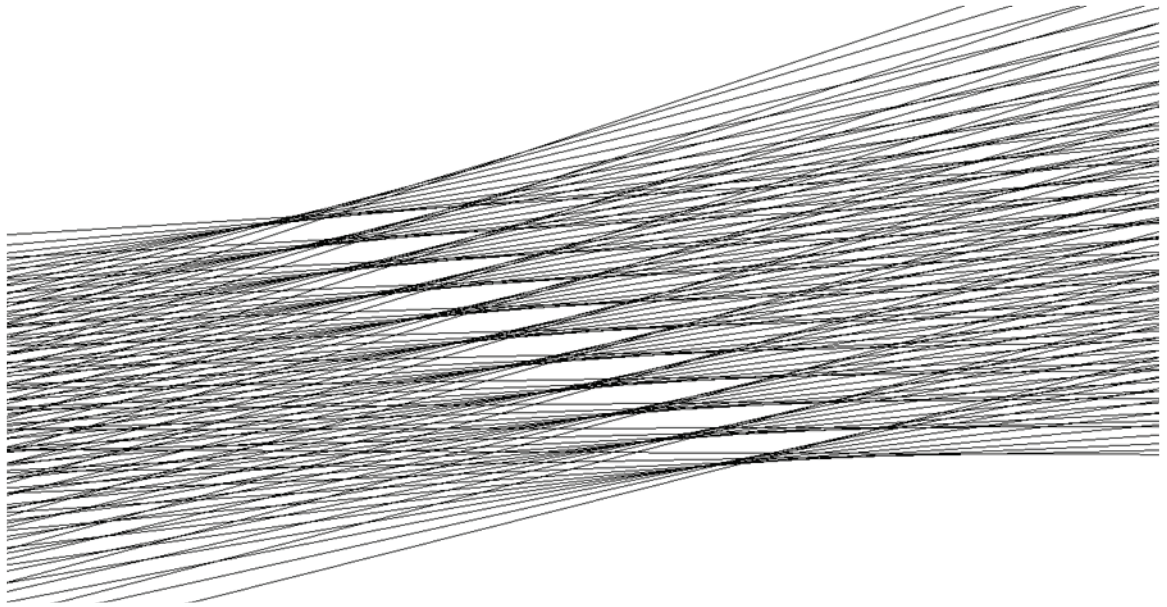
(a)
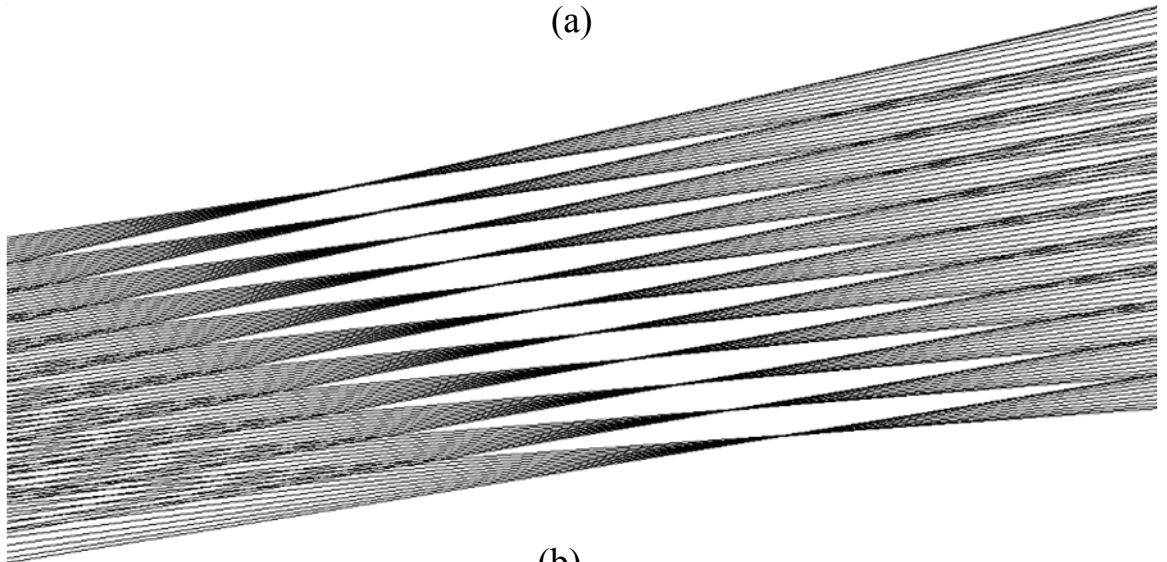
(b)

Fig. 3. 33. Simulated trajectories around the output focal plane for 11 emission energies ranging from 95% to 105% of the pass energy and 11 input angles from -6º to 6º around the central ray in uniform steps: (a) without the pre-collimating lens; (b) with the pre-collimating lens
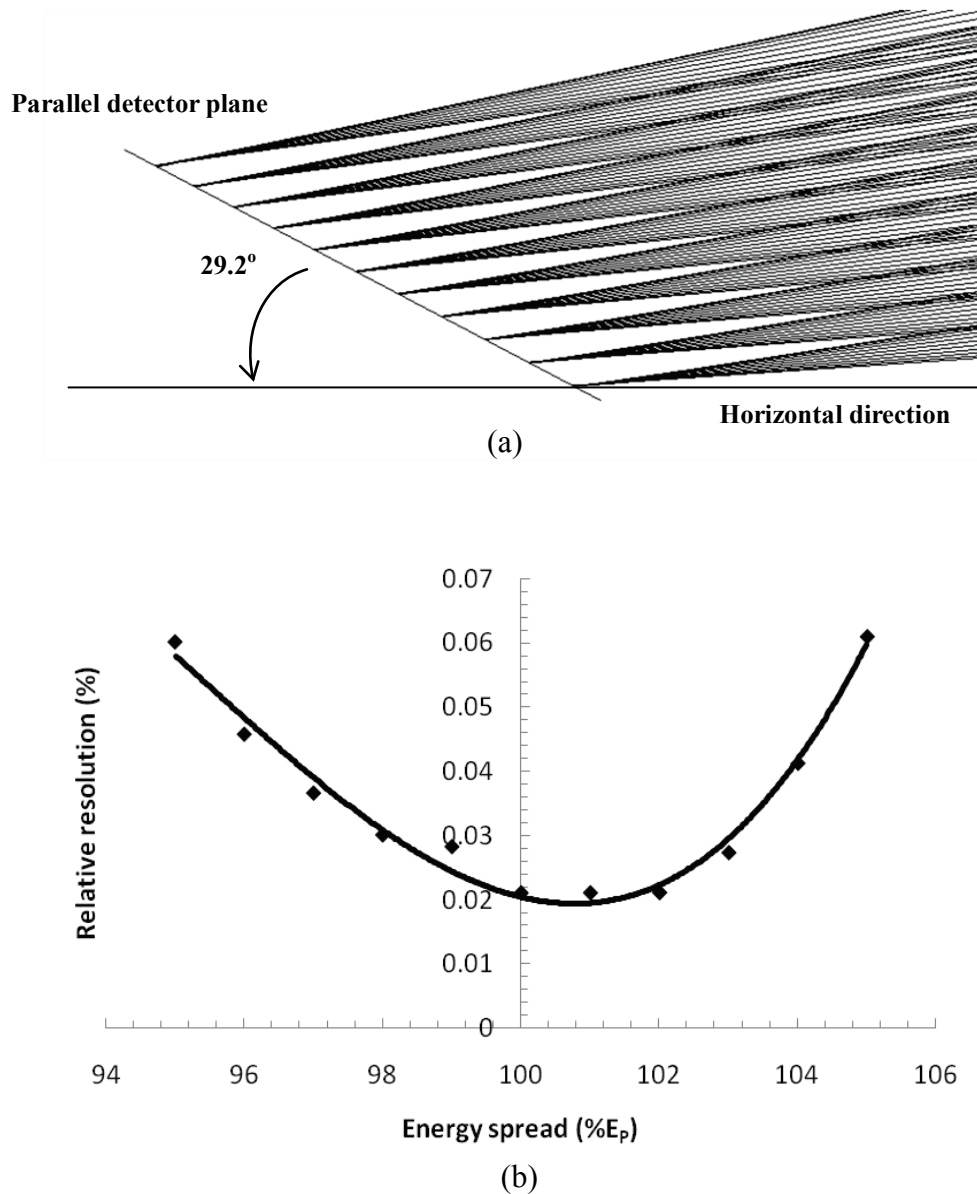
Fig. 3. 34. Simulated energy band (a) Simulated trajectories shown in Fig. 32b along a detection plane at 29.2° with respect to horizontal direction; (b) Simulated energy resolution along the detection plane, across the energy band spanning 95% to 105% of the pass energy

Fig. 3.34a shows the case where the detector plane is orientated to be 29.2° with respect to the horizontal axis, the optimum orientation angle of the detection plane. The energy resolution (half-width) along this detection plane was calculated, and normalized to its value at the centre of the band and plot as a function of energy, the result is shown in Fig. 3.34b. The energy resolution rises by less than a factor of three

for an energy pass band defined from 95% to 105% of the central pass energy. This indicates that the degradation of the energy resolution is small over a relatively wide energy range (~10%), making it possible to operate the spectrometer in the parallel energy mode of detection with high energy resolution.

3.5   Conclusions

A fully 2π radian collection second-order focusing toroidal spectrometer design has been investigated. A range of different geometrical designs were investigated, the best of which have the following simulated predictions: second-order focusing with an expected energy resolution of 0.146% for acceptance angles between $\pm6^\circ$, comparable to the theoretically best resolution-transmittance of the CMA; parallel energy acquisition where the increase in energy resolution with respect to the band centre rises by less than a factor of 2 for energies that lie within $\pm4\%$ of the pass energy; a maximum input angular spread of $\pm10^\circ$ and a maximum parallel energy band-width of $\pm15\%$ (30% total) of the pass energy; retarding/accelerating field mode of operation without the need to incorporate auxiliary lenses; and depending on the precise application, no working distance limitations.

For parallel energy detection, the detection plane lies on the surface of a shallow cone whose slanting side makes an angle of around 26.4° with respect to the horizontal. A multi-channel array of flat strip detectors in the azimuthal direction is not expected to significantly degrade the energy resolution, typically less than 5% for 40 such detectors. For low energy electrons, typically less than 50 eV, electrons can be mirrored on to a flat plate detector located below the specimen after they pass through the spectrometer. The energy resolution is only marginally degraded by doing this,

and predicted to be 0.196% at the centre energy pass band (for an input angular spread of ±6°).

A prototype of the toroidal electron spectrometer based upon simulation design has been made, functioning as a SEM attachment. It shows that the spectrometer has low noise, in the mV range, useful for voltage contrast applications. A negative biasing specimen technique was also investigated and shown to enhance the output signal intensity by one to two orders of magnitude, creating a more convenient way of making open-loop specimen voltage contrast measurements. The technique also improves the SNR, making it possible to detect μV voltage shifts in the SE spectra. BSE spectra was also acquired, demonstrating that is is possible to distinguish close atomic number materials by a SNR of over 20. This result suggests that a SEM spectrometer attachment of this kind may be useful for quantitatively mapping elemental contrast on the nano-scale.

A technique to estimate the energy resolution of the spectrometer has also been proposed. This technique utilizes the measured BSE falling edge as a convolution of the intrinsic BSE spectrum and a Gaussian spectrometer/slit response. The energy resolution measured experimentally by this method is 0.38% for an angular spread of ±8°, which is comparable to the simulation prediction of 0.32%. This agreement provides initial confirmation of the spectrometer's superior second-order focusing properties, as compared with previous first order focusing toroidal spectrometer.

A pre-collimating lens has also been proposed for the second-order focusing spectrometer. Simulation results predict that the spectrometer energy resolution-

transmittance performance can be greatly improved via the use of the lens, predicting a relative energy resolution of 0.021% and 0.088% for emission angular spreads of $\pm$ 6º and $\pm$ 10º respectively, corresponding to a transmittance of around 20% and 34%, an order of magnitude better than that of the second-order focusing CMA and a factor of 50 times better than previous first-order focusing toroidal spectrometers.

References

3.1   E. I. Rau, and V. N. E. Robinson, "An annular toroidal backscattered electron energy analyser for use in scanning electron microscopy", Scanning, 18 (1996) 556-561.

3.2   E. I. Rau, and H. Niedrig, "Information depth and spatial resolution in BSE microtomography in SEM", Nucl.Instrum.Meth. B 143, (1998) 523.

3.3   E. I. Rau, A. Khursheed, A. V. Gostev, and M. Osterberg, "Improvements to the design of an electrostatic toroidal backscattered electron spectrometer for the scanning electron microscope", Rev. Sci. Instrum. 73 (2002) 227-229.

3.4   M. Belha, O. Jbara, and S. Fakhfakh, "Quantitative voltage contrast method for electron irradiated insulators in SEM", J. Phys. D: Appl. Phys. 41 (2008) 175304

3.5   H. A. Engelhardt, A. Zartner, and D. Menzel, H. Liebl, "Novel charged particle analyzer for momentum determination in the multichanneling mode: I. Design aspects and electronlion optical properties", Rev. Sci. Instrum. 52 1981) 835.

3.6   J. D. Riley, R. C. G. Leckey, "A toroidal angle-resolving electron spectrometer for surface studies", Appl. Surfac. Sci. 22-23 (1985) 196.

3.7   L. Broekman, A. Tadich, E. Huwald, J. Riley, R. Leckey, T. Seyller, K. Emtsev, L. Ley, "First results from a second generation toroidal electron spectrometer", J. Electron Spectrosc. Relat. Phenom. 144–147 (2005) 1001.

3.8   A. Duguet, A. Lahmam-Bennani, M. Lecas, and B. El Marji, "A multidetection, multicoincidence spectrometer for (e,2e) and (e,3e) electron impact ionization measurements",Rev. Sci. Instrum., 69 (1998) 3524

3.9   R. W. van Boeyen and J. F. Williams, "Multidetection .e,2e. electron spectrometer", Rev. Sci. Instrum 76 (2005) 063303.

3.10 J. Lower, R. Panajotović, S. Bellm, and E. Weigold, "An improved double-toroidal spectrometer for gas phase (e,2e) studies", Rev. Sci. Instrum 78 (2007) 111301.

3.11 C. Miron, M. Simon, N. Leclercq, and P. Morin' "New high luminosity ''double toroidal'' electron spectrometer", Rev. Sci. Instrum. 68 (1997) 3728.

3.12 M.R.F. Siggel-King, R. Lindsay, F.M. Quinn, J. Pearson, G. Fraser, G. Thornton, "TEARES: a toroidal energy- and angle-resolved electron spectrometer", J. Electron Spectrosc. Relat. Phenom. 137–140 (2004)

3.13 M.R.F. Siggel-King, R. Lindsay, T.J. Reddish, D.P. Seccombec, F.M. Quinn, "TEARES: toroidal energy- and angle-resolving electron spectrometer—results, recent modifications and instrument performance", J. Electron Spectrosc. Relat. Phenom. 144-147 (2005) 1005.

3.14 H. Z. Sar-El, "Criterion for Comparing Analyzers", Rev. of Sci. Instrum., 41, No. 4, 561-564 (1970).

3.15 H. Hafner, J. A. Simpson, and C. E. Kuyatt, "Comparison of the Spherical Deflector and the Cylindrical Mirror Analyzers", Rev. Sci. Instrum, 39 (1968) 33.

3.16 A. Khursheed, "A Second-Order Focusing Toroidal Spectrometer", Proceedings of 11st Seminar on Recent Trends in charged particle optics and Surface Physics Instrumentation, Brno Czech Republic (2008) 57-58

3.17 A. Khursheed, " The KEOS", Electrical and computer engineering department, National University of Singapore, Singapore.

3.18 Lorentz - 2EM, Integrated Engineering Software Inc, Canada.

3.19 A. Khursheed, The Finite Element Method in Charged Particle Optics (Kluwer Aacademic Press, Boston, USA, (1999) Chapter 11.

3.20 E. P. Benis, and T. J. M. Zouros, "The hemispherical deflector analyser revisited II. Electron-optical properties", J. Electron. Spectrosc. Relat. Phenom, 163, 28 (2008).

3.21 M. Kienle and E. Plies," An off-axis multi-channel analyzer for secondary electrons", Nucl. Instrum. And Method. in Res. A 519, (2004) 325

3.22 P. Kazemian, S. A. Mentink, C. Rodenburg, and C. J. Humphreys, "High resolution quantitative two-dimensional dopant mapping using energy-filtered secondary electron imaging", J. Appl. Phys. 100 (2006) 054901.

3.23 D. C. Joy, Monte Carlo Modeling for Electron Microscopy and Microanalysis (Oxford University Press, New York, 1995), p. 25.

3.24 J. Stephen, B. J. Smith, D. C. Marshall and E. M. Wittam, "Applications of a Semiconductor backscattered electron detector in a scanning electron microscope", J. Phys E. 8, 607 (1975).

3.25 M. D. Ball, D. G. McCartney, "The measurement of atomic number and composition in SEM using backscattered electrons", J. Micro. 124, 57 (1981).

3.26 N. Rosenberg, C. Z. Jiang, P. Morin, "Monte Carlo simulations of coaxial backscattered electrons in SEM", Ultralmicroscopy, 76, (1999) 97.

3.27 C. Z. Jiang, P. Morin, N. Rosenberg, "A new type of scanning electron microscope using the coaxial backscattered electrons", Micron 33, 69 (2002).

Chapter 4: A Radial Mirror Analyzer for the SEM

4.1   Introduction

In the previous chapter, a toroidal energy spectrometer with second-order focusing was developed as an add-on attachment for conventional SEMs. Its energy resolution, however, is limited to the same order of the CMA, due to low energy dispersion at its focal plane. The aim of the following work is to design a high energy resolution spectrometer for use inside conventional SEMs, typically to have an energy resolution that is around one order of magnitude better than that of the CMA (for the same entrance angular spread).

In Auger Electron Spectrometry (AES) and X-ray photoelectron spectrometry (XPS) the relatively high energy resolution capability of hemispherical deflector analyzers (HDAs), around 0.05%, comes at the price of low transmission, typically less 0.15% [4.1]. On the other hand, the better transmission of cylindrical mirror analyzers (CMAs), of say 15%, comes at the price of a poorer minimum energy resolution, which typically lies between 0.2 – 0.5% [4.2]. There is an obvious need for energy spectrometers that can achieve both high transmittance (> 15%) and high energy resolution (< 0.05%) at the same time.

There have been a few high performance spectrometer designs (high energy resolution and high transmission) for ASE and XPS. Siegbahn et al. described a class of electron energy analyzers having an axially symmetric field structure, similar to that of the CMA, but differing from the latter in having a curved inner concentric plate, and a conical outer plate [4.3]. This analyzer provides axis-to-axis second-order focusing, similar to the CMA. Its third–order spherical aberration, however, is several times

smaller than that of the CMA for the same base length. This allows a noticeable increase in the angular acceptance of the analyzer for a given energy resolution, or alternatively, increased energy resolution for fixed entrance angular spread. The maximum energy resolution of this analyzer was reported to be 0.05% for an acceptance angular spread of about ±6° corresponding to a transmission around 15%. The energy resolution of a double pass structure using this analyzer design is even better for the same transmission.

Belov and Yavor reported a second-order focusing toroidal mirror analyzer (TMA) that is also an extension of the CMA design [4.4]. The TMA is rotational symmetric and has an inner concentric plate like the CMA, but its outer concentric plate is curved, therefore toroidal in shape. For the case where its focal plane lies on the surface of the inner electrode (require a ring detector), the final spot size is limited by fourth-order aberration (third-order focusing). In many modes of operation, this analyzer has energy resolutions much better than the CMA, typically less than 0.05% for an angular spread of ±8°.

Another high resolution high transmission energy analyzer design was also reported by Belov and Yavor [4.5]. They proposed an axis-to-ring rotational symmetric mirror analyzer design followed by a hemispherical energy analyzer, having 2π azimuthal angular collection. The energy resolution of this design was reported to be 0.07% for an angular spread of ±11°.

A recent high energy resolution high transmission electron spectrometer, named a spheroid energy analyzer (SEA), was described by Cubric [4.6-4.7]. A schematic

diagram of a SEA is shown in Fig. 4.1. The inner and outer cylindrically symmetric electrodes of the SEA are created by two spheroids. The inner electrode is grounded while the outer electrode's potential is ramped to acquire the electron energy spectrum. The energy resolution of the SEA is measured to be 0.05% for an entrance angular spread of ±8° in the polar direction. This design has been recently commercialized by Shimadzu Corporation.
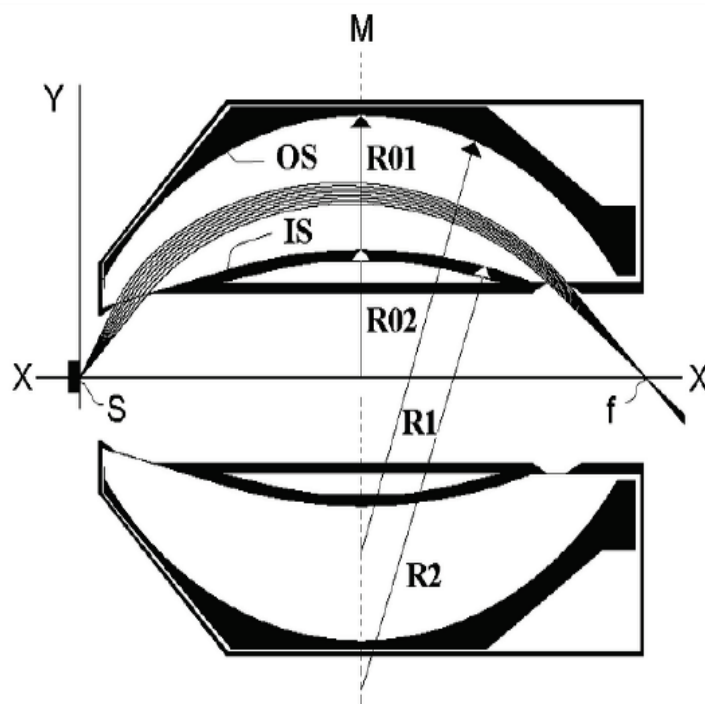
Fig. 4. 1. Schematic diagram of a SEA [4.7]

All of the previous high performance energy analyzer designs just described have the common feature of being variations of the CMA or HDA design. Most of them are based upon using curved/conical concentric inner/outer plates. Moreover, all of them were designed for ASE or XPS, and not for the SEM. They cannot be used as add-on attachments inside a SEM chamber, and require a dedicated electron beam column to be integrated between their source and detector plane.

Apart from high energy resolution, another desirable feature for energy analyzers is to have parallel energy acquisition, where the output signal at different energies can be obtained simultaneously, greatly speeding up data-acquisition times. Although both the CMA and HDA function sequentially, the HDA can operate in a partial parallel mode of operation for high energy resolution (>0.05%), where the output energy bandwidth is typically around 3% to 5% of the central-band energy [4.1]. Widening this output bandwidth further is an important area of spectrometer development. The toroidal spectrometer design reported in Chapter 3 has a parallel mode of operation, however, its focal plane lies on a conical surface detector. Although an array of straight plane detectors in the azimuthal direction can be used to overcome this inconvenience, a flat detector plane is preferable and much simpler to achieve in practice.

The new energy analyzer proposed in this chapter is rotational symmetric and has a high predicted performance (energy resolution of around 0.05% for an angular spread of ±8º), and has the capability of parallel energy acquisition with a bandwidth of 15% on a flat-plane detector. It is also suitable for use as an attachment inside the specimen chambers of scanning electron/ion microscopes. The analyzer is designed to fit around a conical shaped objective lens pole-piece/electrode, allowing for a relatively short minimum working distance, 5 mm or less. The design approach taken in this chapter is essentially a simulation one, where all field distributions and electron trajectory ray paths were simulated using Lorentz-2EM program [4.8].

4.2　The radial mirror analyzer (RMA) design for SEMs

4.2.1　Simulation design

The present energy analyzer design is based upon modifying the well-known fountain spectrometer [4.9]. The main problem preventing the use of the fountain spectrometer inside a scanning electron/ion microscope is that there is no central hole through which the primary electron/ion beam can pass in order to strike the specimen. The introduction of such a central hole will inevitably change its internal field distribution and alter the spectrometer's energy dispersion and focusing properties. The present analyzer design, like the fountain analyzer, has a central rotational axis of symmetry, but unlike the fountain analyzer, it makes provision for a central conical shaped field free region, whose walls have a tilt angle of 45°, in which the pole-pieces/electrodes of an objective lens can fit, and through which the primary beam can pass. The analyzer uses a rotationally symmetric electric field distribution to transport electrons emitted from a central point source in a radial direction on to a ring shaped collection/detection area, as shown in Fig. 4.2.

The name proposed here for the spectrometer, the Radial Mirror Analyzer (RMA), is based upon it using an electric field to mirror and analyze the energies of electrons travelling in a radial direction from a central point source. The outer spectrometer radius, R, is chosen to be 5 cm. Its minimum working distance (W) can be typically of the same size as the objective lens lower pole-piece radius, which can in principle be as small as 5mm, allowing for high spatial resolution. The analyzer is conveniently located above the specimen, much like the conventional backscattered detector. The outer cover is grounded in order to prevent electric field leakage into the SEM specimen chamber. Two grounded electrostatic grids are also used to cover the

entrance and the exit of the spectrometer in order to avoid distortion of the electric field near these regions. In the following simulation model, these grids were approximated to be ideal equipotential planes. Inside the analyzer, under the conical hole, segmented plates are biased at potentials V_1, V_2, and V_3, in order to control how the electric potential falls, suitably adjusted so that the spectrometer has an optimal mirroring/focusing action on incoming electrons. The upper deflection electrode is biased at a voltage V_d.
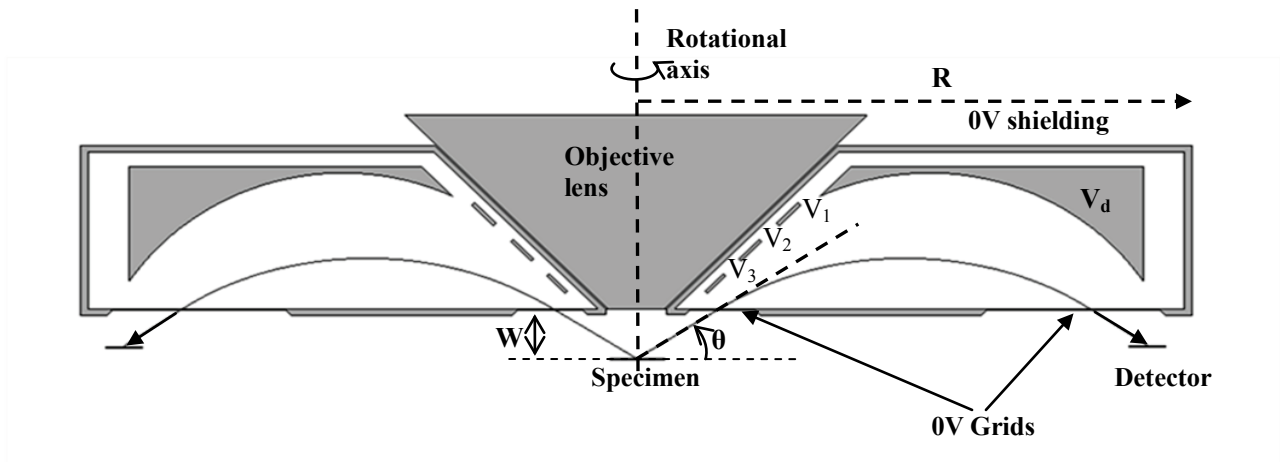
Fig. 4. 2. Schematic diagram of a simulated redesign central filed-free fountain spectrometer for use inside the SEM. The segmented electrodes are biased by V_1, V_2, V_3 and the curvature deflecting electrode is biased at V_d. Parameter W defines the working distance.

Many designs were investigated by varying the upper deflection electrode shape, relative positions of segmented electrodes, electrode biasing potentials, and the entrance angle, θ, in order to minimize the simulated spot size at the detector plane. Conditions for the best simulated energy resolution occur for a central ray entrance angle of $\theta = 32.6°$, $V_1 = V_d$, $V_2 = 0.711V_d$, $V_3 = 0.302V_d$, and a pass energy E_P of $1.75V_d$.
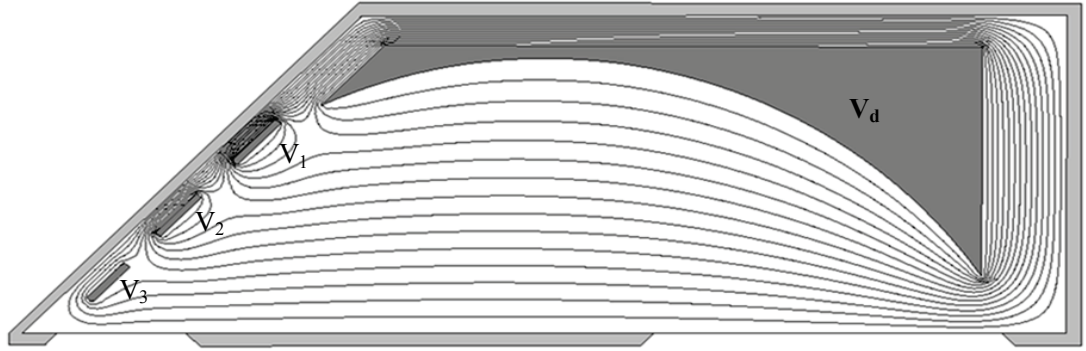
Fig. 4. 3. Equipotential lines from a numerically solved field distribution for the new spectrometer design. 14 equipotential intervals are taken between 0 V to - 0.57V($V_1 =$ V_d, $V_2 = 0.711V_d$, and $V_3 = 0.302V_d$, and $V_d = -0.57V$).

Figure 4.3 shows 14 equipotential lines plot at uniform voltage steps on the simulated potential distribution for these design parameters. The upper deflection electrode voltage is chosen to be $V_d = -0.571V$ (pass energy of 1eV). The equipotential lines inside the spectrometer, especially close to the three segmented electrodes, are clearly not uniform, unlike the equipotential lines inside the conventional fountain spectrometer. Simulation results showed that this non-uniform field distribution near the input of the spectrometer is the most critical parameter for it to achieve high energy resolution, since it reduces the electron beam trace-width at the output of the analyzer. Furthermore, the non-uniform field created by the curvature of the upper deflection electrode close to the exit of the spectrometer is an important design parameter for the analyzer's parallel mode detection characteristics.

4.2.2 Simulated energy resolution-transmittance characteristics

Figure 4.4 shows simulated direct ray paths of scattered electrons with a pass energy $E_P = 1eV$, leaving a point on the rotational axis for an input angular spread of $\pm 6°$ around an entrance angle θ of $32.6°$, 21 trajectories are plot in uniform angular steps.

124

This entrance angle θ is slightly different to that of the conventional second-order of focusing fountain spectrometer, where $\theta = 30^{\circ}$. Spherical aberration characteristics of the spectrometer are obtained by monitoring the beam trace-width at its Gaussian focal plane as a function of input angular spread and is plot in Fig. 4.5a. This graph indicates that the RMA design is characterized by second-order focusing optics, since the trace-width at the output Gaussian focal plane exhibits a third-order dependence with respect to the input angular spread. The third-order variation is however, a little asymmetric, most likely due to the presence of non-uniform field distribution regions, such as the one close to the entrance segmented electrodes and the one below the upper deflection plate at the spectrometer exit. Figure 4.5b depicts the energy dispersion at the output Gaussian focal plane caused by energy spread in the beam, and as expected, it has a linear variation.
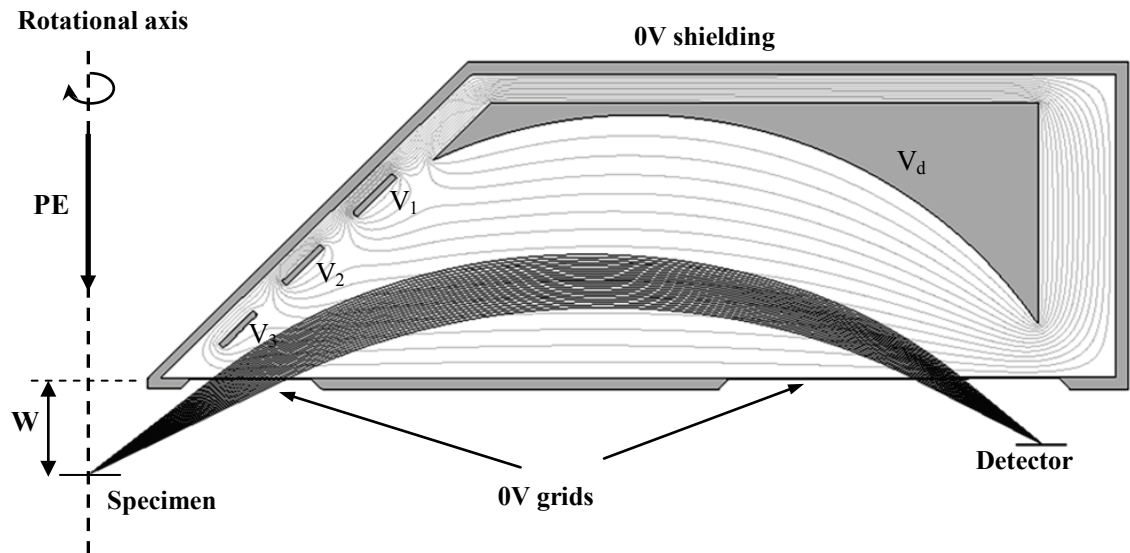
Fig. 4. 4. Simulated ray paths of electrons through the spectrometer at the pass energy for a wide variety of entrance angles. The central ray enters in at 32.6° and 21 trajectories are plot over uniform steps for an input angular spread varying from -6° to 6°.

(a)
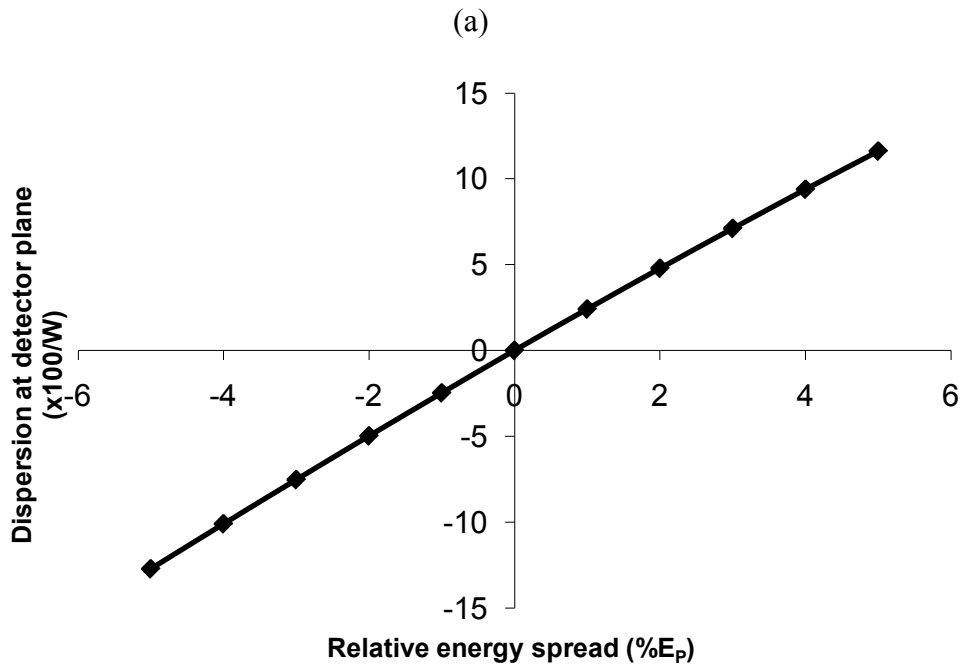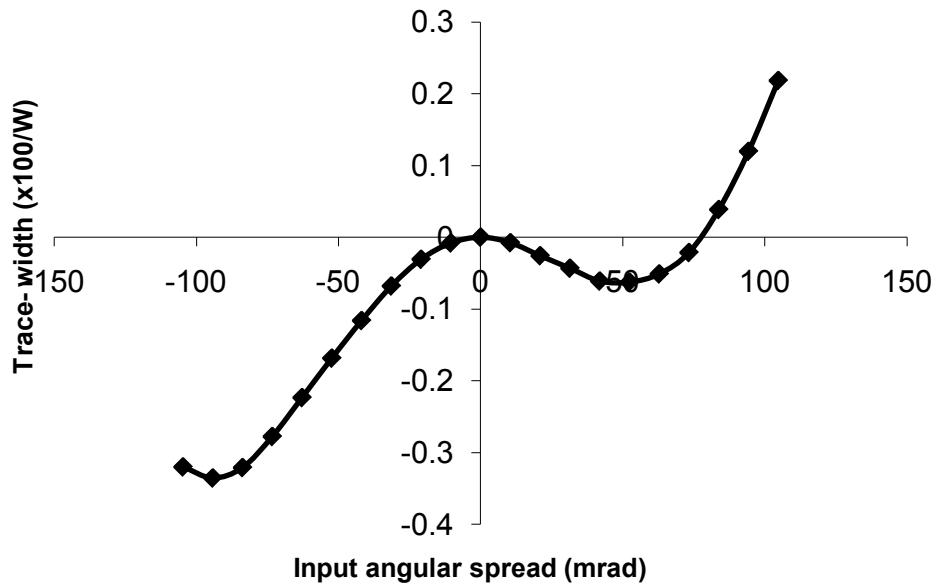
(b)

Fig. 4. 5. Simulated normalized trace width at the output Gaussian focal plane (all the values are normalized to the working distance W): (a) Due to spherical aberration; (b) Due to relative energy spread

The energy resolution of the spectrometer is related to the trace-width created by spherical aberration, compared to the dispersion along the detection plane caused by energy spread. The energy resolution here is calculated from half of the full trace-

width. For input angular spreads of $\pm 6^{\circ}$, the trace width at the Gaussian focal plane and the energy dispersion for an energy difference of 1% are predicted to be 26.9 μm and 122.2 μm respectively. Hence, the half-width relative energy resolution at the Gaussian focal plane is predicted to be 0.11% The transmittance for this angular spread is around 20%, assuming 2π collection in the azimuthal direction and a polar angle cosine distribution of emission. In practice, depending on the transparency of the input/output grids, this transmittance may reduce to around 15%. A well known property of second-order focusing analyzers is that the best energy resolution does not lie at the output Gaussian focal plane, but occurs a small distance before it. For the present RMA design, the best simulated relative energy resolution is simulated to be 0.025% for an input angular spread of $\pm 6^{\circ}$, a factor of 4 times better than the Gaussian plane value.
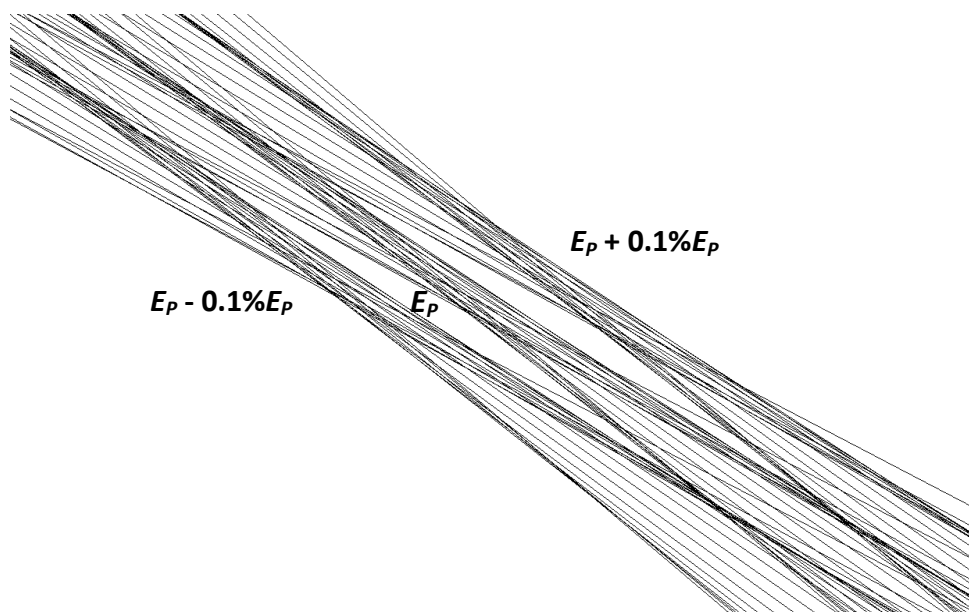
Fig. 4. 6. Simulated trajectories around the output focal plane for 3 emission energies E_P – 0.1%E_P, E_P and E_P + 0.1%E_P, where E_p is the pass energy, and the input angles range from -6° to 6° around the central ray in uniform steps.

This high energy resolution performance is graphically demonstrated in Fig. 4.6, in

which electrons for an input angular spread of $\pm 6^{\circ}$ at the detection plane for three different energies are plot, the energy spread is $\pm 0.1\%$ of the pass energy. Fig. 4.6 shows that the electrons at the detection plane for these energies are well separated and confirms that the best simulated relative energy resolution is around 0.025%. This predicted energy resolution is around an order of magnitude better than that of the CMA for the same entrance angular spread [4.2], and is comparable to the HDA operating in its retardation mode [4.1]. Its performance is also comparable to the recent high performance analyzers proposed by Cubric [4.6].

4.2.3 The parallel energy acquisition mode

The simulation work carried out here predicts that the RMA design has a parallel energy mode of operation, considerably wider than the energy band, about 3%, normally achievable by the HDA in its high energy resolution mode (3%) [4.1]. Fig. 4.7 shows electron trajectory ray paths leaving a point on axis for a range of different emission energies, with no angular dispersion. Sixteen electron trajectories are plot in uniform steps over an energy range spanning 84% to 114% of the pass energy (E_P $=1.75V_d$). The output focal plane, calculated from tracing rays emitted at different angles for each energy, is superimposed on to these rays paths at the spectrometer exit. The spectrometer's output focal plane is not simply a conical surface as it is in the case of the conventional fountain spectrometer, but is a curved surface that can be approximately divided into two separate detection planes. The first detection plane is a conical surface, similar to the one generated by the conventional fountain spectrometer, and is orientated at an angle of 10.2° with respect to the horizontal axis. The second detection plane is a horizontal one, formed by the fact that higher energy electrons travel closer to the non-uniform field distribution region below the upper

deflection electrode at the spectrometer exit, and therefore experience a greater focusing focus than electrons of lower energy. The horizontal part of the detection plane is preferable, since it is easier to make a ring detector than one which lies on a conical surface.
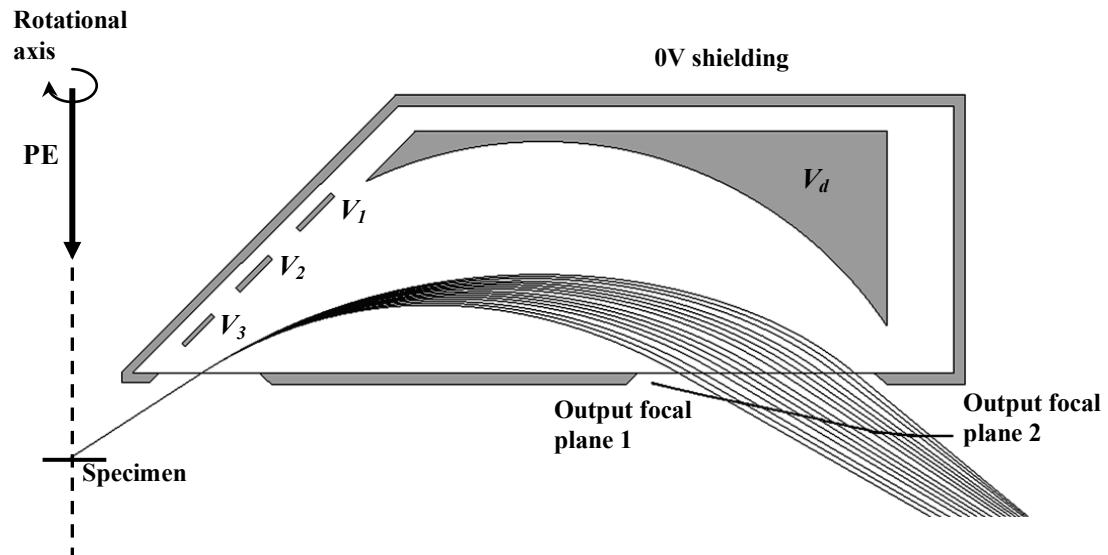
Fig. 4. 7. Simulated zero angle electron trajectories at 16 emission energies spread uniformly from 84% to 114% of the pass energy. The parallel detection plane is marked at the exit of the spectrometer.

The orientation of the conical surface output focal plane shown in Fig. 4.8, 10.2° with respect to the horizontal direction, is selected in order to maximize the width of the output energy band. Fig. 4.8a shows a set of simulated electron ray paths having different emission energies and angles traced from the specimen through the spectrometer collected on the first part of the output focal plane. There are 13 different energies uniformly spread over an energy interval ranging from 84% to 116% (32%) of the central-band energy, E_0. For each energy, there are 13 trajectories whose input angles are uniformly spread between -6° to 6° around the central entrance angle (32.6^o). Fig. 4.8b depicts a magnified diagram of electron trajectories around the conical shaped detection plane shown in Fig. 4.8a.   The simulated energy

resolution of different energies along this detection plane is shown in Fig. 4.9, and lies

well below 0.07% for the whole energy band, a spread of 20% (± 10%) of the central-

band energy. For an energy band of more than 30% (± 15%) of the central-band

energy , the predicted energy resolution drops to around 0.15% at the edge of the

detector.

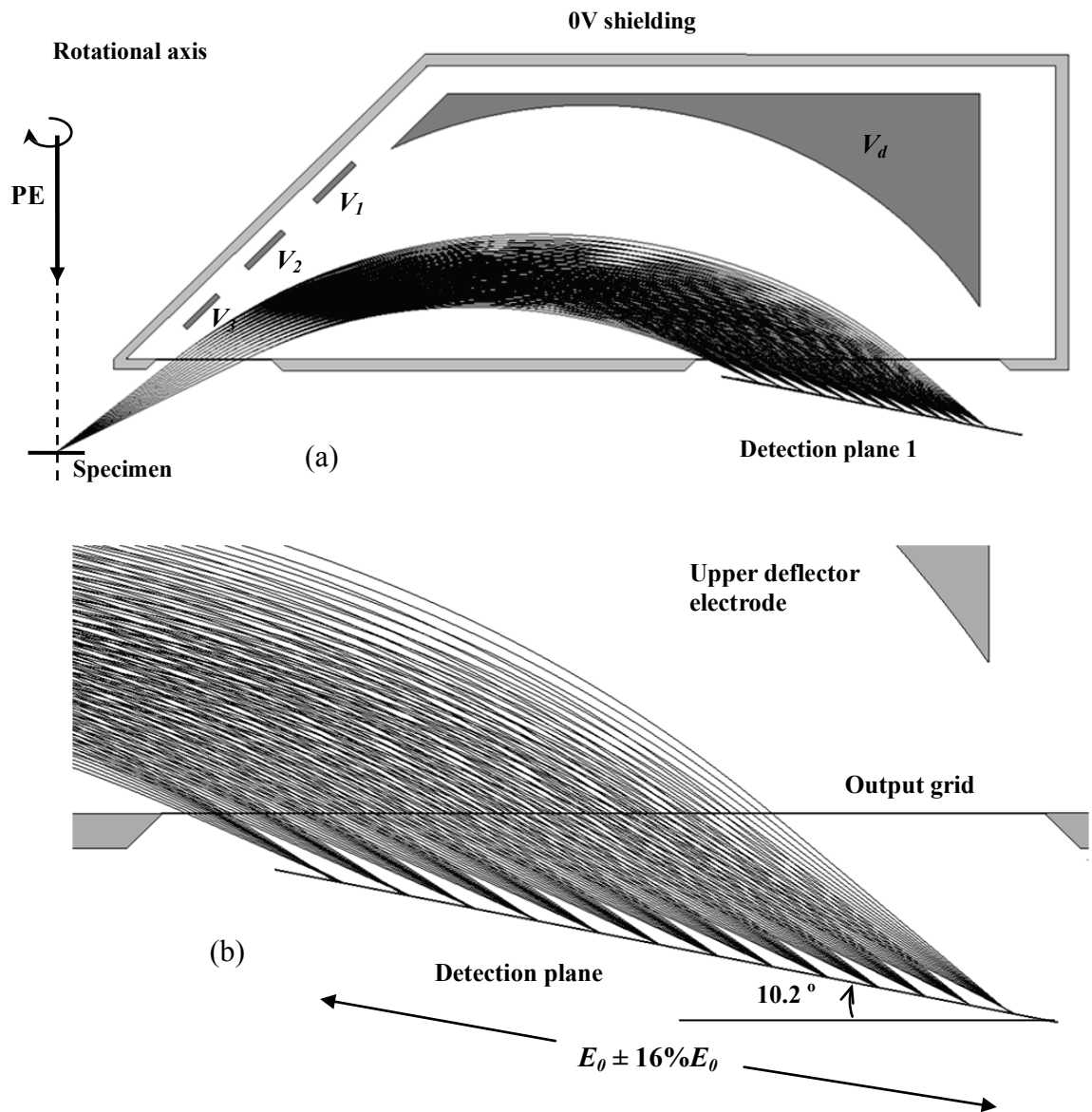**Fig. 4. 8.** Simulated parallel energy acquisition for the detection plane 1: (a) 13 emission energies ranging from 84% to 116% of the central energy and 11 input angles from -6° to 6° around the central ray in uniform steps tracing from the specimen through the spectrometer and to be detected on the detection plane; (b) Magnified trajectories around the detection plane. E_0 defines the central-band energy.

Fig. 4. 9. Simulated energy resolution across the energy band spanning 84% to 114% of the central energy along detection plane 1.

Fig. 4.10a shows simulated ray paths having different emission energies and angles traced on the second part of the output focal plane, the horizontal section. The energy ranges from 92.5% to 107.5% of the central-band energy (15 different energies plot in uniform steps), and each energy has thirteen trajectories corresponding to input angles uniformly spread between -6° and 6° around the centre angle. A magnified view of this diagram around the horizontal detector plane is depicted in Fig. 4.10b. It is clear that the trace-width of the electron beams does not change much within this energy band. The quantitative simulated energy resolution corresponding to this is shown in Fig. 4.11. The energy resolution is predicted to be well below 0.06% for the output energy range of 12% ($\pm$ 6%) of the central-band energy. This output energy range in parallel energy acquisition mode, is around 4 times greater than the typical energy band of the HDA (3%) for same high energy resolution (>0.05%) in its retardation mode [4.1]. The energy resolution distribution along the detection plane is

also much more uniform than in the HDA. This energy resolution is predicted to drop by approximately a factor of two at the edge of the detector when the output energy bandwidth is increased to 15% (±7.5%) of the central-band energy. The parallel detection capability along a horizontal flat plane detector is one of the strong points of the RMA design compared to other high performance energy analyzer designs such as the SEA reported by Cubric [4.6].

Fig. 4. 10. Simulated parallel energy acquisition for the detection plane 2: (a) 16 emission energies ranging from 92.5% to 107.5% of the central energy and 11 input angles from -6° to 6° around the central ray in uniform steps tracing from the specimen through the spectrometer and to be detected on the horizontal detection flat-plane 2; (b) Magnified trajectories around the detection plane. E_0 defines the central band energy.
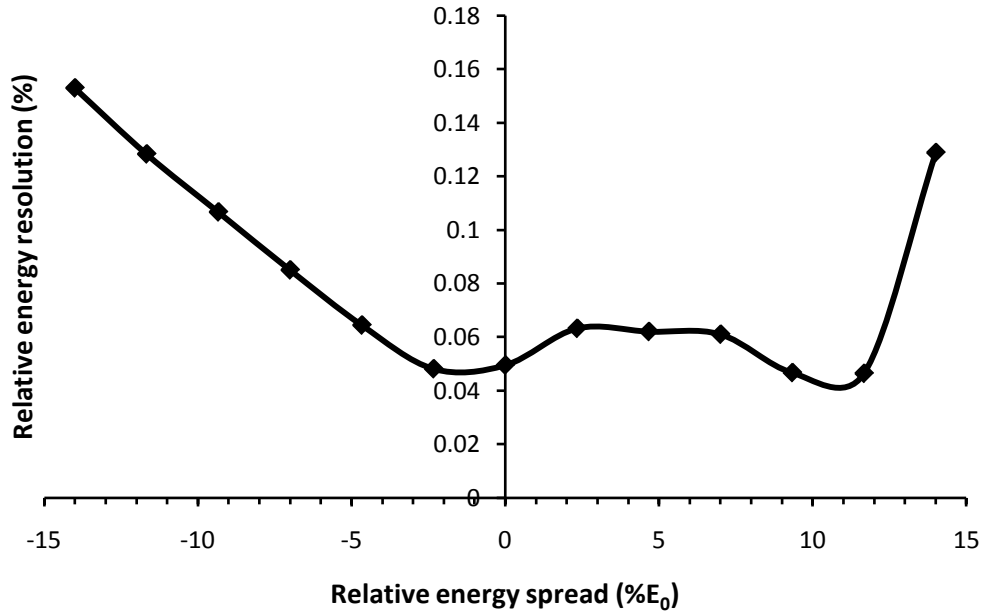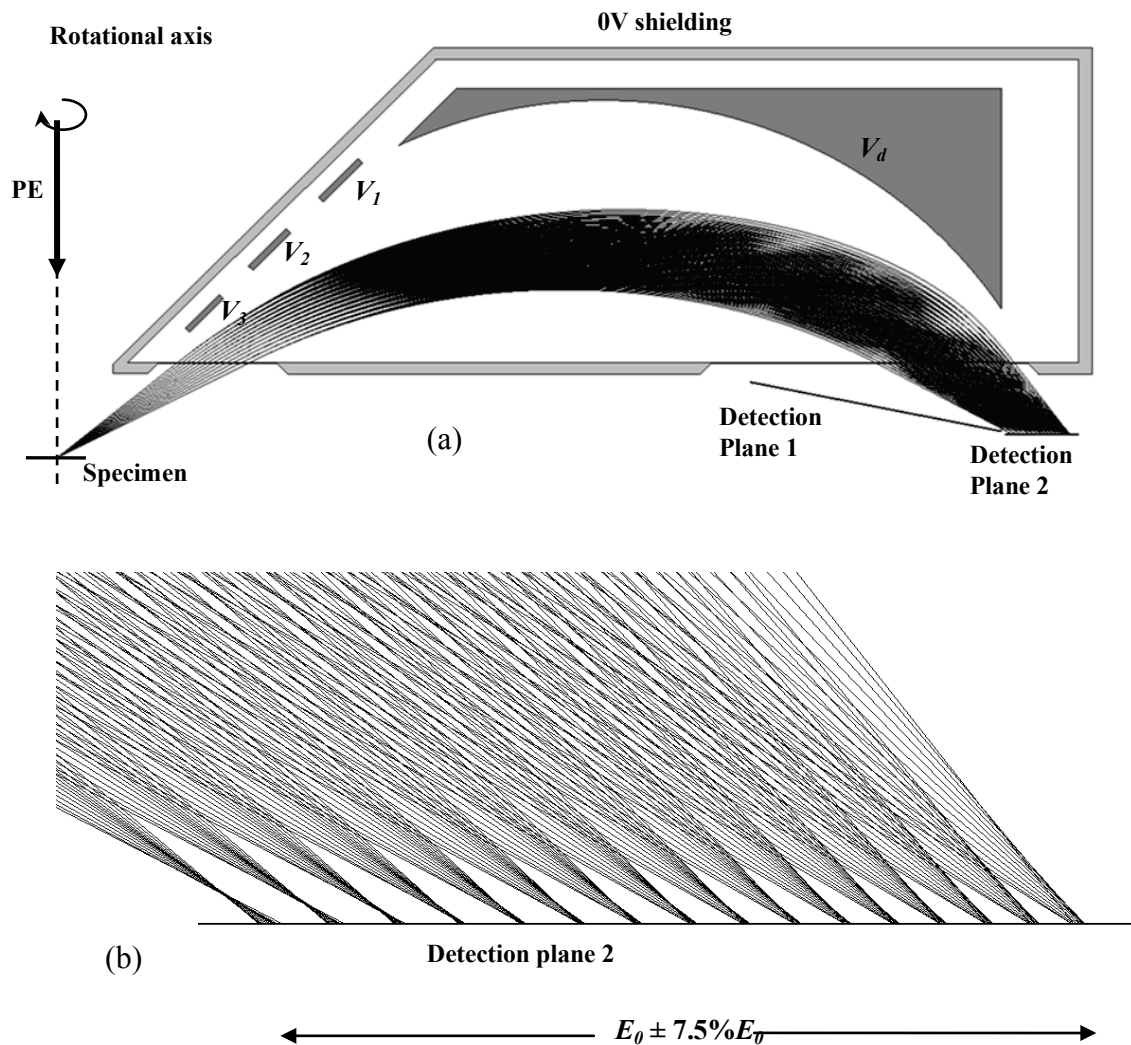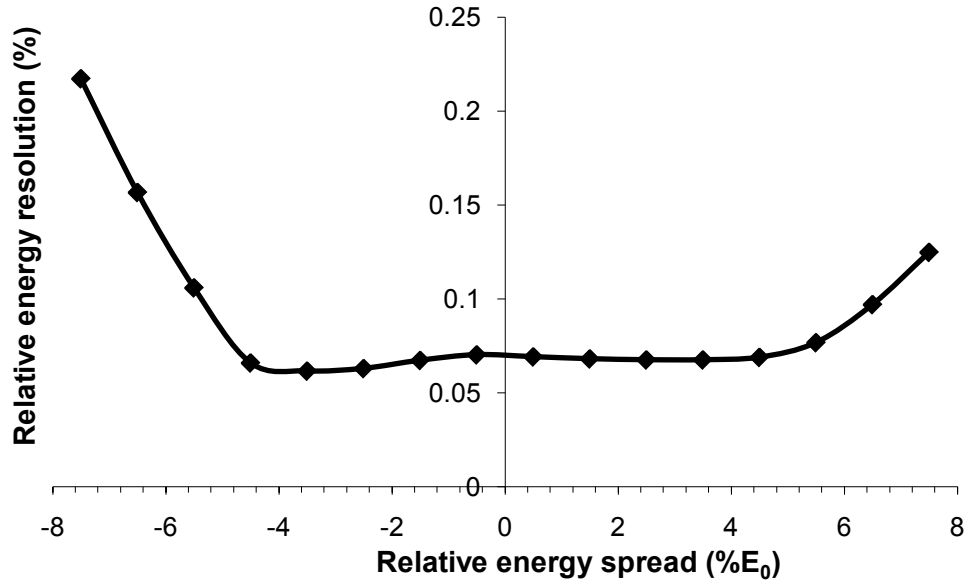
Fig. 4. 11. Simulated energy resolution across the energy band spanning 92.5% to 107.5% of the central energy along the horizontal detection flat-plane 2.

4.3   Conclusions

A high performance electron energy analyzer, called a RMA, suitable for use as an attachment inside the specimen chambers of conventional SEMs, has been reported. The analyzer is designed to fit around a conical shaped objective lens pole-piece/electrode, allowing for a relatively short minimum working distance, 5 mm or less. Simulation results for the analyzer design predict that it can combine high energy resolution with high transmission: a relative energy resolution of 0.025% for an entrance angular spread of ±6°, corresponding to a transmission of better than 15%. This energy resolution is around an order of magnitude better than the well-known Cylindrical Mirror Analyzer (CMA) for the same entrance angular spread.

The analyzer design allows for a parallel mode of operation in which the energy bandwidth on a conical-shaped detection plane is predicted to be as high as 30% (±15%) of the central-band energy. On a flat ring-shaped detection plane, the energy

bandwidth is predicted to be around 15% (±7.5%) of the central-band energy, over which the simulated relative energy resolution varies from 0.05% to 0.15% for angular spreads of ±6º.

The RMA can be used not only for electron spectroscopy inside the SEM but also for other electron spectroscopy applications such as Auger electron or photoelectron spectrometry, where high resolution and high transmission are required.

References

4.1 E. P. Benis, and T. J. M. Zouros,"The hemispherical deflector analyser revisited II. Electron-optical properties", J. Electron. Spectrosc. Relat. Phenom. 163 (2008) 28-39.

4.2 H. Z. Sar-El, "Criterion for comparing analyzers", Rev. Sci. Instrum, 41 (1970) 561.

4.3 K. Siegbahn, N. Kholine, and G. Golikov, "A high resolution and large transmission electron spectrometer", Nucl. Instrum. Meth. A 384 (1997) 563.

4.4 V. D. Belov, and M. I. Yavor, " New type of high-resolution high-transmission energy analyzers based on toroidal mirrors", J. Electron Spectr. Rel. Phenom. 104 (1999) 47.

4.5 V. D. Belov, and M. I. Yavor , "High-resolution energy analyzer with a large angular acceptance for photoelectron spectromicroscopy applications", Rev. Sci. Instrum. 71 (2000) 1651.

4.6 D. Cubric, A. De Fanis, N. Kholine and I. Konishi, "Design and applications of novel charged particle energy analysers", Proceeding of the 11th seminar on recent trends in charged particle optics and surface physics instrumentation, Rrno (2008) 17

4.7 D. Cubric, N. Kholine and I. Konishi, "Electron optics of spheroid charged particle energy analyzers", Nucle. Instru. Method. Phys. Res A. (2010) doi:10.1016/j.nima.2010.12.055.

4.8 Lorentz - 2EM, Integrated Engineering Software Inc, Canada.

4.9 W. Schmitz and W. Mehlhorn, "Parallel plate analyser with second order focusing property", J. Phys. E: Sci. Instrum., 5 (1972) 64.

Chapter 5: Conclusions

5.1 Conclusions

The main objectives of this thesis were to develop electron energy spectrometers for the Scanning Electron Microscope (SEM), in order to make it a more powerful instrument for nano-scale material and device inspection. Three electron energy spectrometers were designed, a circular magnetic beam separator spectrometer, a second-order focusing spectrometer, and a Radial Mirror Analyzer (RMA).

The first spectrometer is designed for high resolution SEMs, where the specimen is located in a strong electric retarding/magnetic field. A circular magnetic deflection field separates scattered electrons from the primary beam and directs them to three retarding field magnetic sector post-deflectors, after which their energies are detected in parallel. The effect of angular dispersion at the detector plane is significantly reduced by the use of a transfer lens, pre-focusing scattered electrons into the centre of the beam separator. It is predicted that the spectrometer can acquire the entire energy range of scattered electrons from the specimen in parallel with high transmittance (around 30% for the AE range, 50% for the BSE range, and up to 100% for the SE range), much better than most existing spectrometer designs, whose transmittance is usually much less than 20%. Its energy resolution is simulated to be comparable to that of the CMA for the AE range (0.2% - 0.8%) and to be acceptable for the SE range (less than 0.2eV) and BSE range (less than 1%). Initial experimental results confirmed that a circular beam separator can function as an energy spectrometer for scattered electrons in the SEM.

The second electron energy spectrometer is a fully 2π radian collection second-order focusing toroidal spectrometer for conventional objective lens SEMs. Simulations based upon direct ray tracing predict that the relative energy resolution of this spectrometer is around 0.146% for an angular spread of $\pm$ 6º, comparable to the theoretically best resolution of the CMA, and an order of magnitude better than existing first-order focusing toroidal spectrometers. Furthermore, its energy resolution is predicted to be greatly improved by use of a pre-collimating lens at its entrance, a simulated relative energy resolution of 0.021% was achieved for an angular spread of $\pm$6º. Also predicted for the spectrometer is a parallel energy acquisition mode of operation, where the energy bandwidth is expected to be greater than $\pm$10% of the pass energy. Experimental results from a prototype toroidal spectrometer attachment to the SEM confirmed its predicted energy resolution. Preliminary experimental results from the secondary electron and backscattered electron spectra, acquired by the prototype, indicate that the spectrometer has useful applications for quantitative voltage and material contrast.

The third electron energy spectrometer, named a Radial Mirror Analyzer (RMA), allows for relatively short working distances (5mm) under conventional objective lenses. Simulation results from direct ray tracing predict that the RMA has a much higher performance over previous spectrometer designs, a simulated relative energy resolution of 0.025% for an angular spread of $\pm$6º was achieved, an order of magnitude better than the CMA for the same entrance angular spread. The RMA design has parallel modes of operation. One parallel detection mode has an energy bandwidth as high as 30% ($\pm$15%) of the central-band energy on a conical-shaped detection plane. Another mode has an energy bandwidth of around 15% ($\pm$7.5%) of

the central-band energy on a flat ring-shaped detection plane, over which the simulated relative energy resolution keeps well within a range from 0.05% to 0.7% for an angular spread of ±6º.

5.2   Suggestions for future work

All the spectrometers designed in this thesis have the potential to become useful devices in scanning electron microscopy, the surface sciences and other areas in applied physics. Further development of the circular magnetic sector beam separator spectrometer requires enlarging the specimen chamber to reduce out-of-plane scattering, so that the sector diameter is significantly larger than the prototype attachment made in this work. A diameter of around 100mm is required.
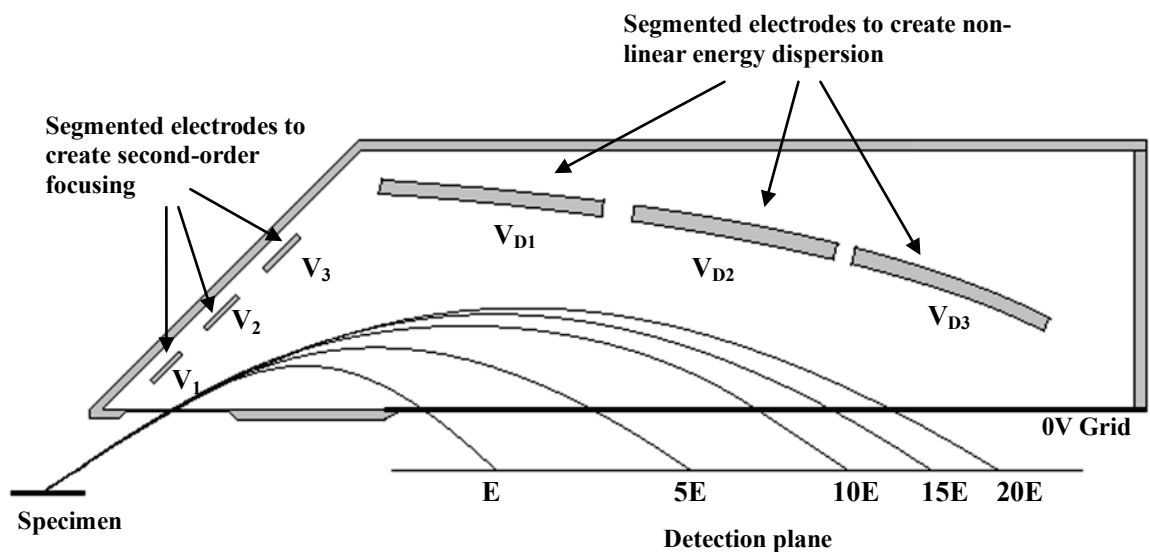

Fig. 5. 1. A schematic layout of a proposed parallel radial mirror analyzer (PRMA)

The RMA promises significant improvement in performance over previous Auger spectrometers, and the next step is to make an experimental prototype and test its energy resolution in practice. Further developments of the RMA design can be made

in order to make it a wider band energy analyzer while maintaining its second-order focusing properties. Simulation results showed that the non-uniform field distribution near the input of the spectrometer, created by a set of segmented electrodes, is the most critical parameter for second-order focusing. This can be combined with elongating/segmenting the main mirror electrode in the radial direction, producing non-linear energy dispersion on the detection plane, thereby extending its energy range, as shown in Figure 5.1. If this modification works, the design of a new second-order focusing parallel energy acquisition analyzer may be possible, perhaps called a Parallel Radial Mirror Analyzer (PRMA).

Appendix A: A semi-analytical technique for 3D field distribution simulation

The three-dimensional semi-analytical technique developed in this thesis, uses a two-dimensional finite element solution in combination with a Fourier Series expansion, to simulate 3D field distribution for both the magnetic and electric fields. Fig. A.1 shows schematic layouts of sector plates having odd and even symmetry planes. The scalar potential *Ψ(x,y,z)* represents magnetic fields in the case of odd symmetry and electric fields in the case of even symmetry. Consider a box with dimensions $(x,y,z)=(a,b,L)$. A finite element solution in the plane of the plates, $\Psi(x,y,L)=g(x,y)$, is used as the potential distribution on top of a box as indicated in Fig. A.1.
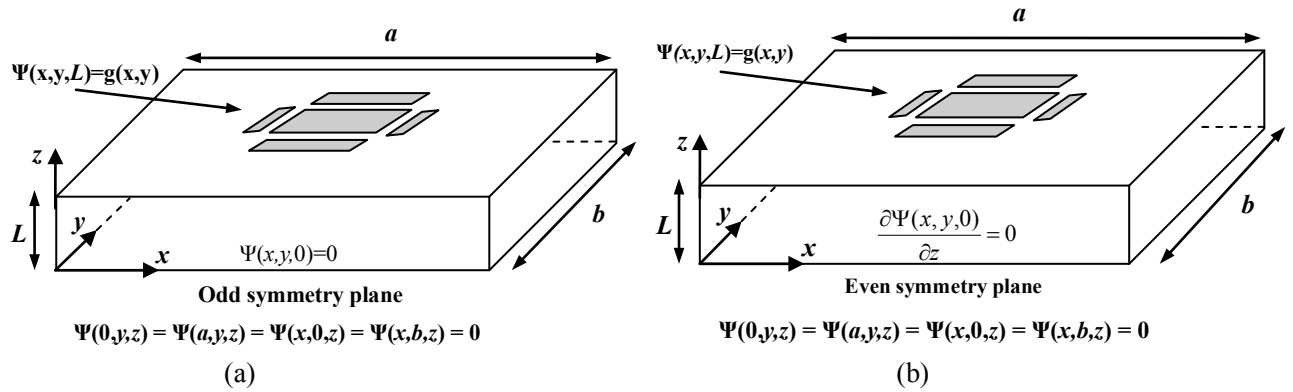
Fig. A. 1. Dimensions and boundary conditions for (a) the square magnetic sector deflector (b) the square electric retarding sector unit.

In the case of the square magnetic deflectors, where $z = 0$ represents the odd-symmetry plane and other sides have zero magnetic potential as shown in Fig. A.1a, the three-dimensional magnetic potential inside the box can be expressed as a double Fourier series as following

$$\Psi(x, y, z) = \sum_{m,n} C_{mn} \sin(k_m x) \sin(k_n y) \sinh(q_{mn} z) \qquad (A.1)$$

where $k_m = \dfrac{m\pi}{a}$, $k_n = \dfrac{n\pi}{b}$, $q_{mn} = \sqrt{k_m^2 + k_n^2}$, and

$$C_{mn} = \frac{4}{ab\sinh(q_{mn}L)}\int_0^a\int_0^b g(x,y)\sin(k_m x)\sin(k_n y)dxdy$$

For the square electric retarding units where $z = 0$ represents the even-symmetry plane and other sides have zero electrical potential as shown in Fig. A.1b, the three dimensional electric potential inside the box can be expressed as the following double Fourier series as following

$$\Psi(x,y,z) = \sum_{m,n} C_{mn}\sin(k_m x)\sin(k_n y)\cosh(q_{mn}z) \qquad (A.2)$$

where $k_m = \dfrac{m\pi}{a}$, $k_n = \dfrac{n\pi}{b}$, $q_{mn} = \sqrt{k_m^2 + k_n^2}$, and

$$C_{mn} = \frac{4}{ab\cosh(q_{mn}L)}\int_0^a\int_0^b g(x,y)\sin(k_m x)\sin(k_n y)dxdy$$

The magnetic and electric fields in the both cases can be simply obtained by differentiating the equations (A.1) and (A.2).

Appendix B: Publications resulting from this project

JOURNAL PUBLICATIONS

1. <u>H. Q. Hoang</u>, M. Osterberg and A. Khursheed, "*A toroidal electron energy spectrometer attachment for the SEM*", revised to Ultramicroscopy.

2. <u>H. Q. Hoang</u> and A. Khursheed, "*A Radial Mirror Analyzer for scanning electron/ion microscopes*", Nuclear Instrument and Methods in Physics Research A (2011), doi:10.1016/j.nima.2011.01.085

3. <u>H. Q. Hoang</u> and A. Khursheed, "*Improvement of a second-order focusing toroidal spectrometer by use of a pre-collimating lens*", Nuclear Instrument and Methods in Physics Research A (2010), doi:10.1016/j.nima.2010.12.009.

4. <u>H. Q. Hoang</u>, M. Osterberg and A. Khursheed, "*Experimental results from a second-order focusing electron toroidal spectrometer attachment for the scanning electron microscope*", Nuclear Instrument and Methods in Physics Research A (2010), doi:10.1016/j.nima.2010.12.010

5. A. Khursheed, K. H. Cheong and <u>H. Q. Hoang</u>, "*Design of a parallel mass spectrometer for focused ion beam columns*", Journal of Vacuum Science and Technology B. 28 (2010) C6F10.

6. <u>H. Q. Hoang</u> and A. Khursheed, "*A toroidal spectrometer for signal detection in scanning ion/electron microscopes*", Journal of Vacuum Science and Technology B. 27 (2009) 3226

7. T. Luo, A. Khursheed, M. Osterberg and <u>H. Q. Hoang</u>, "*The design of multiple electron beam imaging technique for surface inspection*", Journal of Vacuum Science and Technology B. 27 (2009) 3256

8. M. Osterberg, <u>H. Q. Hoang</u> and A. Khursheed, "*Initial Experimental Results on a Magnetic Beam Separator Spectrometer for the SEM*" Ultralmicroscopy 109 (2009) 1310

9. <u>H. Q. Hoang</u> and A. Khursheed, *"Energy dispersion characteristics of a magnetic beam separator"*, Physics Procedia 1 (2008) 161.

10. A. Khursheed and <u>H. Q. Hoang</u>, *"A second-order focusing electrostatic toroidal electron spectrometer with 2π radian collection"*, Ultramicroscopy 109 (2008) 104

11. A. Khursheed and <u>H. Q. Hoang</u>, *"Redesign of the scanning electron microscope for parallel energy spectral acquisition"*, Ultramicroscopy 108 (2008) 151.

<u>CONFERENCE PUBLICATIONS</u>

12. <u>H. Q. Hoang</u> and A. Khursheed, *"High resolution-transmittance energy analyzer designs for electron/ion microscopes"*, 8th international conference on charge particle optics, Singapore, July 12-16, 2010.

13. <u>H. Q. Hoang</u>, M. Osterberg and A. Khursheed, *"A Toroidal energy spectrometer attachment for scanning electron/ion microscopes"*, 8th international conference on charge particle optics, Singapore, July 12-16, 2010.

14. <u>H. Q. Hoang</u>, M. Osterberg and A. Khursheed *"A High energy resolution low noise electron spectrometer for IC failure analysis"*, the 54th international conference on electron, ion, and photon beam technology and fabrication (EIPBN), USA, June 1-4, 2010.

15. <u>H. Q. Hoang</u> and A. Khursheed, "*A toroidal spectrometer for signal detection in scanning ion/electron microscopes*", the 53rd international conference on

electron, ion, and photon beam technology and fabrication (EIPBN), USA, May 26-29, 2009.

16. H. Q Hoang, M. Osterberg, and A. Khursheed, "*Experimental results from a magnetic beam separator spectrometer in the SEM*", Proceeding of the 11th Seminar on Recent Trends in charged particle optics and Surface Physics Instrumentation, Brno Czech Republic, pp45, 2008

17. A. Khursheed, H. Q. Hoang, and S. K. Musuwathi, "*Variable magnetic sector field electron spectrometers for parallel energy acquisition*". Proceeding of the 11th Seminar on Recent Trends in charged particle optics and Surface Physics Instrumentation, Brno Czech Republic, pp59, 2008

18. H. Q. Hoang, and A. Khursheed, "*Redesign of the scanning electron microscope for parallel energy spectral acquisition*", 7th Conference for Charged Particle Optics, Cambridge UK, 2006.

19. H. Q. Hoang, J. Wu, M. Osterberg and A. Khursheed, "*Direct ray tracing of electrons through curved magnetic sector plates*", Proceedings of 10th Seminar on Recent Trends in charged particle optics and Surface Physics Instrumentation, Brno Czech Republic, p29, (2006).